Chirality Induced Spin Selectivity in Functionalized Carbon Nanotubes

by

Md Wazedur Rahman

A thesis submitted in partial fulfillment of the requirements for the degree of

Doctor of Philosophy

in

Solid State Electronics

Department of Electrical and Computer Engineering
University of Alberta

Abstract

In recent years it has been established that electrons become strongly spin polarized when transmitted through chiral compounds and their polarization is dependent on the chirality of the medium. This effect is known as chirality induced spin selectivity or CISS. CISS could be used to realize efficient spin injectors and detectors, which are expected to significantly improve the performance of spintronic devices. There are a number of organic molecules that can exhibit the CISS effect, including nucleic acids and peptides. The organic molecules found in nature are typically insulators that have extremely low electrical conductivities, making them unsuitable for use in practical electronic devices. In this study, we employ carbon nanotubes (CNTs) as transport channels to enhance conductivity, while chiral compounds are used as functionalization entities to induce spin polarization *via* CISS.

CNTs helically functionalized with single-stranded DNA (ssDNA), have recently emerged as a spin filter material. Inversion asymmetric helical potential of DNA creates a spin filtering effect, which polarizes carrier spins in the nanotube. Tube lengths in the submicron range can achieve ~70% spin polarization, although, according to theoretical predictions spin polarization is expected to increase with tube length. In an effort to study length-dependent CISS effect, we described a fabrication process that can yield DNA-wrapped nanotubes of length ∼1−4 μm. Results from this study indicate presence of highly spin-polarized carriers in these systems.

Tuning of DNA-CNT coupling is expected to affect the degree of carrier spin polarization in nanotubes. Also, in CISS, carrier spins are locked with their momentum directions, and in one-dimensional (1D) systems such as nanotubes, momentum flip must be accompanied by a simultaneous spin flip. This constraint can have a profound impact on charge transport in nanotubes. We have explored DNA-CNT spin filters in which CNTs have been functionalized with two different classes of sequences, exhibiting different degrees of coupling with CNT. They induce

different degrees of spin polarization in the channel, with significant impact on temperature-dependent charge transport and associated phenomena. Observed phenomena are consistent with spin-momentum locking expected in CISS systems. The observed negative background magnetoresistance, which results from interference effects between the forward and backward hopping routes, was examined further. CISS-induced spin polarization has been estimated to increase the carrier localization length by an order of magnitude in the low temperature range and it affects the magnetoresistance effect in a non-trivial way that is not observed in conventional systems.

Going beyond the helical geometry of DNA, by using the versatility of peptide chemistry, we demonstrate how spin polarization depends on molecular structural features such as chirality (in non-helical systems) as well as molecule-nanotube interactions. Our findings show that spin polarization can indeed be induced in two-dimensional (2D) carbon nanotube networks by “certain” molecules and the spin signal routinely survives length scales significantly exceeding 1μm. In addition to the more common chirality-dependent effect, a novel form of chirality-independent effect was discovered, and the total spin signal was found to be a mix of both. Finally, the magnetic field dependency of the spin signals was investigated, and the "chirality dependent" signal was shown to exist only at specific field angles.

The influence of *multiple* and mixed chiral functionalizations on 2D carbon nanotube networks is being investigated in the follow-up experiments. The initial results show that when two or more chiral systems are present, both chirality-dependent and chirality-independent processes contribute to the overall spin polarization. This finding suggests that the CISS effect can be fine-tuned further by manipulating the chiral centers in the medium.

Preface

This dissertation has been written in manuscript style with an Introduction (some of the fundamental topics related to this research) followed by four manuscripts (Chapters 2 to 5, published in peer-reviewed journal). The remaining two Chapters (6 and 7) are research in progress. Typically, each Chapter follows the manuscript sequences of an introduction (covering the background), results and discussions followed by conclusion. Since every journal has its own format and guidelines for the manuscripts, the general guidelines for the thesis formatting specified by the Faculty of Graduate Studies were adopted here to ensure the consistency of the thesis. The manuscripts in this thesis are listed as follows along with the contributions from each of the authors for the manuscripts:

1. Md. Wazedur Rahman; M.C. Torres; Seyedamin Firouzeh; J.M. Cuerva; Luis Á.C.; Sandipan Pramanik. Molecular Functionalization and Emergence of Long-range Spin-dependent Phenomena in Two-dimensional (2D) Carbon Nanotube Networks. ACS Nano 2021, 15, 12, 20056–20066. https://doi.org/10.1021/acsnano.1c07739

   Authors Contributions:

   Md. Wazedur Rahman: Conceptualization, methodology, contact (Ni-Au) and device fabrication, characterization, formal analysis, validation, investigation, resources, data curation, writing-original draft and editing, writing review and visualization

   M.C. Torres: Sample synthesis (materials), resources, and review

   Seyedamin Firouzeh: Contact (Ni-Au) fabrication and review

   M.C. Torres: Sample synthesis (materials), resources, and review

   Luis Á.C.: Conceptualization, sample synthesis (materials), resources, writing review and editing, project administration and funding acquisition.

Sandipan Pramanik: Conceptualization, validation, investigation, manuscript composition, writing review and editing, supervision, project administration and funding acquisition

2. Md. Wazedur Rahman; F. Seyedamin; Sandipan Pramanik. Carrier Localization and Magnetoresistance in DNA-functionalized Carbon Nanotubes. Nanotechnology 32 (2021) 455001. https://doi.org/10.1088/1361-6528/ac18d9

   Authors Contributions:

   Md. Wazedur Rahman: Conceptualization, methodology, contact (Ni-Au) and device fabrication, characterization, formal analysis, validation, investigation, resources, data curation, writing-original draft and editing, writing review and visualization

   Seyedamin Firouzeh: Contact (Ni-Au) fabrication and review

   Sandipan Pramanik: Conceptualization, validation, investigation, manuscript composition, writing review and editing, supervision, project administration and funding acquisition

3. Md. Wazedur Rahman; F. Seyedamin; M. Vladimiro; Sandipan Pramanik. Carrier Transport Engineering in Carbon Nanotubes by Chirality Induced Spin Polarization. ACS Nano 2020, 14, 3, 3389–3396. https://doi.org/10.1021/acsnano.9b09267

   Parts of Chapter 3 have been published in a conference [Md. Wazedur Rahman and Sandipan Pramanik, 'Spin filtering with $d(GT)_{200}$ wrapped single wall carbon nanotubes', The 80th Okazaki conference CISS-2019, Japan and Md. Wazedur Rahman and Sandipan Pramanik, 'Carrier transport mechanisms in DNA-functionalized carbon nanotubes and effects on magnetoresistance and spin filtering', The 80th Okazaki conference CISS-2019, Japan].

   Authors Contributions:

Md. Wazedur Rahman: Conceptualization, methodology, contact (Ni-Au) and device fabrication, characterization, formal analysis, validation, investigation, resources, data curation, writing-original draft and editing, writing review and visualization

Seyedamin Firouzeh: Contact (Ni-Au) fabrication and review

Vladimiro Mujica: Data analysis and discussion, writing review and editing

Sandipan Pramanik: Conceptualization, validation, investigation, manuscript composition, writing review and editing, supervision, project administration and funding acquisition

4. Md. Wazedur Rahman; Kazi M. Alam; Sandipan Pramanik. Long carbon nanotubes functionalized with DNA and implications for spintronics. ACS Omega, 2018, 3 (12), pp 17108–17115. https://doi.org/10.1021/acsomega.8b02237

   Parts of Chapter 2 have been presented (Oral and poster) in Faculty of Engineering Graduate Student Symposium (FEGRS), 2018, University of Alberta, Edmonton, Canada.

   Authors Contributions:

   Md. Wazedur Rahman: Conceptualization, methodology, contact (Ni-Au) and device fabrication, characterization, formal analysis, validation, investigation, resources, data curation, writing-original draft and editing, writing review and visualization

   Kazi M. Alam: Conceptualization, methodology, and review

   Sandipan Pramanik: Conceptualization, validation, investigation, manuscript composition, writing review and editing, supervision, project administration and funding acquisition

A comprehensive list of references including the references used at each of the manuscripts is provided at the end, followed by Appendices.

Acknowledgements

I'd like to convey my heartfelt gratitude to my thesis adviser, Prof. Dr. Sandipan Pramanik, who made the entire project feasible. His recommendations and support aided me throughout my research and thesis writing. My time working as a student of Prof. Sandipan Pramanik is a priceless asset that will help me for the rest of my life.

I'd also want to thank the members of my supervising committee, Dr. Manisha Gupta and Dr. Mani Vaidyanathan, for their advice and comments. I am grateful to the Electrical and Computer Engineering department at the University of Alberta for offering a wonderful working environment, as well as the NSERC (Natural Sciences and Engineering Research Council), Canada for their assistance.

It was a privilege to collaborate with my research group members, Dr. Srikrishna, Dr. Kazi Alam, Sayedamin, and others who provided assistance and helpful recommendations.

Finally, I'd want to express my gratitude to my parents (Md. Delwar Rahman and Mahfuza Bari) and family members, whose unwavering support and encouragement enabled me to accomplish this effort.

Table of Contents

List of Figures

List of Abbreviations

CISS	Chirality induced spin selectivity
CNTs	Carbon nanotubes
SWCNT	Single wall carbon nanotubes
MR	Magnetoresistance
GMR	Giant magnetoresistance
MTJs	Magnetic tunnel junctions
VRH	Variable-range hopping
WL	Weak localization
RBM	Radial breathing mode
TM	Tangential mode
FWHM	Full width half maximum
2D	Two dimensional
DNA	Deoxyribonucleic acid
SDS	Sodium dodecyl sulfate
Fmoc	N-Fluorenylmethoxycarbonyl
FF	Diphenylalanine
AA	Dialanine
GG	Diglycine
GdL	Glucono-δ-lactone
LZM	Lysozyme
CLLC	Cross-linked lysozyme crystals

Chapter 1. Introduction

1.1 Introduction

Spintronics is a field of research in electronics that aims to use the spin property of electrons to carry and process information.[1,2] The fundamental physical barriers (such as leakage current, heat, and power consumption) to continued shrinking of the micro- and nano-electronic devices have motivated exploration of new types of devices or physics. Spintronics is a promising technology in this regard, as it primarily relies on spin, the intrinsic angular momentum of an electron, instead of charge.[1,2]

In typical spintronic devices, ferromagnets are used as spin polarizer and analyzer and spin-orbit coupling is used to control spin superposition.[2] Recent studies showed that electron transport through chiral or helical molecules is spin selective.[3–5] Helical geometry of the molecules induces a strong inversion-asymmetric potential which generates spin-polarized current via spin-orbit interaction. This phenomenon is known as chirality induced spin selectivity (CISS)[4,6,7] and can be exploited to realize efficient spin polarizers and analyzers. The discovery of this phenomenon through transport experiments reveals an underlying magnetoresistance effect whose origin is still unknown. In recent studies, it has been suggested that the CISS effect may not be dependent only on helical geometry, molecular chirality alone may be sufficient to see this CISS effect.[8,9] In principle, achiral inversion-asymmetric systems could also exhibit spin-selective properties due to the intrinsic inversion-asymmetry of the molecules.[10]

Despite their unlimited chemical turnability, organic molecules behave as insulators, which limits the integration of the CISS effect with mainstream electronics or two-dimensional (2D) nanoelectronics.[11,12] CNTs (carbon nanotubes) functionalized with chiral molecules can potentially remedy this problem as they are more conductive than their organic molecules, and could provide a useful platform for practical spintronics devices.[13–15] However, nature of the CISS effect remains unclear in a two-dimensional (2D) nanotube network. Ability to introduce spin polarization in a 2D CNT network, will allow introduction of spintronic capabilities to a wide range of devices on this platform.

The goal of this research is to explore the CISS effect in functionalized CNTs using experimental techniques. Chapter 1 touches on some of the fundamental topics related to this research. Chapter 2 describes how helically functionalized CNTs are fabricated. Chapter 3 explores how the CISS effect in these system affects carrier transport. Chapter 4 describes the effect of DNA functionalization on conduction mechanism and explores possible origin of the observed background magnetoresistance. The results of Chapter 5 demonstrate that spin polarization can be induced in two-dimensional (2D) carbon nanotube networks by certain chiral, but non-helical molecules, and that the spin signal survives length scales that are considerably greater than 1 μm. In addition to the commonly known chirality-dependent effect, a novel form of chirality-independent effect was discovered, and the total spin signal was found to be a mix of both. Finally, the angle dependency of the spin signals was investigated, and the "chirality dependent" signal was shown to exist only at specific field angles. The influence of multiple chiral media on two-dimensional SWCNT networks is investigated in Chapter 6. Chapter 7 describes ongoing work on protein (lysozyme) functionalized CNTs.

1.2 Spintronics

Giant magnetoresistance (GMR) and tunneling magnetoresistance (TMR) are among the very first spintronic devices. The idea of spin-polarized current was first put forth in Ref.[16] with the discovery of giant magnetoresistance (GMR) in (001) Fe/ (001) Cr multilayers in 1988, which revolutionized the data storage industry in the following decades. In 2007, P. Grünberg and A. Fert received the Nobel prize in physics for the discovery of GMR.[17]

Giant magnetoresistance (GMR) is a quantum effect observed in magnetic multilayers, where the adjacent ferromagnetic thin films are separated by nonmagnetic thin films. The relative magnetic orientations in the ferromagnetic layers strongly influence the electrical resistance in the presence of an external magnetic field. In general, a parallel orientation between the ferromagnetic layers corresponds to lower electrical resistance, while an antiparallel orientation gives higher resistance.[18] Ferromagnetic transition metals have been extensively used over the next decade to study GMR and related devices. The GMR ratio can be defined as $\frac{\Delta R}{R} = \frac{R_{\uparrow\downarrow} - R_{\uparrow\uparrow}}{R_{\uparrow\uparrow}}$; where, $R_{\uparrow\uparrow}$ is the resistivity for parallel orientation and $R_{\uparrow\downarrow}$ is the resistivity for antiparallel orientation.[19] The discovery of GMR led to a family of spintronic devices that rely on spin-dependent charge

transport. These include TMR (or magnetic tunnel junction (MTJ)) devices, spin valves, *etc.* Most of the developments in spintronics so far are based on inorganic materials and semiconductors.[20,21] Recent research has shown that organic molecules can play an important role in spintronic devices, as they perform efficiently both as spin polarizer/analyzer and spin transport medium.[22,23]

1.2.1 Spin valve

The basic operating principle of a spin valve is similar to GMR because they both rely on spin-dependent transport. Non-magnetic (NM) materials carry electrons with an equal number of up and down spins (in equilibrium). On the other hand, ferromagnets (FM) carry electrons with a net spin component. In a spin valve device, a non-magnetic material is sandwiched between two ferromagnets, and the relative magnetization of the ferromagnets is controlled by an external magnetic field (Figure 1.1). Electrical resistance depends on the relative magnetization alignments of the ferromagnetic layers.[24,25] When electrons enter into a non-magnetic material from a ferromagnet, it carries a net spin component, which is parallel to the ferromagnet's magnetization. These electrons are transmitted easily by the other ferromagnet, if its magnetization aligns with the injected spins, resulting in low resistance. If the ferromagnetic layer has opposite magnetization, then the device will show higher resistance. An antiferromagnetic layer could be used to make one of the ferromagnetic layers magnetically fixed.[25,26]

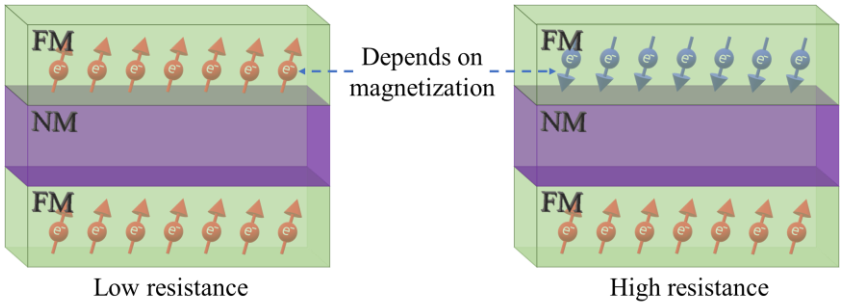

Figure 1. 1 *A schematic diagram of a spin valve.*

Over the past few decades, significant research has been carried out on spin valves dedicated to material, performance and architectural improvements.[27,28] Different inorganic and organic materials have been used as NM spacers and also as FM electrodes.[29] Nowadays, 2D materials are used as interfacial layer (typically wide-gap oxides such as Al_2O_3 or MgO) in spin-valve devices to increase the spin-dependent interface resistance between the NM and FM layers.[30,31]

1.2.2 Magnetic tunnel junction

Magnetic tunnel junctions (MTJs) are the primary building blocks in magnetic random-access memory (MRAM). The fundamental operating fashion of MTJs is based on spin-dependent tunneling (Figure 1.2). In MTJ devices two ferromagnetic layers (FMs) are separated by a thin (typically < 1 nm) insulator and tunneling current depends on the relative magnetization of the FM contacts (similar to the spin valves described above).[2] At first, Julliere reported this phenomenon in Co and Fe layers separated by a semiconductor (Ge) tunnel barrier (tunnel magnetoresistance or TMR).[32] This experiment was done at low temperatures ($T < 4.2\ K$) showing around 14% resistance change from parallel to anti-parallel. Later, much stronger TMR ratios were reported using Al_2O_3 or MgO tunnel barriers.[33,34]

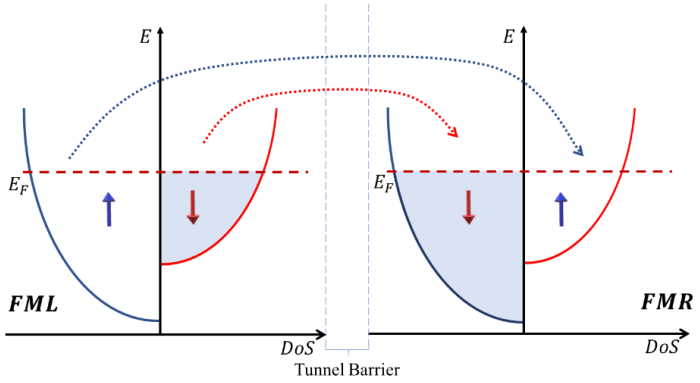

Figure 1. 2 *Schematic of density of states (DoS) of two oppositely magnetized ferromagnetic layers (arrows up/down indicate the spin direction) and spin-dependent tunneling.*

The tunnel conductance for parallel (P) and anti-parallel (AP) magnetizations are given by:

$$G_P \propto D_L{}^{\uparrow} D_R{}^{\uparrow} + D_L{}^{\downarrow} D_R{}^{\downarrow} \text{ and } G_{AP} \propto D_L{}^{\uparrow} D_R{}^{\downarrow} + D_L{}^{\downarrow} D_R{}^{\uparrow} \text{ respectively,}$$

where $D_L{}^{\uparrow}$ is the density of state (DoS) at the Fermi level for spin-up electrons and $D_R{}^{\downarrow}$ is the density of state (DoS) at the Fermi level for spin-down electrons. "L" and "R" represent left and right contacts, respectively.

The spin polarization of the FMs are defined as: $P_L = \frac{D_L{}^{\uparrow} - D_L{}^{\downarrow}}{D_L{}^{\uparrow} + D_L{}^{\downarrow}}$ and $P_R = \frac{D_R{}^{\uparrow} - D_R{}^{\downarrow}}{D_R{}^{\uparrow} + D_R{}^{\downarrow}}$

Based on the above equation one can derive the Julliere[32] formula:

$$TMR = \frac{G_{AP} - G_P}{G_{AP}} \; or \; \frac{G_{AP} - G_P}{G_P} = \frac{2\,P_L\,P_R}{1 + P_L\,P_R}$$

Clearly, high spin polarization materials are necessary to achieve high tunnel magnetoresistance (TMR). To enhance the performance of the device, researchers started to develop ferromagnetic alloys with high spin-polarization.[34,35] Also, various tunnel insulators (such as Al_2O_3, MgO, *etc.*) have been explored.[34,36] J. Moodera et al. reported room temperature TMR, with Al_2O_3 as a tunneling barrier.[33] Some research groups showed drastic improvement in the TMR ratio (over a few 100%) at room temperature by using an insulating MgO tunnel barrier.[36,37]

1.2.3 Organic spintronics

Organic electronics combined with spintronics opens a new hybrid field covering the areas of physics, chemistry, and material science.[38] In general, organic materials are considered as an insulators but in some cases, they can conduct electricity.[39] Over the last ten years, research in organic spintronics primarily focused on spin injection and transport through organics materials and the possibility of controlling spins in organic spintronic devices to enhance their efficiency.[38,40]

In the last few decades organic electronics has been explored with the promise of developing flexible, printable, wearable and cheaper electronics devices.[41–45] Electronic devices based on organic materials require a detailed understanding of carrier transport, the creation of exciton, transport, and recombination of the exciton for better performance. Organic ferroelectric materials led researchers to design flexible and printable electronic devices, especially for data storage applications.[46] The initial accomplishments of organic electronics especially in the field of optoelectronics (organic light-emitting diodes (OLEDs), organic field-effect transistors (OFETs), organic photovoltaic (OPV), *etc.*) created a strong interest for more fundamental research for other electronic devices based on organic materials. In principle, controlling spins in organic optoelectronic devices can enhance their efficiency. This motivated exploration in the area of "organic spintronics".

Inorganic materials, specially III-V semiconductors, have strong spin-orbit coupling (SOC), whereas organic materials (composed of mostly light elements such as C, H, N, O, *etc.*) show weak spin-orbit coupling. This leads to long spin relaxation time (weak spin-scattering mechanisms in organics).[47,48] Organic spin-valve devices are those in which an organic material has been used as the spacer layers between two ferromagnetic electrodes (spin injector/detector).[49,50] The organic layer is generally thick enough to avoid any magnetic coupling

between the ferromagnetic (FM) electrodes. One fundamental challenge for FM electrodes is to efficiently inject spin to the organic layer and again detect spin from the organic layer to FM.[51] Further research in this area is expected to give a satisfactory solution to this problem.

The essential operations in spintronics consist of injection, transport, manipulation, and detection of spin-polarized electrons. Along with spin injection, spin transport could be ballistic, diffusive, or via tunneling. Manipulation of spin mainly depends on spin-orbit interaction. In the context of organic spintronics, transport of spin-polarized carriers occurs by incoherent hopping conduction or by tunneling between localized states.[22,52] Organic materials (polymers and small molecules) are mostly π-conjugated hydrocarbons, where the p_z orbitals of the sp^2 hybridized carbon atoms overlap each other to form a delocalized electron cloud. The performance of the device depends on the carrier mobility within the π-conjugated hydrocarbons.[53] There is a lot of room for improvement for spin injection/detection as well as spin transport in organics, because inorganic devices continue to perform better than their organic counterparts.

1.3 Chirality induced spin selectivity (CISS)

Chirality induced spin selectivity (CISS) is an emerging research area in the field of spintronics. In chemistry, chirality is the geometrical property of a molecule in which the molecule's mirror image cannot be overlapped with it perfectly by any combination of translations and rotations.[54] Recent studies showed that electron transmission through chiral molecules depends on the electron's spin orientation.[55] The consequent spin polarization arising from spin selective electron transport can be very large compared to typical ferromagnetic spin filters. As discussed earlier, ferromagnetic contacts (such as Ni, Co, Fe, and their alloys) are generally used to generate and detect spin-polarized carriers and are often referred to as "spin filters".[56] CISS effect in electron transmission provides a new strategy for manipulating electron spins using organic materials and/or biomolecules.[4,5,57]

Extensive theoretical[58–60] and experimental[14,15,57,61] research is currently underway to understand the role of chirality in spin selective electron transport. Deoxyribonucleic acid (DNA) is a prototypical chiral molecule and has been used in early experiments on CISS.[5,14] The helical pattern of DNA creates helical potential, which polarizes the spins via the spin-orbit coupling. According to some studies the CISS effect may not require helical geometry,[8,9] but just the

existence of chirality may be sufficient. Spin polarization depends on molecular structural features such as chirality as well as molecule-nanotube interactions. In general, organic molecules and DNA are insulators, they carry very low currents, and they cannot be used to make practical devices. In this report, we use carbon nanotubes (CNTs) as a transport channel and induce chirality by functionalizing them with DNA (helical) and other chiral molecule (non-helical).

1.4 Carbon nanotubes

Depending on the hybridization of carbon atoms, carbon-based materials exist in three different allotropes. Graphene (building block of graphite) is one of the allotropes, in which sp^2 hybridized carbon atoms are arranged in a planner hexagonal lattice.[62] Carbon nanotubes (CNTs) are one-dimensional (1D) forms of graphene, formed by conceptually rolling up graphene sheet into a hollow cylinder. One-dimensionality of CNTs allows exploration of 1D phenomena in the quantum regime. Single-walled carbon nanotubes (SWCNTs) typically have diameter in the range of ~ 0.7 to 2.5 nm and length as large as micrometers, which results in extremely large aspect ratios (length/diameter) ideal for exploring 1D physics.[63] SWCNTs show remarkable electrical,[64,65] mechanical,[66] optical,[67,68] and thermal[69] properties as well as diameter- and chirality-dependent metallicity.[70] The chiral vector,[71] C_h is defined as –

$C_h = na_1 + ma_2$; where, n and m are integers ($0 \leq m \leq n$) and $\overrightarrow{a_1}$, $\overrightarrow{a_2}$ are graphene primitive vectors.

The chiral angle,[71] θ is expressed as –

$$\cos\theta = \frac{C_h \,.\, a_1}{|C_h||a_1|} = \frac{2n + m}{2\sqrt{n^2 + m^2 + nm}}$$

The nanotube diameter is given by,

$$d_t = \frac{|C_h|}{\pi} = \frac{a_{c-c}}{\pi}\sqrt{3(n^2 + m^2 + nm)}\,;\; a_{c-c} \approx 1.44\,A^o$$

CNTs are usually synthesized by high-temperature arc discharge (using electricity as an energy source), laser ablation (using high-intensity light), and low-temperature chemical vapor deposition (using heat from the furnace) method.[72] CNTs are always produced with several impurities such as amorphous carbon, nanocrystalline graphite, fullerenes, and various metals (such as Co, Ni, or Fe) depending on the methods used. So, one of the fundamental drawbacks of

these methods is purity which causes a major obstacle for practical applications. The precision of nanotube diameter, length, alignment, and purity makes low-temperature chemical vapor deposition (CVD) method (<800^o C) the most utilized method.[73] SWCNTs typically form bundles due to inter-tube van der Waals force,[74,75] making it difficult to utilize the properties of individual nanotubes as synthesized. Due to the same reason, it is difficult to disperse them to individual nanotubes using standard solutions. Different covalent and noncovalent surface functionalization approaches such as surfactants,[76] polymer wrapping,[77] DNA assisted separation[78,79] have been developed to address this problem.

1.5 Raman spectroscopy

Raman spectroscopy is a fast, powerful, and non-destructive method for the characterization of various carbon nanostructures. Several important information, such as diameter, chirality, conduction character, doping, *etc.* can be obtained from Raman characterization.[80] Due to the cylindrical symmetry of SWCNTs, their Raman spectra include two additional features (compared to graphene): a radial breathing mode (RBM) and a tangential mode (TM).[62] Raman spectrum of SWCNTs is typically taken at different (532 nm, 633 nm, and 785 nm) laser excitations.[80,81]

The RBM band appears in carbon nanotubes as carbon atoms coherently expand or contract in the radial direction (out-of-plane phonon mode) of the cylindrical geometry. The RBM is a low frequency ($\omega_{\mathrm{RBM}} \approx$ 100-500 cm^{-1}) band, and they give an easy and quick determination of the nanotube diameter.[71,80] The total mass of the carbon atoms along circumferential direction is proportional to the diameter, which gives the inverse proportionality between RBM frequency and diameter (d_t in nm):

$$\omega_{\mathrm{RBM}} = C/d_t \ (cm^{-1})\text{; where, C = 248 } cm^{-1}nm \text{ for isolated SWCNT}^{82}$$

The resonant Raman spectra of SWCNTs show similar D-band (1300-1350 cm^{-1}), G-band (1550-1600 cm^{-1}), and G'-band (2600-2700 cm^{-1}), as observed in graphene. D-band or defect peak appears both in CNTs and graphene due to the breakdown of the hexagonal structural symmetry. Both G-band, and G'-band are common in all sp^2-hybridized carbon. G-band is isotropic for graphene and anisotropic for SWCNTs. The tangential mode (TM) or the G-band for the SWCNTs exhibits two peaks (G^+ and G^-). The higher-frequency mode (G^+) is caused by in-plane

vibrations along the tube axis. The G^+-band appears at 1590 cm^{-1}, and can be fitted using a Lorentzian line shape. The lower-frequency mode (G^-) is caused by in-plane vibrations along the circumferential direction. The G^--band appears around 1570 cm^{-1}.[80,81] The G^+-band is diameter independent and G^--band is diameter dependent. Metallic SWCNTs exhibit an asymmetric Breit-Wigner-Fano (BWF)[83–85] lineshape in the G-band, indicating coupling of a discrete energy excitation level with a continuum spectrum. Asymmetric BWF lineshape is expressed by -

$I(\omega) = I_0 \frac{[1+(\omega-\omega_{BWF})/q\Gamma]^2}{1+[(\omega-\omega_{BWF})/\Gamma]^2}$;[83] where, I_0, Γ and $1/q$ are represents intensity, broadening factor and the asymmetry of the shape, respectively.

The BWF signal appears only when the electronic density of states at the Fermi energy $D(E_F)$ has a finite value. Semiconducting SWCNTs don't show any BWF in G^--band and can be fitted by a Lorentzian line shape.

1.6 Weak Localization

Weak localization is a type of quantum interference effect that occurs in impure conductive materials and causes negative MR. Conduction electrons diffuse through various impurities or defects with a finite mean free path.

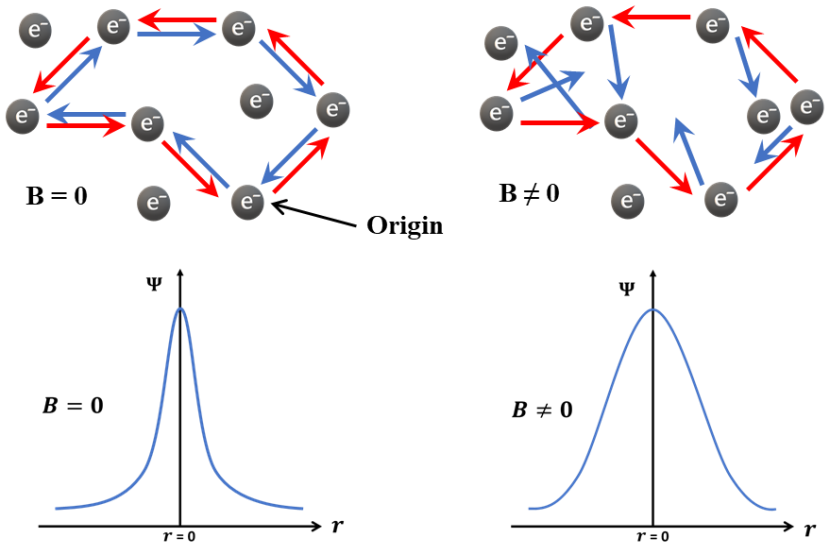

Figure 1. 3. *Conduction electron diffusion paths in both directions (red and blue lines). Weak localization occurs when a conduction electron completes a closed trajectory and arrives at the origin. An external magnetic field introduces a new phase between the two partial waves, which can reduce or eliminate constructive interference and makes the carriers less localized.*

The conduction electrons have a non zero probability of diffusing in a closed trajectory through multiple scattering centres and reaching the starting point or origin.[86,87] Due to the wave nature of electrons, there will be another diffusion path in the opposite direction (Figure 1.3). The phase and amplitude of these waves are the same when they return to the origin, resulting in constructive interference. This is referred to as "weak localization".[87–89] As a result of this constructive interference, electrons tend to stay localized at its origin, resulting in higher resistance. An external magnetic field introduces a new phase between the two partial waves, which reduces or eliminates constructive interference, and makes the carriers less localized. The loss of phase coherence between the partial waves is proportional to the strength of the magnetic field. The result of this effect is a gradual drop of material resistance with increasing magnetic field strength, resulting in a negative MR effect. At low temperatures, where the wave nature of electrons is preserved and phase breaking events due to phonons are uncommon, negative MR is commonly observed as a result of weak localization effects.

1.7 Chiral medium

CISS effect has been explored extensively in various chiral systems such as self-assembled DNA,[90] oligopeptides,[6] helicenes,[91] polymers,[92] metal-organic frameworks[93] and crystals,[94] supramolecular nanofibers[95] *etc.* In this work our goal is to explore this effect in CNTs functionalized with various chiral molecules. Details about these molecules are discussed below.

1.7.1 Single-stranded deoxyribonucleic acid (ssDNA)

All deoxyribonucleic acid (DNA) are made up of the same nitrogen-base molecules known as nucleotides.[96,97] There are four types of nucleotide: adenine ("A"), thymine ("T"), guanine ("G"), and cytosine ("C"). The sugar phosphate backbone, which is made up of 5-carbon deoxyribose sugars and phosphate groups, is a crucial structural component of DNA. This sugar phosphate backbone, twists around itself in a coil like screw threads, to protect the bases within it. This twisting defines the chirality of DNA structure, which is referred to as the "right-handed" and "left-handed" helix.[98]

In Chapters 2-4 we functionalized CNTs using ssDNA to investigate the CISS effect in this system. Theoretical studies have demonstrated that this system has the potential to function as a spin filter.[58,99] The DNA−CNT interaction is mediated by (a) π-stacking interaction between the

DNA bases and the p_z orbitals of the nanotube carbon atoms and (b) electrostatic interaction between nanotube and sugar-phosphate backbone.[79] The DNA strands, due to their intrinsic helicity, tend to wrap the nanotubes in a helical fashion.[100] The helical pattern of DNA creates helical potential, which polarizes the spins via the spin-orbit coupling.

It has been discovered that as number base-pair grow, so does spin polarization DNA molecules.[57] The carriers interact with the helical potential for a longer period of time during their transit through longer chiral systems. Longer nanotubes helically wrapped in DNA therefore can result in larger degree of spin polarization.

1.7.2 N-Fluorenylmethoxycarbonyl (Fmoc) and dipeptides

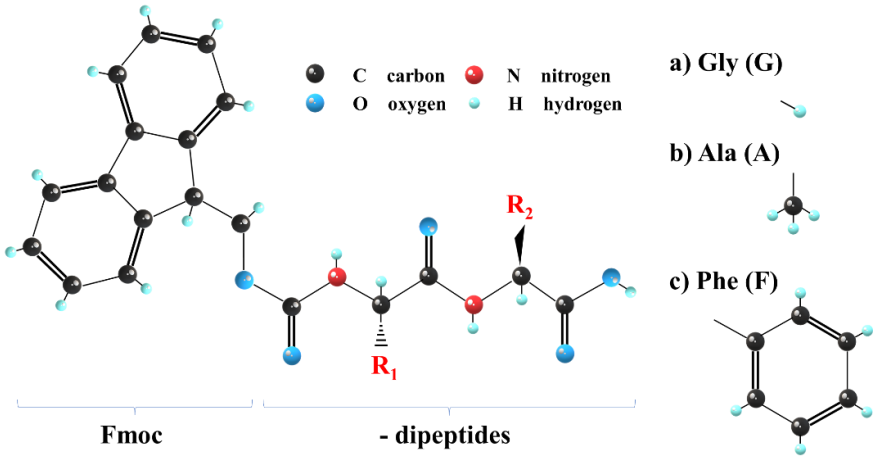

Figure 1. 4. *Molecular structure of Fmoc-dipeptides.*

The invention of the base N-fluorenylmethoxycarbonyl (Fmoc) group and its incorporation into peptide (a short chain of amino acids) synthesis techniques is regarded as a landmark in peptide chemistry.[101,102] In organic synthesis, Fmoc played an important part in the ability for self-assembly, which allows for quick and efficient peptide synthesis. On the other hand, chemical diversity in peptides is a key ingredient in designing novel biomimetic supramolecular structures. The poor electrical conductivity of these biomolecules limits them from being directly incorporated into practical electronic devices. Mixing Fmoc-amino acids with inorganic and organic nanoparticles has the potential to create intriguing hybrid materials in order to accomplish effective charge transport of these aromatic moieties.[103] These molecules can interact with carbon-based materials such as carbon nanotubes (CNTs) or graphene by non-covalent form of bindings.[104] The noncovalent forms of binding, such as π-π stacking,[105] hydrophobic

interactions,[106] and electrostatic adsorption,[107] are less influential on the structural and functional characteristics of CNTs and biomolecules than covalent functionalization.

Previously, Fmoc-ended aromatic amino acids were utilised to disperse CNTs.[108] Therefore, as functionalization entities we choose dipeptides linked to Fmoc- molecules. Fmoc- has a planar, aromatic achiral structure, which efficiently binds with CNTs[108–110] (as well as other Fmoc molecules[111–114]) in water, mainly via π-stacking interactions and form a three-dimensional network. Chirality can be introduced by appropriately choosing the side chains R1 and R2 (Figure 1a) in the amino acids that constitute the dipeptide. For example, Fmoc-diglycine (Fmoc-GG; R1 = R2 = H) is achiral whereas Fmoc-dialanine (Fmoc-AA; R1 = R2 = -CH3) or Fmoc-diphenylalanine (Fmoc-FF; R1 = R2 = -CH2Ph) are chiral and therefore the spin filtering effect can be studied in both enantiomers using L and D amino acids. In addition, among the various side chains, the ones with aromatic rings (such as FF) are expected to bind with CNTs more efficiently than the ones without (such as AA and GG). In this work (Chapter 5) amino acids having identical side chains and chirality were chosen (*i.e.*, R1 = R2, LL or DD) for ease of comparison between different data sets.

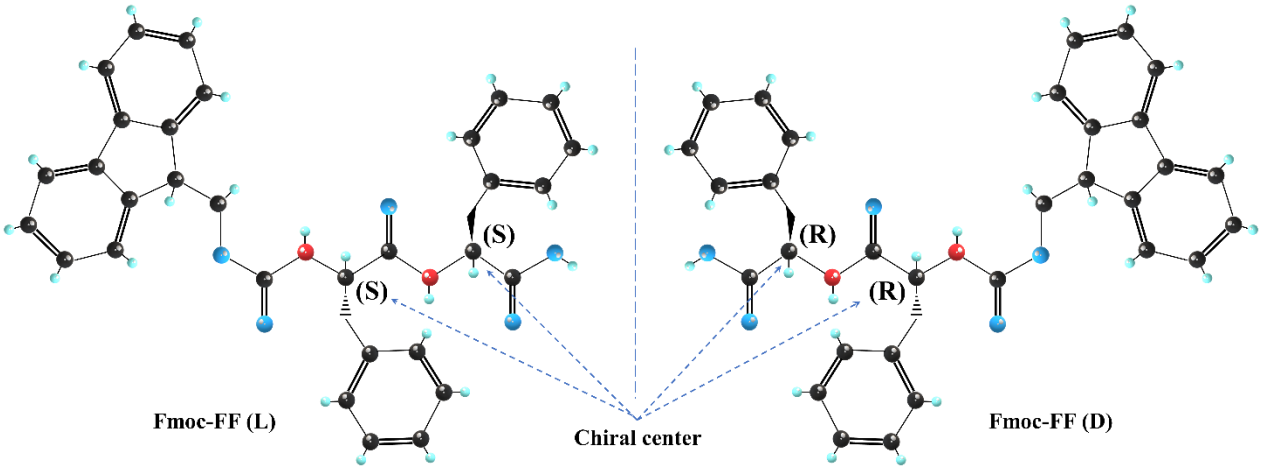

Figure 1. 5. *Two chiral centers with an absolute configuration of (S, S) for Fmoc-FF (L) and (R, R) for counterparts Fmoc-FF (D). Adapted from Ref.*[115]

Among all those dipeptides, one of the most studied peptides is Fmoc-Phe-Phe-OH (Fmoc-FF).[112] In stereochemistry, the R (Rectus, Latin for right) / S (Sinister, Latin for left) system is used to describe the configuration of a chirality center for enantiomers.[116] This approach names each chiral center R or S using a system in which its substituents are prioritized based on atomic number. In the case of Fmoc-FF (L) it has two chiral centers (Figure 1.5) with an absolute configuration of

(S, S), while its counterpart Fmoc-FF (D) has an absolute configuration of (R, R).[115] These two molecules are enantiomers, which means they are mirror images of each other. Thus, Fmoc-FF (L) is levorotatory, and Fmoc-FF (D) is dextrorotatory.

1.7.3 Glucono-δ-lactone (GdL)

Glucono-δ-lactone (GdL) plays a crucial role in carbohydrate metabolism and is found in many biological systems. Since GdL hydrolysis may release protons, it can be used as a moderate acidification reagent.[117,118] The use of GdL as a monomer in polymer synthesis produces a wide range of useful compounds.[119] A study by Garesio et al. demonstrates that gluconolactone can be used as a precursor for the synthesis of tensioactive agents.[120] Aside from their relevance in biological systems, lactones have numerous roles, including their easy water solubility, which has been proven to be excellent probes for the definition of lysozyme binding properties. GdL is hydrolyzed after two electrons and two protons are released during the electrooxidation of glucose.

There are six carbon (C) atoms (Figure 1.6) in the GdL ring, and every C atom is attached to a group of oxygen (OH).[121] Each carbon that bear both hydrogen and hydroxyl, will be a chiral center. GdL has four chiral centers - 3R,4S,5S,6R - where the number defines the position of the chiral carbon.[122]

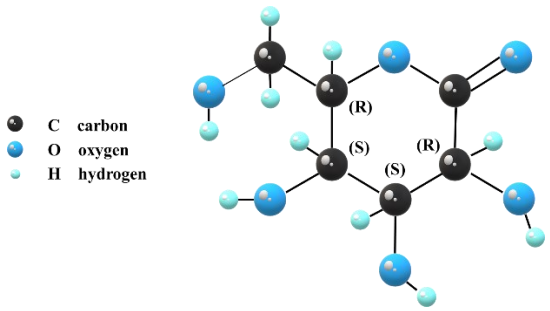

Figure 1. 6. *Molecular structure of glucono-δ-lactone (GdL).*

Recent research has emphasised the possibility of changing the structural and functional characteristics of the Fmoc-dipeptides based materials by the inclusion of one or more additional molecular entities.[114,123] The chirality of GdL will add additional chiral center along with the Fmoc-dipeptides in the system. The creation of this kind of supramolecular cross-linked network is referred to as hydrogelation.[124,125] A supramolecular structure is formed when molecules aggregate/interact via non-covalent interactions (like, ionic interactions, π -stacking, and hydrogen

bonds).[125] The formation of supramolecular hydrogels via assembly of Fmoc–dipeptides offer vast variety of applications.[126] The CISS effect is not well understood in the systems of multiple chiral molecules (GdL and Fmoc–dipeptides combined) due to a lack of fundamental knowledge. These constraints are the motivating factors for our experiment in Chapter 6.

1.7.4 Lysozyme (LZM)

Lysozyme (LZM) (1,4-β-N-acetylmuramidase) (molar mass ~14000 $gmol^{-1}$) is a highly stable cationic protein, containing a polypeptide chain of 129 amino acids with a diameter of around 3 nm.[127,128] The protein surface of LZM is folded into a tight globular shape with a lengthy cleft. The structure of LZM has been extensively studied and reveals how its various regions interact with one another dynamically.[129] The mixing of carbon nanotubes with proteins or particularly with LZM is fascinating in CNT dispersion, since it has the potential to enhance the properties of materials generated from CNT dispersions.[130] The understanding of proteins' interactions with CNTs is important for expanding the biological and medical applications of CNTs.[131,132]

The interaction between the LZM and sidewall of SWCNT is π-π stacking, which can form mechanically strong crystal on the macroscopic scale (~μm). One of the unique properties of LZM interaction with CNT is diameter dependency.[133] In our experiments reported in Chapter 7 we are using cross-linked lysozyme crystals (CLLCs)[134] embedded with semiconducting SWCNTs foe CISS experiments. Rafael et. al. proposed a method for the preparation of peptide hydrogel-based CLLCs with different concentrations of SWCNTs.[135] The final protein crystal (LZM+SWCNTs) shares many of the same intrinsic properties as SWCNTs (electrical conductivity, mechanical strength, *etc.*). The electrical conductivity and the mechanical strength (Young's modulus) increased along with the increasing concentrations of SWCNTs in LZM+SWCNTs composite crystal.[135] Given the chiral nature of the LZM crystal, this (Chapter 7) experiment aims to explore the presence of the CISS effect in these systems. Experiments in Chapter 7 has been done in collaboration with Universidad de Granada, 18071 Granada, Spain.

1.8 Summary and Conclusion

Functionalized CNT can potentially act as efficient spin filters as indicated by initial experimental and theoretical studies.[14,60,136] In this thesis we explore this area further, to better understand the CISS effect.

Chapter 2 of this thesis briefly reviews prior work on nanotubes functionalized by ssDNA, with a focus on final tube length. The fabrication process used by us, and the potential implications of this work have been described. Results from this work have been published in Ref.[137]

Chapter 3 of this thesis presents our results on ssDNA−CNT spin filters in which CNTs have been functionalized with two different classes of sequences, exhibiting different degrees of interaction with the CNT. CISS-induced spin-momentum locking phenomenon and its impact on charge transport in nanotubes have been explored. Results from this work have been published in Ref.[138]

Chapter 4 describes the effect of DNA functionalization on conduction mechanism and explores possible origin of the observed background magnetoresistance. Results from this work have been published in Ref.[139]

In Chapter 5, we demonstrate that "certain" molecules are able to induce spin polarization in two-dimensional (2D) carbon nanotube networks and that the spin signal survives length scales that are considerably longer than 1 μm. A chirality-independent effect, as well as the more frequent chirality-dependent effect, were identified, and the total spin signal is a combination of the two. Finally, angle dependence of the spin signals was investigated, and it was shown that the "chirality dependent" signal only occurs at specific field angles. Results from this work have been published in Ref.[140]

Chapter 6 investigates the effect of multiple chiral molecules on the CISS effect in two-dimensional SWCNT networks. Such studies have not been conducted before, to the best of our knowledge.

In Chapter 7 we discuss our ongoing research on CISS effect in Lysozyme functionalized SWCNT network. We outline possible future directions, which we are planning to explore in the near future.

Chapter 2. Synthesis and characterization of long (>1 μm) CNTs functionalized with DNA[†]

2.1 Introduction

As mentioned in the previous chapter, helical molecules such as DNA act as an efficient source and detector of spin-polarized charge carriers.[5,141] This phenomenon, often dubbed as chirality-induced spin selectivity or CISS, could be used to significantly improve the performance of spintronic devices, which utilize carrier spins (rather than charge) to realize electronic and sensing functions. Recently, it has been reported that carbon nanotubes, helically wrapped with DNA, can also act as an efficient source and detector of spin-polarized carriers, by virtue of spin−orbit coupling originating from the helical potential.[14,15] It has been found experimentally as well as theoretically that the CISS effect becomes more pronounced with the extension of the helical potential.[57,60] It has been found that spin polarization increases with increasing base-pair length[57], presumably because the carriers experience prolonged interaction with the helical potential during their transit through longer chiral systems. By the same token, longer nanotubes, helically wrapped with DNA, is expected to produce a higher degree of spin polarization. Recent experiments performed on ~750 nm long tubes resulted in ~70-80% spin polarization[14,15]. Since the overall efficiency of spintronic devices depends critically on spin filtering efficiency[142], ideally ~100% spin polarization is desirable, which could be obtained from longer nanotubes with helical functionalizations. However, most earlier studies on CNT-DNA functionalizations (reviewed below) resulted in short tubes (typically less than 1 μm) due to fabrication constraints. Motivated by this, here, we report fabrication of isolated and long (~1-4 μm) nanotubes, helically wrapped with DNA strands. The fabrication process is applicable for both metallic and semiconducting nanotubes. Functionalized nanotubes have been characterized in detail by AFM, optical absorption experiments, Raman spectroscopy and temperature-dependent electrical transport. Initial transport measurements indicate the presence of strong magnetoresistance in these tubes, which could be attributed to spin-dependent effects. Systematic fabrication of long DNA-wrapped nanotubes is

[†] Parts of this chapter have been published in - Rahman, M. W., Alam, K. M. and Pramanik, S. Long Carbon Nanotubes Functionalized with DNA and Implications for Spintronics. ACS Omega 2018, 3, 12, 17108–17115.

expected to enable further investigation into the spin-dependent properties of these ultimate one-dimensional nanoscale hybrids and may have a significant impact on nanoscale spintronics.

2.2 Background

One of the major disadvantages of CNTs, however, has been their poor solubility in common aqueous and organic solvents. As-grown nanotubes (High-pressure carbon monoxide (HiPco)[143]-synthesized SWCNTs, Nano-Integris Inc.) often take bundled form because of intertube van der Waal's interaction, and for device applications, it is important to have them dispersed. To address this, various types of chemical functionalization techniques have been developed[70,144]. Functionalization can be performed primarily in two different ways, such as (a) covalent functionalization,[70] which while being chemically stable, adversely affects the intrinsic properties (such as electrical conductivity, toughness, *etc.*) of the nanotubes by inflicting irreversible structural damage and (b) noncovalent functionalization,[144] which keeps the inherent properties of the nanotubes intact but are comparatively less stable. Chemical functionalizations not only disperse the nanotubes, but they often allow separation of tubes based on their electronic properties (semiconducting vs. metallic)[70,144] and form the basis of a wide variety of electrochemical sensors,[145] by virtue of the attached chemical moieties.

For the purpose of device electronics, noncovalent functionalization is more desirable because it minimally affects the intrinsic electronic properties of the tubes. One simple and efficient approach is functionalization using single-stranded DNA, which has been investigated extensively in the past.[78,79,146] The DNA−CNT binding energy is higher than the CNT−CNT binding energy, which facilitates tube separation.[79] The DNA−CNT interaction is mediated by (a) π-stacking interaction between the DNA bases and the p_z orbitals of the nanotube carbon atoms and (b) electrostatic interaction between nanotube and sugar-phosphate backbone.[79] The DNA strands, due to their intrinsic helicity, tend to wrap the nanotubes in a helical fashion.[100] Such helically wrapped nanotubes have been used for diverse applications in recent years.[147]

2.3 Prior work

Nanotube dispersion can be achieved via functionalizing CNTs with a wide range of polymers[70,144,148]. Here, however, we will focus on single-stranded DNA, because in most cases they wrap the tubes helically[78,79,149,150] and the composite hybrid is a promising spin filter

system[14,15]. Typically, nanotube powder is mixed with excess DNA solution. Next, ultrasonication is used to disintegrate the nanotube bundle, which allows the DNA strands to wrap with the tubes. This step also determines the length of the dispersed (and helically wrapped) nanotubes[151], which is a critical aspect for spin filter applications as described above. Finally, the mixture is centrifuged, which results in precipitation of unfunctionalized tubes and other impurities. Helically wrapped nanotubes are dispersed in the supernatant solution, which is decanted for further processing.

Zheng[79] et al. reported CNT wrapping by various lengths (60-, 30-, 21- and 15-mer) of poly-T strands, among which $d(T)_{30}$ produced the highest yield. Typical nanotube length, based on AFM, is ~ 50-1000 nm. In another experiment Zheng[78] et al. used $d(GT)_n$ (n = 10-45) to isolate SWCNTs, and length distribution of ~ 50 to 500 nm was observed. In particular, $d(GT)_{30}$ resulted in an average tube length of ~ 500 nm.[152] Gigliotti[153] et al. used long genomic ssDNA (~ 3796 bases) with random sequences to disperse CNTs. The average length was found to be ~ 700 nm and in a few instances, 2 μm long nanotubes were observed. Longer tube length was attributed to longer DNA strands and short sonication time (~ 10-20 minutes). However, due to the short sonication period, few nanotube bundles remained in the solution (not well dispersed), which is consistent with other studies.[151] Natural DNA has been used by several other groups as well.[154–156] Cathcart[156] et al. used ~10,000 base pair long DNA, which is expected to shorten after sonication. The reported average final nanotube length was ~260 nm. Vogel[157,158] et al. studied the effect of DNA sequence length on helical wrapping and separation of nanotubes. Short DNA strands, such as $d(GT)_3$ and $d(AC)_3$, were found to disperse CNTs more efficiently than the longer ones ($d(GT)_n$ and $d(AC)_n$, n = 4, 10, 20, 40). Yang[159] et al. were able to disperse nanotubes by double-stranded DNA (dsDNA). Typical DNA length was ~ 100-300 base pairs and from the AFM data, average nanotube length was around a few hundred nm. Yang[160] et al. reported loosening of DNA wrapping as strand length is increased.

2.4 Fabrication

The key aspects that determine the length of the final wrapped nanotubes are (i) length of the DNA strand because it is expected that long base-pair DNA will wrap longer tube segments and lead to longer wrapped nanotubes and (ii) ultrasonication parameters such as power and duration.[78] In this work, we focus on $d(GT)_n$ strands since they are known to produce efficient functionalization as well as exhibit spin filtering. We report data on $d(GT)_{200}$, which systematically

produces nanotubes with length ~1-4 μm, significantly longer than those reported in the current literature (< 1 μm). We varied the ultrasonication duration to maximize the length of the wrapped tubes. We compared our results with shorter $d(GT)_{15}$ strands and found that longer strands consistently produce efficient dispersion, without sacrificing the length of the tube.

For fabrication of DNA wrapped long nanotubes, we use $d(GT)_{200}$ strands (Integrated DNA Technologies). First, 20 nmole of DNA oligo is mixed with nuclease-free water and buffer to produce a 1 mg/ml ssDNA solution. Next, 0.7 mg HiPco SWCNTs (diameter ranging from 0.7 to 1.2 nm, Nano-Integris Inc.) is mixed with this solution, and the mixture was ultrasonicated (Sonics, VC130 PB) for 90 min at a power level of 7 W in an ice-water bath. After sonication, the mixture is centrifuged at 14000g for 90 mins, which precipitates undispersed SWCNTs at the bottom. The top part of the mixture was collected for further experiments.

A small part of the decanted supernatant solution is drop cast on top of SiO_2 substrate for a few mins, followed by thorough rinsing with DI water and drying under ambient conditions. These specimens are used for AFM (atomic force microscopy - Dimension Edge) studies. AFM observations described below, suggest that most of the bundled CNTs are converted into individually wrapped tubes. The minimum length of ssDNA-CNTs at this stage is 1 μm, and some are as long as 4 μm. For electrical transport measurements, a small amount of ssDNA-CNT supernatant solution was drop cast on pre-patterned Au and Ni contacts for 15 min. Next, the substrates are thoroughly rinsed with DI water and vacuum annealed (200^o C for 30 mins). Vacuum annealing improves the electrical contacts between the electrodes and ssDNA-CNTs and improves the reproducibility of charge transport measurements. Contact thickness is ~100 nm, and they were photolithographically patterned on top of SiO_2 (500nm)/Si wafer.

2.5 Result and discussion

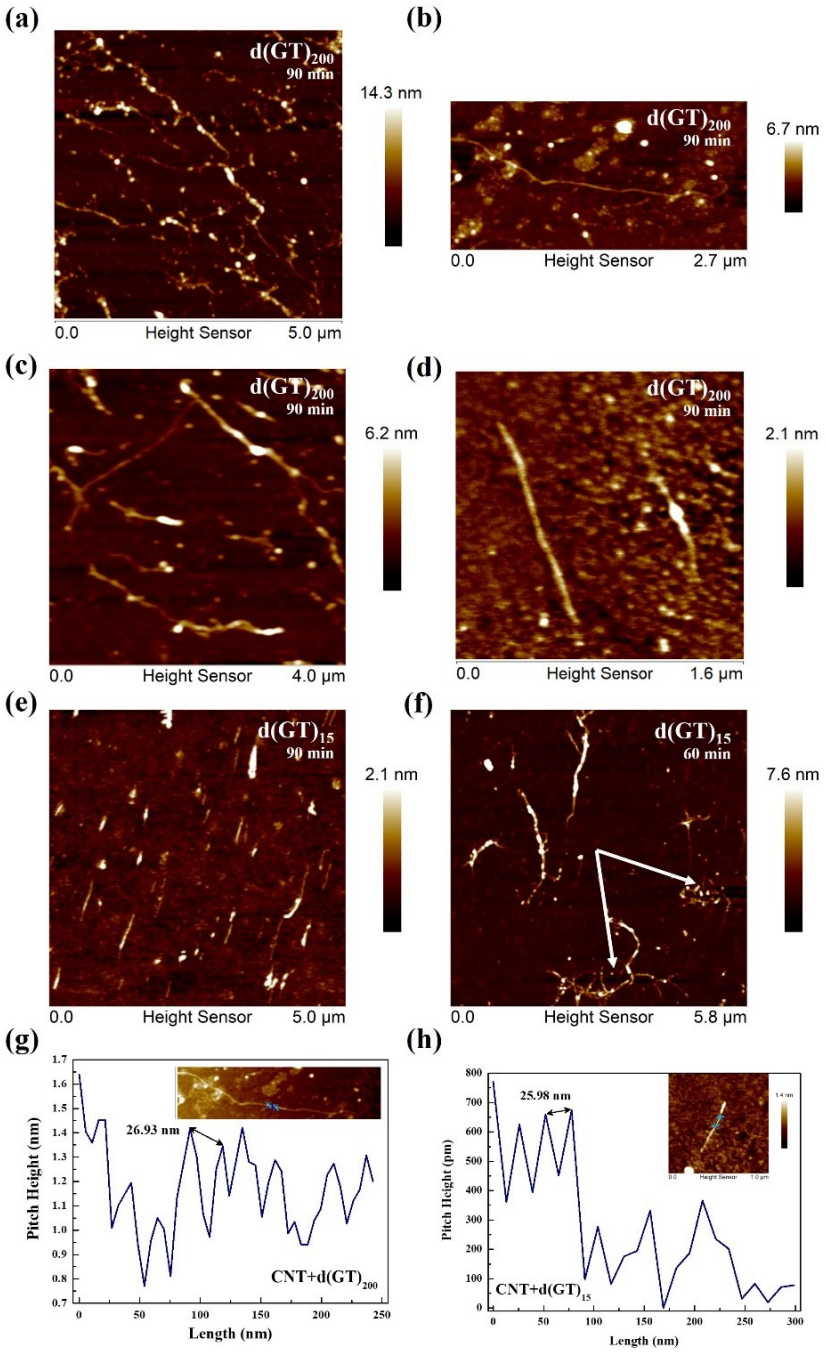

Figure 2. 1: *(a−f) AFM images of dispersed nanotubes wrapped with $d(GT)_{200}$ and $d(GT)_{15}$. Ultrasonication times are indicated in each image. (g, h) Both strands result in similar wrapping pitch.*[137]

Figure 2.1(a) shows $d(GT)_{200}$ wrapped nanotubes dispersed on a SiO_2 substrate. Figures 2.1(b), (c), (d) show representative images of tubes with length ~ 1-4 µm. For the purpose of comparison, Figure 2.1(e) shows wrapping using $d(GT)_{15}$ under the same fabrication condition as

above. In this case, however, tubes are <1 μm, which is consistent with previously published data cited above. Clearly, the length of the strands plays a role in determining the final length of the wrapped tubes. To check if reducing the sonication time using $d(GT)_{15}$ strands helps in preserving tube length, we carried out the process for 60 min. As seen from Figure 2.1(f), tube lengths are slightly longer (~ 2 μm), but the tubes are not well-dispersed and stay in the bundled form (indicated by arrows). Figure AP 1(a) (Appendix) shows nanotube length distribution collected from ~ 50 nanotubes. A clear difference in the average tube length is observed, with $d(GT)_{200}$ resulting in more than double the average length of $d(GT)_{15}$ functionalized tubes for identical sonication time (90 mins). Figures 2.1(g) and (h) show AFM height scan along the tube length for $d(GT)_{200}$ and $d(GT)_{15,}$ respectively. Periodic height modulation is observed, which indicates the presence of helical wrapping along the tube length. Wrapping pitch is ~26 nm in both cases, which is not surprising since both strands have identical chemical composition. The exact value of the wrapping pitch could be smaller than the above value due to convolution with the AFM tip.

For optical absorption measurements, a drop of ssDNA-CNT (or, SDS-CNT) supernatant solution was cast on a quartz substrate and naturally dried. We used Perkin Elmer Lambda 1050 UV-Vis-NIR spectrophotometer over a range of 400 to 1400 nm with a spectral resolution of 1 nm. SDS (Sodium Dodecyl Sulfate) functionalization was used for comparison, because unlike DNA, SDS does not wrap the tubes helically. For SDS functionalization, 1ml SDS (1% w/v) was mixed with 0.8 mg SWCNTs, followed by 90 min ultrasonication and 60 min centrifugation. Figure 2.2 shows the typical absorption spectra. Semiconducting HiPco tubes exhibit S_{11} (900-1600 nm) and S_{22} (550-900 nm) interband transitions and metallic HiPco tubes show M_{11} interband transition (400-650 nm)[78] in the measurement range. Observation of multiple peaks in the spectrum indicates the presence of nanotubes with different chiralities in the sample. As shown in the *inset* of Figure 2.2, the peaks are narrower for $d(GT)_{15}$ and $d(GT)_{200}$, compared to SDS, indicating more efficient dispersion by the DNA strands. Compared to SDS functionalized tubes, DNA functionalization causes a blue shift (~25 nm, Figure 2.2 *inset*) in the absorption peaks. Statistical data showing multiple (~3) scans, their average and standard deviation are presented in Figure AP 1(b) (Appendix), which confirms the above features. Further information about the dispersed nanotubes can be extracted from Raman spectroscopy as described below.

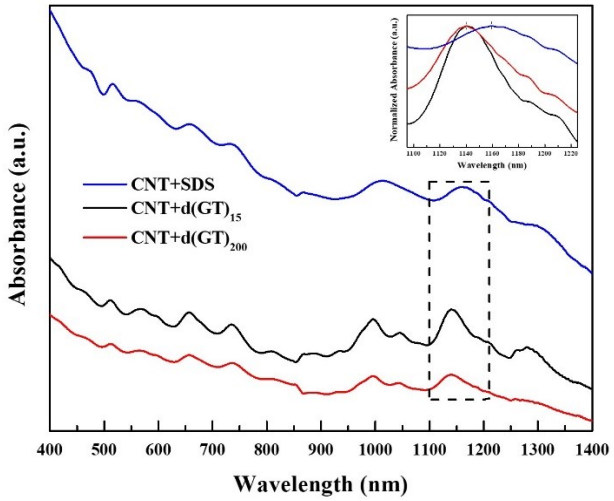

Figure 2. 2: *Ultraviolet−visible−near infrared (UV−Vis−near IR) absorption spectra of nanotubes dispersed by various reagents. Multiple peaks indicate the presence of nanotubes with different chiralities in the specimen. As shown in the inset, DNA wrapping causes narrowing and blue shift of an absorption peak compared to SDS-wrapped tubes.*[137]

Figure 2.3 shows representative Raman spectra (532 nm excitation, room temperature) before and after nanotube wrapping (dry condition, no annealing). Figure 2.3 (a) shows the RBM band, which occurs at lower wavenumbers and corresponds to the coherent radial vibrations of the carbon atoms[80]. The multiple peaks from the RBM spectrum of the bundled tubes in the 200-320 cm^{-1} range implies a diameter distribution of d_t = 0.8 - 1.2 nm (± 0.1nm) in the bundle. The main peak occurs around ~267 cm^{-1}, which corresponds to a diameter of ~ 0.9 nm, matching closely with vendor specification. This main peak is also quite broad, with FWHM of ~ 19.33 cm^{-1}. After DNA wrapping, RBM peaks tend to get narrower, as a result of dispersion and nanotube isolation (Figure 2.3 (a)). For example, d(GT)$_{15}$ and d(GT)$_{200}$ lead to FWHM (main peak) of ~ 11.94 cm^{-1} and 12.15 cm^{-1} respectively. DNA wrapping also leads to fewer peaks compared to the bundle, due to fewer population of nanotubes in the sample and diameter selectivity of the wrapping process. Interestingly, the peak positions are shifted slightly (~ 4 cm^{-1}) towards higher wavenumbers. DNA wrapping tends to constrain the radial vibration of the carbon atoms, leading to an effective increase in the tube stiffness in the radial direction, resulting in higher wavenumbers. This feature confirms the tight physical wrapping of nanotubes by the DNA strands.

Comparing all the three reagents used for dispersion, it appears that d(GT)$_{15}$ and d(GT)$_{200}$ are approximately equally effective in terms of wrapping compactness. On the other hand,

dispersion using SDS does not appear to be as effective as the DNA strands, since the RBM band closely resembles the bundled CNT.

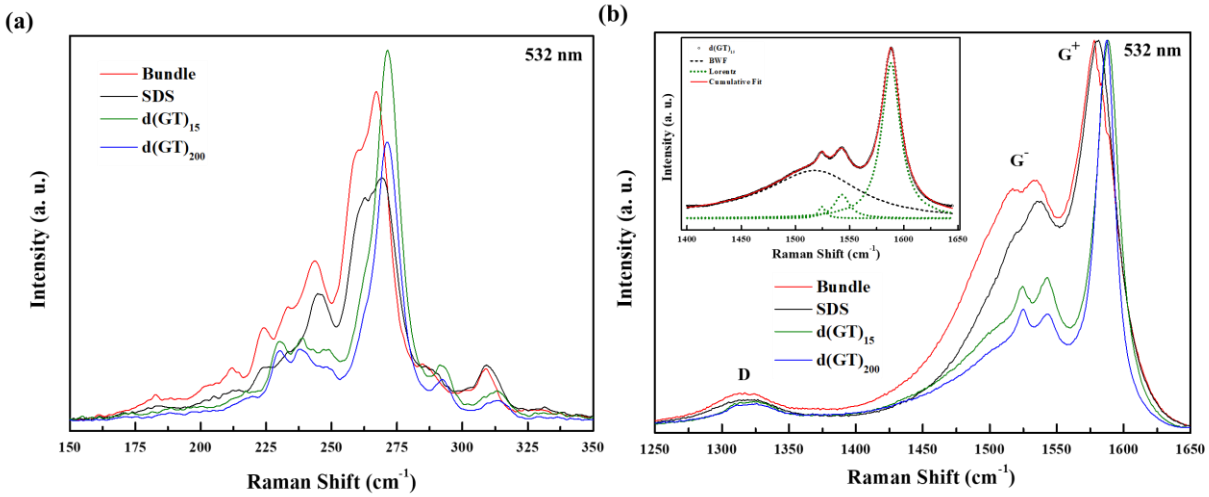

Figure 2. 3: *Raman characterization of bundled nanotubes and dispersed nanotubes using 532 nm excitation. Three different dispersing reagents have been used: SDS, d(GT)15, and d(GT)200. (a) RBM and (b) TM or G-band. A weak defect (D) band is present at ~1350 cm^{-1}. (b) Inset shows fitting of the G band with three Lorentzians and one B−W−F lineshape.*[137]

Figure 2.3(b) shows the TM mode (or G-band) for the nanotube bundle and after functionalization with three different reagents. The TM mode has two prominent peaks: G^+, which occurs around 1580 cm^{-1} and G^-, which occurs at lower wavenumbers (~1525 cm^{-1}). The G^+ peak originates from the longitudinal vibrations of carbon atoms along the tube axis, whereas G^- is due to the circumferential vibrations[161]. The force constant of C-C bonds is larger along the longitudinal direction compared to the tangential direction, which explains the difference between the frequencies of these two bands. After DNA functionalization, circumferential vibration gets quenched due to tight wrapping with DNA strands, which results in weaker G^- peaks, as can be seen clearly from Figure 2.3(b). Overall, as expected, the G-band gets narrower after dispersion, compared to the bundle. For example, the G^+ peak has an FWHM of 41.83 cm^{-1} for bundled tubes, which reduces to 17.9 cm^{-1} for d(GT)200 wrapping and 22.12 cm^{-1} for d(GT)15 wrapping. Wrapping with SDS reduced the FWHM to 35.34 cm^{-1}, which is not as pronounced as the DNA strands mentioned above. Functionalization also causes charge transfer between the tube and DNA strands, resulting in a slight upshift in the peak locations[80]. For the DNA strands, this shift is ~ 10 cm^{-1}, whereas for SDS, it is only ~3 cm^{-1}. This reconfirms tight physical wrapping of the nanotubes by DNA strands. Figure AP 2 (Appendix) shows summary (average and standard

deviation) of Raman data collected from multiple (~5) scans and multiple samples. The qualitative features described above represent the general behavior exhibited by these specimens.

The G^+ peak can be fitted with a Lorentzian, whereas G^- peak requires a broad Breit-Wigner-Fano (BWF) lineshape and two Lorentzian, as shown in the *inset* of Figure 2.3(b). This feature is a signature of metallic nanotubes and arises due to the coupling of phonons with the continuum of electronic states near the Fermi level of metallic nanotubes[84]. Semiconducting tubes, on the other hand, do not exhibit such feature and in that case both G^+ and G^- peaks can be fitted with Lorentzians.

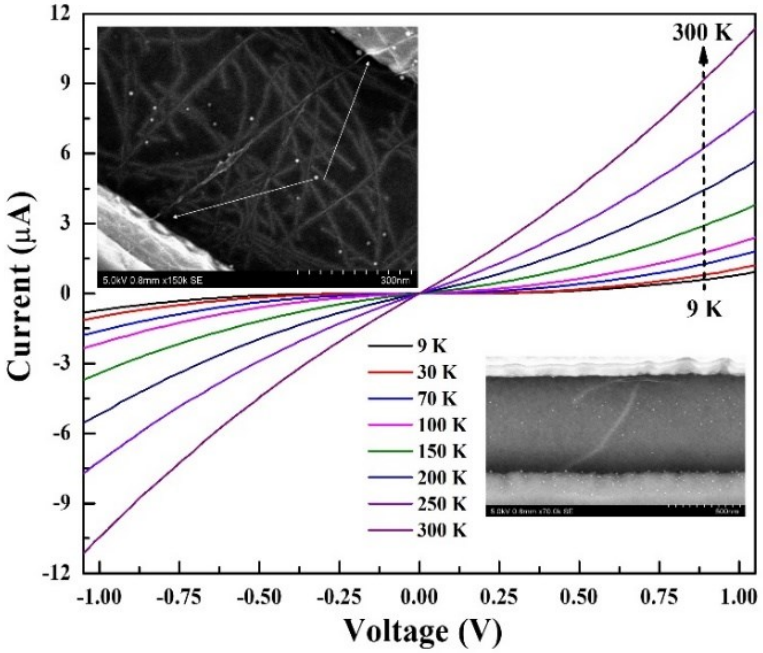

Figure 2. 4: *Temperature-dependent current−voltage (I− V) characteristics of CNTs wrapped with d(GT)$_{200}$ at zero magnetic fields. Top-left inset shows multiple tubes between the contacts, but only very few are electrically connected with both contacts (shown by arrows). Bottom-right inset shows only one tube connected between the contacts.*[137]

Figure 2.4 shows the two-terminal temperature-dependent I-V characteristics for d(GT)$_{200}$ wrapped nanotubes. Contact resistances of such devices have been characterized before by our group in their work[14] and have been found to be negligible. This could be attributed to the annealing step described above, and a similar effect has been reported by other groups as well[162,163]. For this study, the channel length is set to ~750 nm, as seen in Figure 2.4 *insets*. Multiple tubes could be present in between the contacts but only very few are electrically connected with both contacts (Figure 4, top-left *inset*). Diluting the dispersed nanotube solution results in fewer tubes between the contacts (Figure 2.4, bottom-right *inset*). Non-linear I-V characteristics, typical

of single-wall nanotubes, have been observed. Temperature dependence of I-V clearly shows a semiconducting trend, as observed before in similar devices[164]. This apparently contradicts the Raman data reported above, which shows a metallic nature. However, perturbation due to helical functionalization could lift the degeneracy of the original sub-bands and create a bandgap. For this measurement, one contact is Au, and another contact is Ni, which serves as a spin detector as described below.

DNA molecules are known to exhibit large-bandgap semiconducting behavior, even at room temperature[165,166]. Typically, in the low bias range, DNA strands exhibit very low conductance and essentially behave as an insulator[165,166]. This is in contrast with the data observed in Figure 2.4, which shows low but measurable conductance in this range. This indicates that the primary transport channel is the nanotube and not the DNA strands on the periphery. This is consistent with the device geometry, since, direct one-step coherent tunneling through 750 nm wide potential barrier (due to DNA strands) is extremely unlikely[167]. Also, in such cases, the current should be almost independent of temperature, which we do not observe. Incoherent thermally activated hopping could provide another transport mechanism through the DNA strands[167], but this should be ineffective at low temperatures, and even at higher temperatures DNA strands still behave as insulators[166]. Further, in the case of DNA, the conductance gap at low bias tends to increase with temperature[165], which is qualitatively different from what we observe. Thus, in our case, carrier transport appears to be taking place *via* the nanotubes. The role of DNA functionalization is to induce an inversion-asymmetric helical potential on the charge carriers, which is expected to result in a finite non-zero spin polarization *via* spin-orbit coupling.

Since nanotubes are the primary transport channels, the I-V scans are highly reproducible with negligible differences between multiple scans taken under the same condition (not shown). We note that while ssDNA-SWCNT hybrids are unstable above 80^{o} C in aqueous solutions, the critical temperature for these hybrids adsorbed on SiO_2 is much higher[100]. Using a binding energy value of 0.7eV for ssDNA-SWCNT hybrids, we can estimate the critical temperature for instability on SiO_2 substrate, which turns out to be approximately few 1000 K. This value is significantly larger than our annealing temperature (200^{o} C or 473K), and hence no DNA unwrapping is expected. We have examined the nanotubes by AFM after annealing and the same helical wrapping

pattern was observed, indicating that the DNA molecules were not destroyed as a result of annealing.

Figure 2.5 shows I-V characteristics at 9K and 21K for two distinct polarities of magnetic field values +1.2T and -1.2T. A magnetic field is applied in-plane and is enough to saturate the magnetic Ni contact, which has a coercive field of ~100G. A clear splitting in the I-V curve has been observed, which indicates the presence of magnetoresistance (MR) effect in these devices. The *insets* in Figure 2.5 show the resistance ($R = dV/dI$) as a function of bias (V), computed by numerical differentiation of the I-V characteristics. At a given bias, a significant split in the resistances has been observed, especially in ± 0.1V range. The MR effect gradually disappears as the bias is increased. Also, at higher temperatures (such as 70K), the MR effect is not present as shown in Figure AP 3(a) (Appendix).

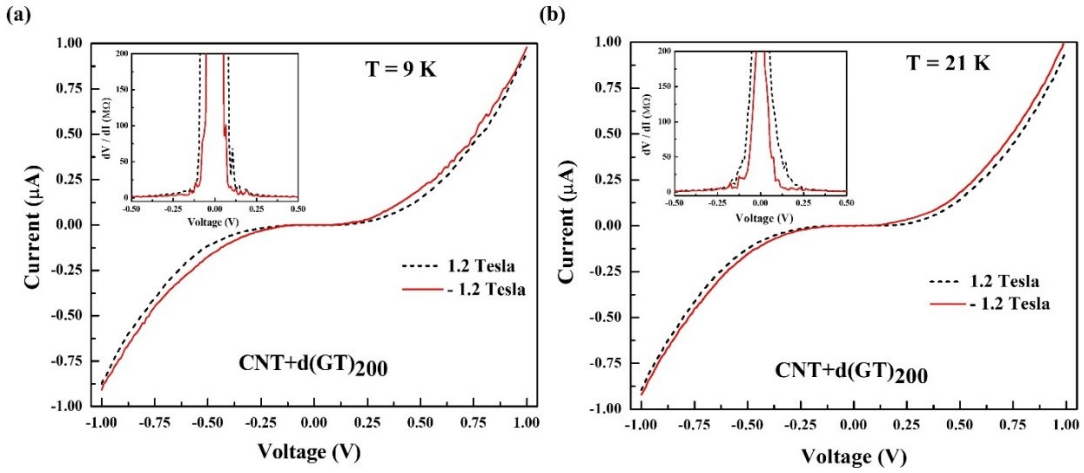

Figure 2. 5: *Typical I−V characteristics at +1.2 and −1.2 T, showing the presence of MR at 9 K (a) and 21 K (b). (insets) Variation of device resistance as a function of bias.*[137]

As indicated above, the I-V scans are highly reproducible, and the observed splitting cannot be attributed to statistical variations. As an example, Figure AP 3(b) (Appendix) shows multiple scans at each magnetic field, the average value, and the standard deviations. The magnetic field dependent splitting is still observed.

The magnitude of the MR value (defined as $R(1.2\,T) - R(-1.2\,T)/R(-1.2\,T)$ is significant ~ 90% at 0.1V and cannot be explained by AMR (anisotropic MR) of Ni contact, which is typically ~1%. Also, as the temperature-dependent I-Vs indicate, the series resistance of the metallic contacts does not play any perceptible role in the overall device resistance. Such a large

MR signal is indicative of spin-dependent transmission at the Ni contact, which acts as a spin detector. This data indicates that $d(GT)_{200}$ strands are capable of spin filtering, consistent with existing literature. Using the Julliere[32] model, we estimate a spin polarization value of 79% at -0.1 V and 21K. Since $d(GT)_{200}$ functionalization creates longer tubes, it is possible to perform a systematic length-dependent study of spin polarization using these tubes and compare them with theoretical models.

2.6 Conclusion

In conclusion, we have reported the successful and reproducible fabrication of individual long carbon nanotubes wrapped with single-stranded DNA. Previous studies mostly reported only submicron tubes, but our choice of fabrication parameters allows us to significantly expand (~2-4 x) the length range of the tubes. The wrapped tubes have been characterized extensively using various techniques, and they reveal a high degree of dispersion of nanotubes, complete DNA wrapping along nanotube length without any evidence of discontinuity and tight physical contact between DNA and nanotube. Such features are highly desirable for subsequent device fabrication. Long DNA-wrapped tubes are becoming increasingly important in the emerging area of chiral spintronics, where it has been found that longer tubes can increase the spin polarization of charge carriers in electrical transport devices. In addition, our use of longer DNA strands results in fewer discontinuities in the helical potential profile compared to the shorter DNA strands reported so far in the literature. Initial data indicates the presence of spin filtering in these systems. Our fabrication process enables further investigation in this area (especially, length dependence of spin filtering; chapter 4), and can potentially result in highly spin-polarized nanoscale systems, which will find applications in ultra-small spintronic devices and circuits.

Chapter 3. Effects of CISS on carrier transport in DNA-functionalized CNTs[‡]

3.1 Introduction

Since helical coupling with DNA results in spin polarization in a DNA-CNT hybrid (as discussed in previous chapters), tuning of the DNA−CNT interaction is expected to affect carrier spins in nanotubes. The CISS effect is also known to induce spin polarization, which is coupled with the carrier's momentum direction[57,60], and therefore, in one-dimensional systems, such as nanotubes, momentum flip must be accompanied by a simultaneous spin flip. This spin-momentum locking can have a profound impact on charge transport in nanotubes, as backscattering due to phonons and disorder will be suppressed because these mechanisms are spin-independent. Helical wrapping of nanotubes with DNA is mediated by $\boldsymbol{\pi}$-$\boldsymbol{\pi}$ stacking between the DNA bases and nanotube sidewalls, and also by electrostatic and torsional interactions within the sugar-phosphate backbone[168,169]. It is well-known that different base sequences exhibit significantly different interaction strengths and binding energies with nanotubes[78,79,150,168–171]. This raises the intriguing possibility of engineering the helical coupling *via* tailor-made DNA sequences and thereby tuning the degree of CISS-induced spin-filtering. Using specific sets of DNA sequences that exhibit different degrees of coupling with nanotubes, here we demonstrate that this can indeed be achieved. Due to the spin-momentum locking, charge transport properties varying significantly among these samples.

We have tested SWCNTs functionalized with some simple patterns of primary nucleobase sequences such as $d(AC)_{15}$, $d(CC)_{15}$, $d(GT)_{15}$, and $d(TT)_{15}$. It has been reported that oligonucleotides based on thymine bases (such as $d(GT)_{15}$ and $d(TT)_{15}$) are more effective in dispersing and functionalizing nanotubes[78,79], which can be partly attributed to the higher binding affinity of G/T with nanotubes compared to A/C[172]. AFM and Raman characterizations reported in this work also support this observation. In this work we report a systematic study of single-wall nanotubes functionalized with $d(AC)_{15}$ and $d(CC)_{15}$ strands and compare the results with data on

[‡] Parts of this chapter have been published in – Rahman, Md. Wazedur, Firouzeh, S., Mujica, V. and Pramanik, S. Carrier Transport Engineering in Carbon Nanotubes by Chirality Induced Spin Polarization, ACS Nano 2020, 14, 3, 3389-3396.

$d(GT)_{15}$ and $d(TT)_{15}$[14,15,137]. Multiple (>20) samples have been tested in each category and systematic differences in spin filtering and charge transport have been observed depending on the functionalization moiety.

3.2 Experiment

CNT-DNA functionalization has been described earlier (Chapter 2). Briefly, HiPco single wall bundled CNTs (0.7-1.2 nm diameter) and single-stranded DNA (such as $d(AC)_{15}$, $d(CC)_{15}$, $d(GT)_{15}$ and $d(TT)_{15}$) solutions were purchased commercially, mixed, followed by ultrasonication and centrifugation. A drop from the supernatant is dispersed on a SiO_2 substrate. Nanotubes are predominantly semiconducting, as revealed from the Raman data in Figure 3.1. Temperature-dependent studies described later also show semiconducting behavior.

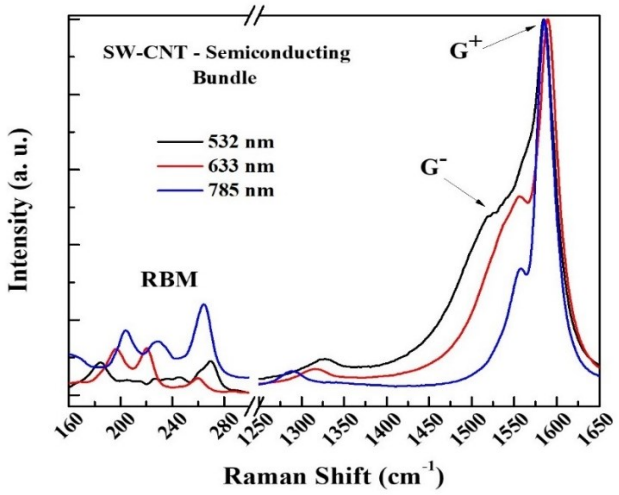

Figure 3. 1 *Raman characterizations carried out at multiple laser frequencies on as-purchased bundled nanotubes. No Breit-Wigner-Fano (B-W-F) lineshape has been observed at any frequency, indicating that the nanotubes are predominantly semiconducting. Defect peak (~ 1340 cm^{-1}) is negligible for bundled specimens.*[138]

The ssDNA specimens used in this study have 30 bases, according to the vendor specifications. The sequences used are as follows:

$d(GT)_{15}$: GTGTGTGTGTGTGTGTGTGTGTGTGTGT

$d(TT)_{15}$: TTTTTTTTTTTTTTTTTTTTTTTTTTTTTT

$d(AC)_{15}$: ACACACACACACACACACACACACACAC

$d(CC)_{15}$: CCCCCCCCCCCCCCCCCCCCCCCCCCCCCC

Since each base is approximately 0.33nm, the total length of each strand is estimated to be 30 x 0.33 = 10 nm, which is sufficiently long to coil around the circumference (~ 3 nm) of a ~1 nm diameter nanotube.

3.3 Result

Figure 3.2(a) (also Figure AP 4 in Appendix shows the typical AFM image of DNA-wrapped nanotubes dispersed on a SiO_2 substrate. Alternating bands of high and low regions are observed along nanotube lengths (Figures 3.2(a) *inset*), indicating helical wrapping. A typical nanotube device is shown in Figure 3.2(b). Minimum contact distance (~ 750 nm) is larger than average tube length (~ 500 nm), which significantly reduces the number of connected tubes. Interestingly, $d(AC)_{15}$ and $d(CC)_{15}$ have wider wrapping pitch compared to $d(GT)_{15}$ and $d(TT)_{15}$, resulting in fewer helical turns per unit length (Figure 3.2(c)).

Figure 3.2(d) shows typical Raman scans with signature peaks at ~ 1590 cm^{-1} (G^+) and 1545 cm^{-1} (G^-), indicating longitudinal and transverse vibrations of the nanotube graphitic lattice respectively[80]. In the low-frequency range (150-300 cm^{-1}) typical radial breathing modes have been observed. Defect (*D*) peak at ~1340 cm^{-1} is negligible for bundles (also, Figure 3.1), though a small *D* peak emerges after functionalization due to the broken tubes as a result of dispersion. DNA wrapping tends to narrow the width of the G-band as a result of tube isolation. Individual, non-functionalized ("bare") CNTs also exhibit similar Raman behavior as in Figure 3.2(d)[80].

As expected, G^-/G^+ intensity ratio gets reduced as a result of helical functionalization (Figures 3.2(d), (e)), because helical binding restricts transverse vibrations of the carbon atoms[173]. Data collected over ~20 samples in each category (Figure 3.2(e)) shows that $d(AC)_{15}$ and $d(CC)_{15}$ functionalizations tend to have higher G^-/G^+ ratio than $d(GT)_{15}$ and $d(TT)_{15}$, though all of them are smaller compared to bundled tubes. This systematic trend indicates that $d(AC)_{15}$ and $d(CC)_{15}$ functionalizations have weaker interaction with nanotubes (transverse vibration less suppressed) compared to $d(GT)_{15}$ and $d(TT)_{15}$. We note that this is consistent with the wrapping pitch differential observed in Figure 3.2(c).

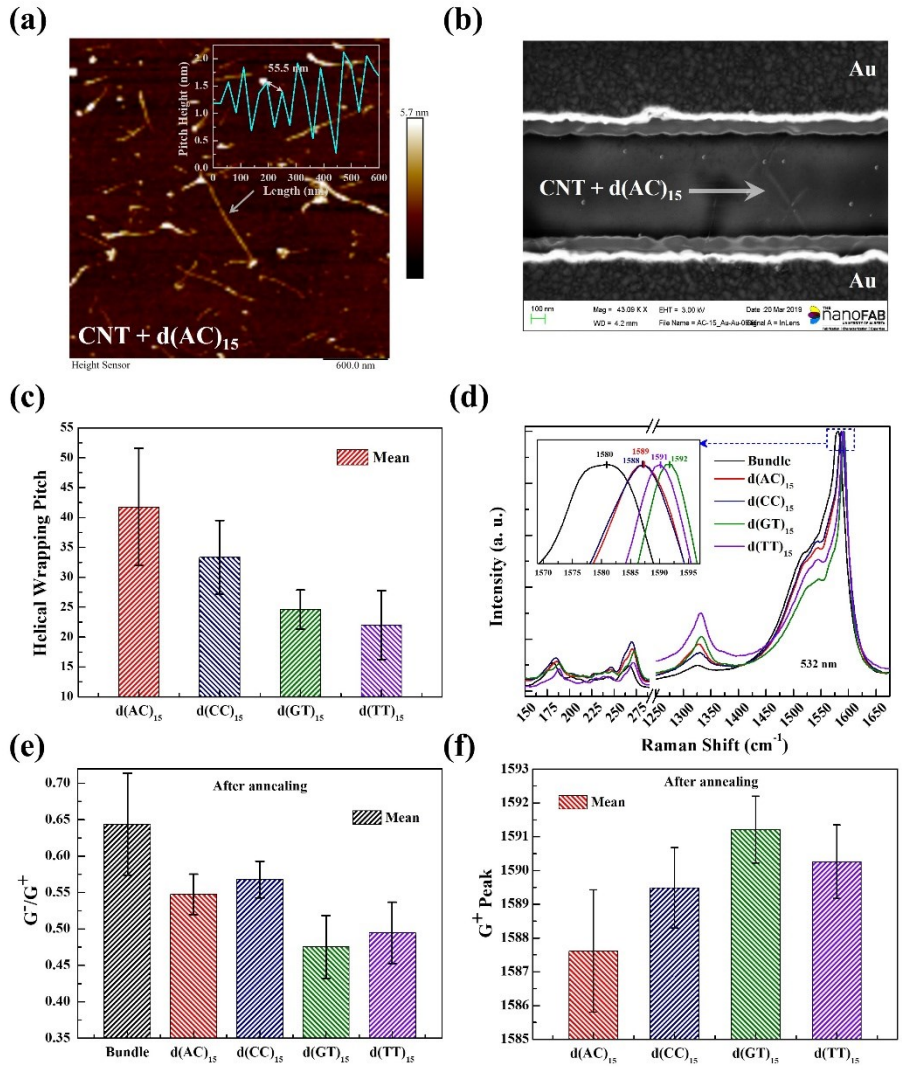

Figure 3. 2 (a-b) *Typical images of DNA-wrapped CNTs and devices.* ***(c)*** *Distribution of helical pitch for each functionalization.* ***(d–f)*** *Raman characterizations.*[138]

Figure 3.2(d) *inset* shows upshift of G^+ peak frequency (compared to bundle), which is indicative of charge transfer between the nanotube and DNA[80,173–176]. Larger shifts tend to occur for $d(GT)_{15}$ and $d(TT)_{15}$ (Figure 3.2(f)), which again indicates closer proximity of $d(GT)_{15}$ and $d(TT)_{15}$ strands with the nanotubes as compared to $d(AC)_{15}$ and $d(CC)_{15}$. All DNA strands have "acceptor" type charge transfer with the tube[80,173] and hence any difference in charge transport behavior (described below) cannot be explained by the difference in doping type. We note that such charge transfer effects are generally small[174–176], and not significant enough to affect the transport properties in any case. Thus, based on all the above observations we conclude that

$d(GT)_{15}$ and $d(TT)_{15}$ result in "strong coupling" with CNTs, whereas $d(AC)_{15}$ and $d(CC)_{15}$ result in "weak coupling".

Figures 3.3(a)-(d) show typical temperature-dependent current-voltage characteristics over ~ 10-300K at zero magnetic field (Au contacts). Planar resistances of the contacts (Au or Ni) have been characterized separately (not shown) and they are ~6 orders of magnitude smaller than the nanotube devices and show metallic behavior. This confirms that contact resistances don't play any significant role in the transport measurements. We observe a semiconducting trend with temperature in all cases, which attests to the predominantly semiconducting nature of the nanotubes. We note that the helical DNA strands are insulating in nature, especially on a length scale employed in this study (~750 nm). Currents in our devices are ~ 10-100 μA, which cannot be explained by transport *via* DNA strands. Thus, in these experiments' nanotubes are the medium of charge transport.

Strong temperature-dependent resistance is indicative of hopping conduction. Figure 3.3(a)-(d) *insets* show fitting with variable range hopping (VRH) model[177], based on the equation $R(T) = R_0 \exp (T_0/T)^{1/d+1}$ for $d = 2$ (also, Figure AP 5 in Appendix for $d = 1, 3$), with linear fit over a wide range. For $d(AC)_{15}$ and $d(CC)_{15}$ functionalized nanotubes, we observe small deviations from the linear fit at low temperatures (below ~ 50K) (Figures 3.3(a), (b) *insets,* Figure AP 5 in Appendix). However, for $d(GT)_{15}$ and $d(TT)_{15}$ functionalized samples, the deviation at low temperatures (below ~50K) is significantly larger for all values of d (Figures 3.3(c), (d) *insets,* Figure AP 5 in Appendix), suggesting that the hopping events being influenced by some other factor in these cases. Figure 3.3(e) highlights this difference. Multiple samples (~8) have been tested in each category and this feature has been observed. As mentioned above, charge transport in all cases must involve transport through the nanotubes (and *not* the DNA strands), which makes the drastically different temperature-dependence of *I-V* rather unusual, and hints in the direction of an indirect interplay of the nanotubes with the DNA strands.

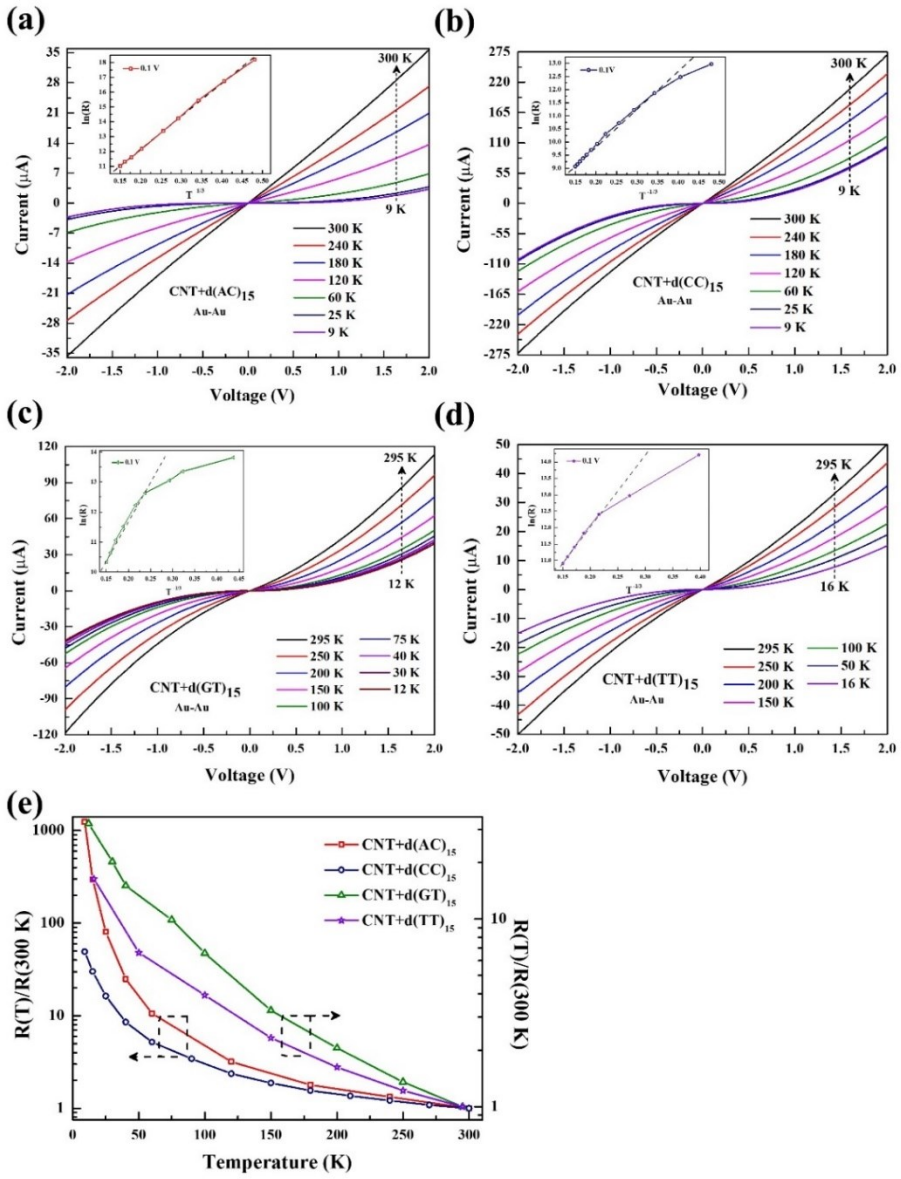

Figure 3. 3 (a−d) *Current−voltage (I−V) characteristics for different functionalizations (B = 0). Insets show fitting with the VRH model for d= 2.* ***(e)*** *Temperature dependence of resistance (0.1 V bias) for different functionalizations. The difference is most pronounced at lower temperatures (<50 K).*[138]

The observed difference cannot be attributed to the difference in nanotube chiralities. For each type of functionalization, several devices have been tested with varying nanotube chiralities (albeit primarily semiconducting, as described before). The data solely depends on the type of functionalization, even though these entities don't directly participate in carrier transport due to their insulating nature. Also, the measured current values are roughly within the same range, with no systematic difference based on functionalization. Any variation in the current value is due to the difference in the exact number of connected tubes. These rules out trap distributions as a

possible cause for the observed difference. We note that studies on *isolated*, non-functionalized ("bare") SWCNTs have shown similar strongly temperature-dependent transport[178], which has been explained by VRH. However, no deviation at low temperatures was observed. Non-functionalized SWCNT networks also show qualitatively similar behavior such as VRH and no deviations at low temperature.[179,180]

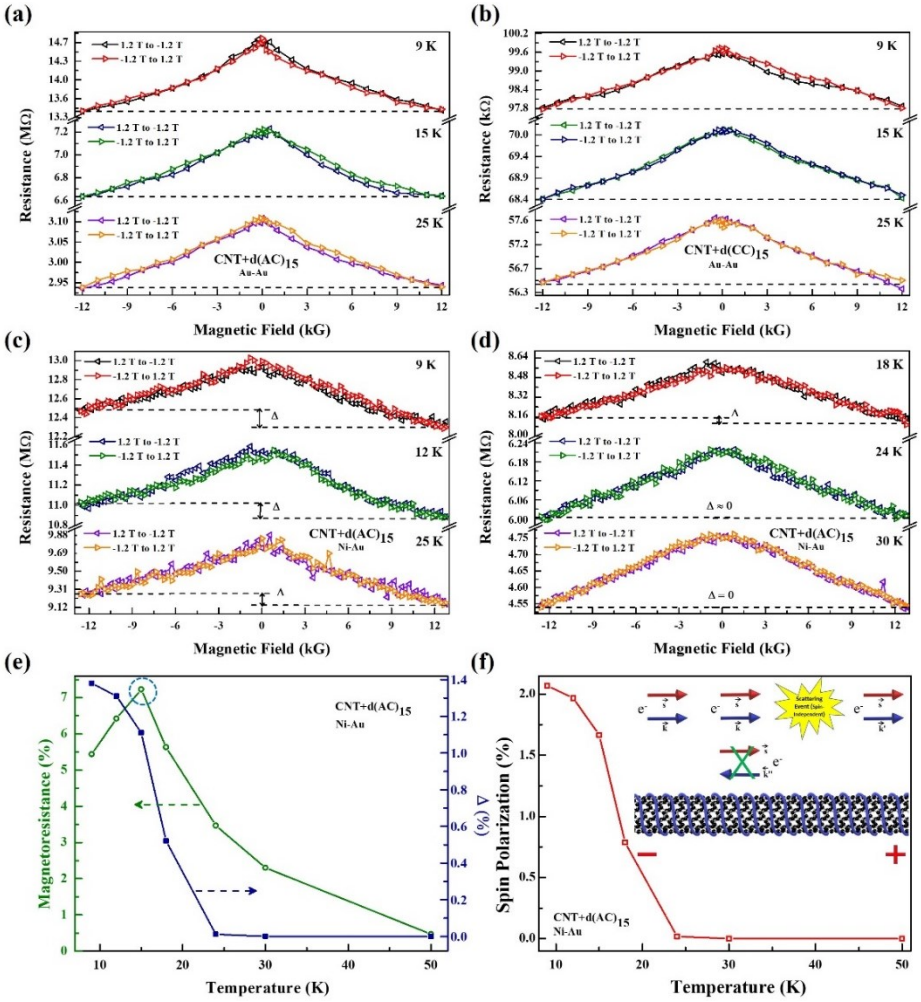

Figure 3. 4 (a-b) *Symmetric MR of (a) d(AC)$_{15}$ and (b) d(CC)$_{15}$ functionalized nanotubes with Au−Au contacts.* ***(c-d)*** *Asymmetric MR of d(AC)$_{15}$-wrapped tubes with Ni−Au contacts. Applied bias is 0.5 V in all cases.* ***(e)*** *Temperature dependence of background MR and Δ. Nonmonotonicity has been observed in the background MR, indicated by the dashed circle.* ***(f)*** *Spin polarization (estimated from Δ) vs temperature. (inset) Schematic description of suppression of backward scattering due to strong spin momentum locking.*[138]

Figure 3.4(a), (b) show the magnetoresistance (MR) responses of d(AC)$_{15}$ and d(CC)$_{15}$ functionalized samples with non-magnetic Au contacts. In this case, no spin-filter related MR is expected, even if CISS-induced spin-polarized carriers are present in the system. As seen in Figures 3.4(a), (b), a negative background MR of ~ 1-10% is observed, which is *symmetric* with

respect to the applied magnetic field. The MR signal is non-monotonic in the low-temperature range and gradually disappears at higher temperatures (Figure 3.4(e)). Earlier studies on $d(GT)_{15}$ and $d(TT)_{15}$ functionalizations ("strong coupling" case), however, did not report any such background MR[14,15,137] (also, Figure AP 6 in Appendix). This difference is noteworthy, since as mentioned above, in all cases transport occurs through nanotubes with nominally identical electrical properties, yet such systematic differences have been observed.

To detect any CISS-induced spin polarization, we have replaced one of the contacts with Ni, which acts as a spin detector. While a "two-terminal" detection is precluded in the linear response regime, no such restriction exists in the non-linear regime (present case)[181]. According to another study, in such a two-terminal configuration with only one magnetic electrode, true equilibrium is reached with CISS-induced spin accumulation in the non-magnetic electrode[60]. Magnetization reversal leads to non-zero MR in such cases[60].

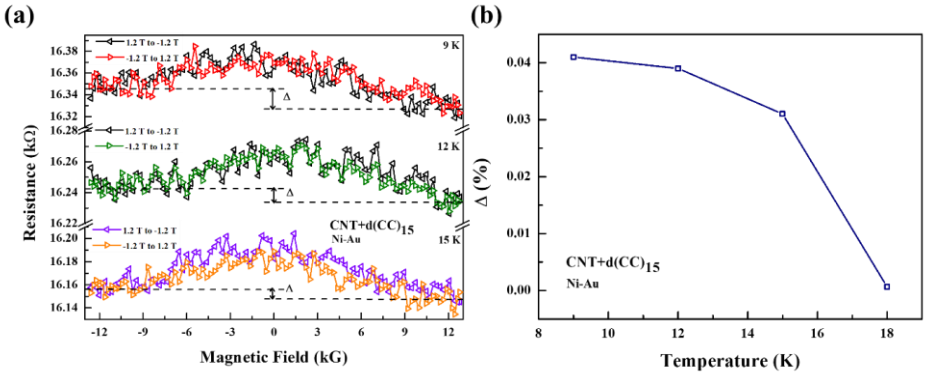

Figure 3. 5 *Asymmetric MR of $d(CC)_{15}$ wrapped tubes with Ni-Au contacts. The asymmetry (Δ) disappears gradually at higher temperatures.*[138]

Figures 3.4(c), (d) (and Figure 3.5) show MR data from $d(AC)_{15}$ (and $d(CC)_{15}$) functionalized nanotubes contacted with Ni and Au electrodes. The background MR observed above is still present. Interestingly, device resistance has been found to be *asymmetric* (indicated by *Δ* in Figures 3.4(c), (d)) relative to positive and negative magnetic fields. No such asymmetry was observed in Figures 3.4(a), (b). Earlier reports on $d(GT)_{15}$ and $d(TT)_{15}$ functionalizations ("strongly coupled" case), reported asymmetric MR response[14,15,137], which was attributed to spin-polarized carriers.

This asymmetry indicates that charge transmission is unequal for positive and negative magnetizations of Ni, which implies that the charge carriers are spin-polarized for $d(AC)_{15}$ and

$d(CC)_{15}$ wrapping. Spin polarization estimated from this asymmetric MR component (Δ)[14,15,137] turns out to be ~2-5% at low temperature and bias (Figure 3.4(f)), significantly smaller than ~70%, observed for $d(GT)_{15}$ and $d(TT)_{15}$ functionalizations. In the latter cases, spin-dependent MR is also much stronger (~100%)[14,15]. Thus, strong DNA-CNT coupling results in stronger spin polarization whereas weaker coupling produces weaker spin polarization.

The symmetric background negative MR observed in the weak-coupling case (Figures 3.4(a), (b)) is reminiscent of weak-localization (WL), which manifests in weakly-disordered metallic systems[88]. In such systems, backscattering (or reflection) probability of an electron is enhanced due to constructive interference between *forward and backward* elastic scattering paths[88]. In the presence of an external magnetic field, phase shift is introduced between these interfering paths, which weakens or destroys the constructive interference and reduces the reflection probability, leading to negative MR. If the strong spin-orbit coupling is present, the interference is destructive, and the magnetic field results in a positive MR (weak antilocalization or WAL)[88].

In the present context where transport is due to VRH, *forward and backward hopping paths* interfere constructively and result in a certain localization length. The applied magnetic field breaks time-reversal symmetry between forward and backward hopping paths (similar to weak localization in metallic systems), thereby increasing the localization length and generating a negative MR[182]. In the presence of spin-orbit interaction, localization length is reduced under an applied magnetic field, which results in positive MR[182].

We note that in the VRH regime, negative MR can also originate due to quantum interference between *forward* hopping paths[183,184]. This mechanism is characterized by a linear magnetic field dependence, especially at low fields (< 1T) and in nanotube samples[180,184]. However, in our case, the MR curves are non-linear, as shown in Figure AP 7 (Appendix). Due to this qualitative difference, this mechanism is unlikely to be operative in our case.

Negative MR can also originate in graphitic structures due to the enhancement of the density of states when the Fermi level falls into a partially filled Landau level[185] or, due to magnetic field induced Zeeman splitting[186]. These, however, are unlikely in our case, because observation of negative MR is correlated only with the nature of functionalization. This indicates that the CNT band structure is not the underlying cause.

As mentioned above, the negative background MR was never observed in $d(GT)_{15}$ or $d(TT)_{15}$ functionalized samples[14,15,137] (also, Figure AP 6 in Appendix) even though in both cases carrier transport occurs *via* the tubes and the strands do not directly participate in charge transfer. Such differences can be explained by invoking CISS, in which spins are locked with momentum direction. In $d(GT)_{15}$ and $d(TT)_{15}$ samples CISS effect is strong, implying significant spin-momentum locking. Any backward hopping in these samples will also require a simultaneous spin flip. This significantly reduces the probability of backward hopping since most scattering events are spin independent. As a result, the interference-based MR mechanism described above is suppressed. In the case of $d(AC)_{15}$ and $d(CC)_{15}$, however, the CISS effect is weak, and hence spin-momentum locking is not significant. As a result, carriers have a higher probability of momentum-flip, and negative MR is readily observed. These processes are schematically shown in Figure 3.4(f) *inset*.

Similar to $d(GT)_{15}$ or $d(TT)_{15}$ wrapped nanotubes[14,15,137], CISS-induced MR (Δ) and resultant spin polarization have been observed to decay with temperature even in the case of $d(AC)_{15}$ and $d(CC)_{15}$ (Figure 3.4(e), (f), Figures 3.5). This is because spin polarization is induced in the carriers in nanotubes, and it is well known that in the nanotube medium spin polarization decays with temperature[187]. As expected, the symmetric background MR observed in Figures 3.4(a), (b), which was attributed to the interference effects between forward and backward hopping paths, also decays with temperature (Figure 3.4(e)). This is reminiscent of decay of WL MR in metallic systems with temperature, due to phase-breaking phonon scattering events[88]. However, counterintuitively, a unique *non-monotonicity* exists at low temperatures with an MR peak at ~15K (Figure 3.4(e)). Above ~15K, spin polarization is weak and gradual decrease of the background MR can be attributed to the phonons. However, below this temperature, spin polarization is comparatively strong, which tends to suppress backward hopping (as discussed before) and hence reduces the background MR signal. This results in a non-monotonic temperature dependence of the background MR.

The difference in low-temperature transport characteristics (Figures 3.3(e)) is consistent with the physical picture presented above. As the temperature is increased, carriers tend to become more delocalized due to electron-phonon interaction, resulting in lower resistance[188]. Delocalization occurs when the electrons are scattered by the phonons *both* forwards and

backwards[188]. In Figure 3.3(e), we have observed this trend, where device resistance decreases by a factor of ~10 (for all samples) as the temperature is increased from 50K to 300K. In this temperature range, no CISS-induced spin polarization is present (Figure 3.4(f)). The emergence of strong CISS at lower temperatures (in $d(GT)_{15}$ and $d(TT)_{15}$ samples) suppresses phonon-induced backward hopping events, and hence phonons become less effective in delocalizing carriers. Therefore, at low temperatures, the resistance of CISS samples decreases weakly as the temperature is increased. The CISS effect, however, is weaker in $d(AC)_{15}$ and $d(CC)_{15}$ samples, and hence phonon-induced backward hopping events are allowed. Thus, phonons are more effective in delocalizing carriers in these samples, which results in a sharp decrease in resistance as the temperature is increased. Overall, the observed transport phenomena are consistent with the fact that electron-phonon interaction, which is the main source of thermal and decoherence effects in transport, is constrained by symmetry in the presence of spin polarization. This is because phonons do not carry spin angular momentum and hence cannot reverse the direction of spin, due to angular momentum conservation.

3.4 Conclusion

In conclusion, we have reported magneto-transport behavior in CNTs, helically wrapped with $d(AC)_{15}$ and $d(CC)_{15}$. These strands produce weaker coupling with CNTs compared to previously reported $d(GT)_{15}$ and $d(TT)_{15}$ strands. This has a significant impact on CISS-induced spin polarization in these systems. The strongly coupled and weakly coupled specimens also show significantly different charge transport behavior, which can be explained by invoking CISS. This work demonstrates CISS as a mechanism to engineer not only spin polarization but also charge transfer processes at the nanoscale.

Chapter 4. Carrier Localization and Magnetoresistance in DNA-functionalized Carbon Nanotubes[§]

4.1 Introduction

Most of the CISS systems explored so far include molecular-scale devices (primarily individual molecules or self-assembled monolayers) consisting of DNA strands[5], oligopeptides[6], helicenes[91], polymers[92], supramolecular nanofibers[95] *etc.*, all of which can be considered as insulators in terms of their bulk electronic properties. The CISS effect has also been explored in planar geometry using carbon nanotubes (CNTs) which are helically functionalized with single-stranded DNA[14,15,137,138]. Such systems offer an exciting pathway to exploit CISS, since they allow spin polarization to be induced in conductive materials through helical functionalization. In transport experiments, presence of the CISS effect is typically detected using a two-terminal setup, in which one contact is nonmagnetic (such as Au) and the other contact is magnetic (such as Ni or Co). This configuration results in different resistances in the non-linear transport regime, depending on the magnetization orientation of the magnetic contact, which is considered as a signature of CISS-induced spin polarization[8,99,181,189].

In a two-terminal measurement, the observed magnetoresistance (MR) can originate from various sources such as orbital MR of the system under consideration, spurious Hall effects due to the fringe field in the vicinity of the magnetic contacts or other effects not related to CISS. In the case of nanotubes, structural disorder or the helical functionalization can give rise to carrier localization effects, which can result in complex features in the MR data. While DNA wrapped CNTs have been studied extensively due to their various applications as biosensors[190], their transport and MR behaviour have not been systematically studied so far. In this chapter we investigate the origins of the MR effects that can coexist with the CISS signal in DNA functionalized nanotubes. Specifically, we study single wall carbon nanotubes (SWCNT) functionalized with $d(AC)_{15}$ single-strand (ss)-DNA.

[§] Parts of this chapter have been published in – Md. Wazedur Rahman, F. Seyedamin, and Sandipan Pramanik, 'Carrier Localization and Magnetoresistance in DNA-functionalized Carbon Nanotubes', Nanotechnology 32 (2021) 455001.

4.2 Results and discussions

DNA wrapped CNT samples have been synthesized by a process described in our earlier work[14,15,137,138]. Briefly, 20 nmole $d(AC)_{15}$ ssDNA oligo (Ultramer - Integrated DNA Technologies) is mixed with nuclease free water and buffer solution to prepare 1mg/ml ssDNA solution. This solution is added to 0.7 mg HiPco SWCNT bundle (0.7–1.2 nm diameter, Nano-Integris Inc.) and the mixture is kept in an ice-water bath. The mixture was ultrasonicated (Sonics, VC130 PB) for 90 min at a power level of 7 W and then centrifuged at 14000g for 60 mins to remove undispersed SWCNTs. Top part of the mixture was collected for further measurements to avoid insoluble bundled CNTs.

Figure 1(a) shows a typical AFM (atomic force microscopy - Dimension Edge) image of $d(AC)_{15}$ wrapped nanotubes dispersed on SiO_2 substrate. Most of the bundled CNTs are converted into isolated tubes. The length of ssDNA-CNTs is ~ 1–3.5 μm. Alternate regions of dark and bright bands are observed, which correlates to regions of lower and higher altitudes relative to the substrate and hence indicate helical wrapping (Figure 1(a) *inset*).

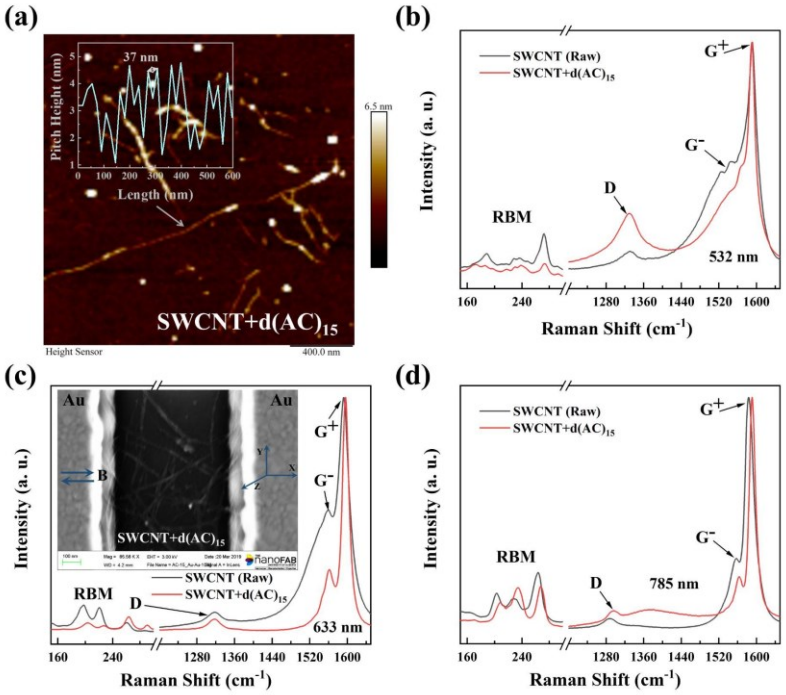

Figure 4. 1 (a) *Typical AFM image of $d(AC)_{15}$ wrapped SWCNTs. Height variation along nanotube length is shown in the inset.* ***(b)-(d)*** *Raman characterizations before and after DNA wrapping at different laser wavelengths (532nm, 633 nm and 785 nm). Characteristic peaks have been indicated. Inset in* ***(c)*** *shows a typical scanning electron microscopic (SEM) image of the final device. Magnetic field is applied in-plane, as shown.*[139]

The wrapped tubes have been characterized using Raman spectroscopy (532 nm, 633 nm, and 785 nm laser), and the results are shown in Figures 4.1(b)-(d). The key features are the G band (which consists of G+ and G- peaks at ~ 1590 cm^{-1} and ~ 1560 cm^{-1} respectively), and the so-called radial breathing mode (RBM), which manifests at 150–300 cm^{-1} range. Comparison with the raw (unfunctionalized) nanotubes shows that the ratio of G-/G+ peak intensity is reduced as a result of helical functionalization. Since the G+ and G- peaks represent longitudinal and transverse vibrations of the hexagonal graphitic lattice of CNT respectively, it is expected that helical functionalization would suppress the transverse vibration and hence suppress the G- peak, resulting in lower G-/G+. The G+ peak also experiences an upshift as a result of functionalization. This is indicative of fractional charge transfer from the CNT to DNA, presumably due to π-π stacking interactions. The G band as a whole is narrowed (compared to the raw CNT bundle) as a result of functionalization, which is due to isolation of nanotubes. The emergence of a small D (defect) peak at ~ 1320 cm^{-1} after functionalization is due to the broken ends of the dispersed tubes.

For transport measurements, Au-Au and Ni-Au contact pairs (thickness ~ 100 nm, contact distance ~ 750 nm) were photolithographically patterned on top of SiO_2 (500nm)/Si wafer. A drop of ssDNA-CNT solution was placed between the contacts and kept for 15 min., followed by thorough rinsing with DI water to remove the excess tubes. Finally, the devices were vacuum annealed (200^{o}C for 30 mins) to improve the contacts between electrodes and ssDNA-CNT. A scanning electron microscope (SEM) image of the final device structure is shown in Figure 4.1(c) *inset*. We note that very few nanotubes have been contacted by both electrodes and hence participate in conduction, whereas the rest do not.

Current-voltage (I-V) characteristics of these devices were measured over a wide temperature (9K–300K) and magnetic field (± 12 kG) range. Magnetic field is applied in-plane, as depicted in Figure 4.1(c) *inset*. Figure 4.2(a) shows typical I-V response as a function of temperature at zero magnetic field. The I-V curves are nonlinear (especially at low temperatures) and exhibit semiconducting behavior, with device resistance decreasing more than an order of magnitude as the temperature is increased from 9K to 300K (Figure 4.2(a) *inset*). Such behavior has been reported before in carbon nanotube films or networks and is commonly attributed to hopping conduction[180,191,192]. In case of nanotubes, small structural disorders, or surface functionalizations can result in localized carriers, with electron wavefunction $\psi(r)$ at location r

decaying exponentially with the distance $|r - r_i|$: $\psi(r) \sim \exp(-|r - r_i|/\xi)$, where r_i is the center of the localized wavefunction and ξ is the so-called "localization length" (or the decay length of a localized carrier's wavefunction). Carrier propagation can be viewed as thermal or electric field assisted hops between these localized states. Probability of hopping decreases exponentially with the distance between the localized states and also depends on the thermal factor $\exp(-\Delta E/k_B T)$, where ΔE is the energy difference between the two states. In the case of CNT films (or, networks) studied in literature, the contact points between the nanotubes act as potential barriers or scattering centers, which are responsible for carrier localization[180,191–194]. However, in the present case, the tubes are mostly separated from each other as a result of DNA functionalization (as seen from Figure 4.1(a)), and hence tube crossings are minimized, though not completely eliminated. The primary reason for carrier localization in the present case is due to the interaction of the DNA strands with the tubes as well as any other minute amount of structural defect. Charge transport primarily occurs through hopping between the localized states, which are created by the helical potential due to the DNA wrapping[195]. The DNA strands are insulating, hence direct charge transport through these molecules over a large distance (~ 750 nm) is unlikely. We note that the planar resistances of the metallic contacts are ~ 4 orders of magnitude smaller than the device resistance and exhibit linear, metallic behavior with temperature (Figure AP 8 (a) in Appendix). Hence their series contribution to the above measurements is negligible.

To confirm that helical wrapping is responsible for carrier localization, we functionalized nanotubes with SDS (sodium dodecyl sulfate), which is an achiral, non helical surfactant that attaches to the walls of the nanotubes and disperses them[196]. These samples were prepared using a similar process as before *i.e.*, ultrasonication (90 min at a power of 7 W) and centrifugation (14000g for 60 min) in 1% SDS solution. In Figure AP 9 (a) (Appendix) we show the Raman characterization of these samples, which shows weak suppression of the G- peak compared to the DNA samples. This indicates relatively weak interaction of the CNTs with SDS molecules. The I-V characteristics of such dispersed, SDS-coated tubes, and temperature dependence of resistance are found to be weakly semiconducting (Figure AP 9 (b) in Appendix). In this case, resistance changes only by a factor of ~5 over the entire temperature range, whereas for DNA wrapped samples, it is typically more than an order of magnitude. Thus, DNA functionalization is responsible for carrier localization and hopping type conduction observed in Figure 4.2. In contrast, such localization effects are much weaker in case of SDS functionalized CNTs.

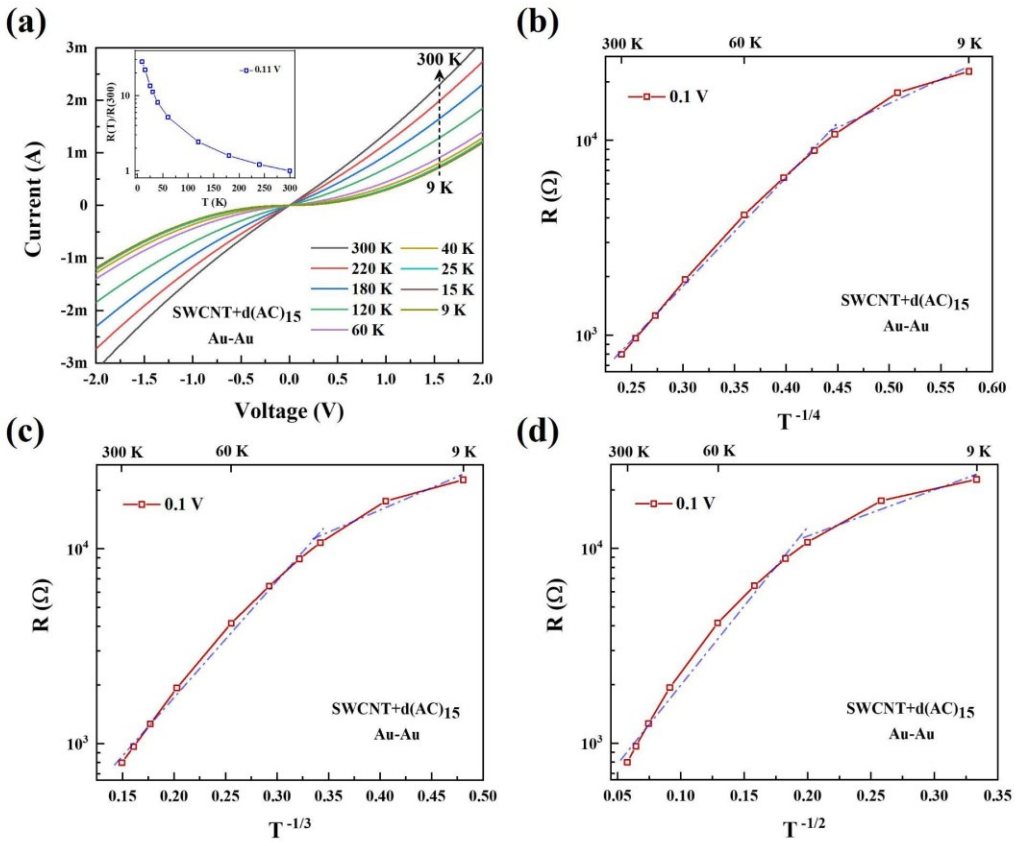

Figure 4. 2 (a) *Current-voltage (I-V) characteristics of d(AC)15+SWCNTs connected between Au-Au electrodes at B = 0. Inset - Normalized resistance as a function of temperature (at low bias ~ 0.11 V).* ***(b)-(d)*** *Fitting of the data in (a) with the VRH model for d = 3, 2 and 1 respectively.*[139]

Carrier hops between localized states lead to diffusion-type finite conductivity, which is typically described using variable-range hopping (VRH) model: $R(T) = R_0 \exp (T_0/T)^{1/(d+1)}$, where the pre-factor R_0 is determined by electron-phonon interaction, d depends on the effective dimensionality of the system and T_0 is the so-called "characteristic temperature", which is inversely dependent on localization length ξ[184,197,198]. For two- (or, three-) dimensional systems without electron-electron interaction, the exponent $1/(d+1)$ is typically ⅓ (or, ¼) and $T_0 \propto 1/g\xi^2$ (or, $T_0 \propto 1/g\xi^3$) where g is the density of states at the Fermi level[184,197]. If Coulomb interaction is present, the exponent is ½ (for both two- and three-dimensions) and $T_0 \propto 1/\xi$[180,197]. Physically, large T_0 in the VRH model implies that more thermal energy is required to induce phonon-assisted hopping between the localized states, which in turn implies higher degree of carrier localization (*i.e.*, smaller ξ). We note that typical hopping length $r_{hop} \sim \xi(T_0/T)^{1/(d+1)}$ is much larger than the average physical distance between two localized states[197].

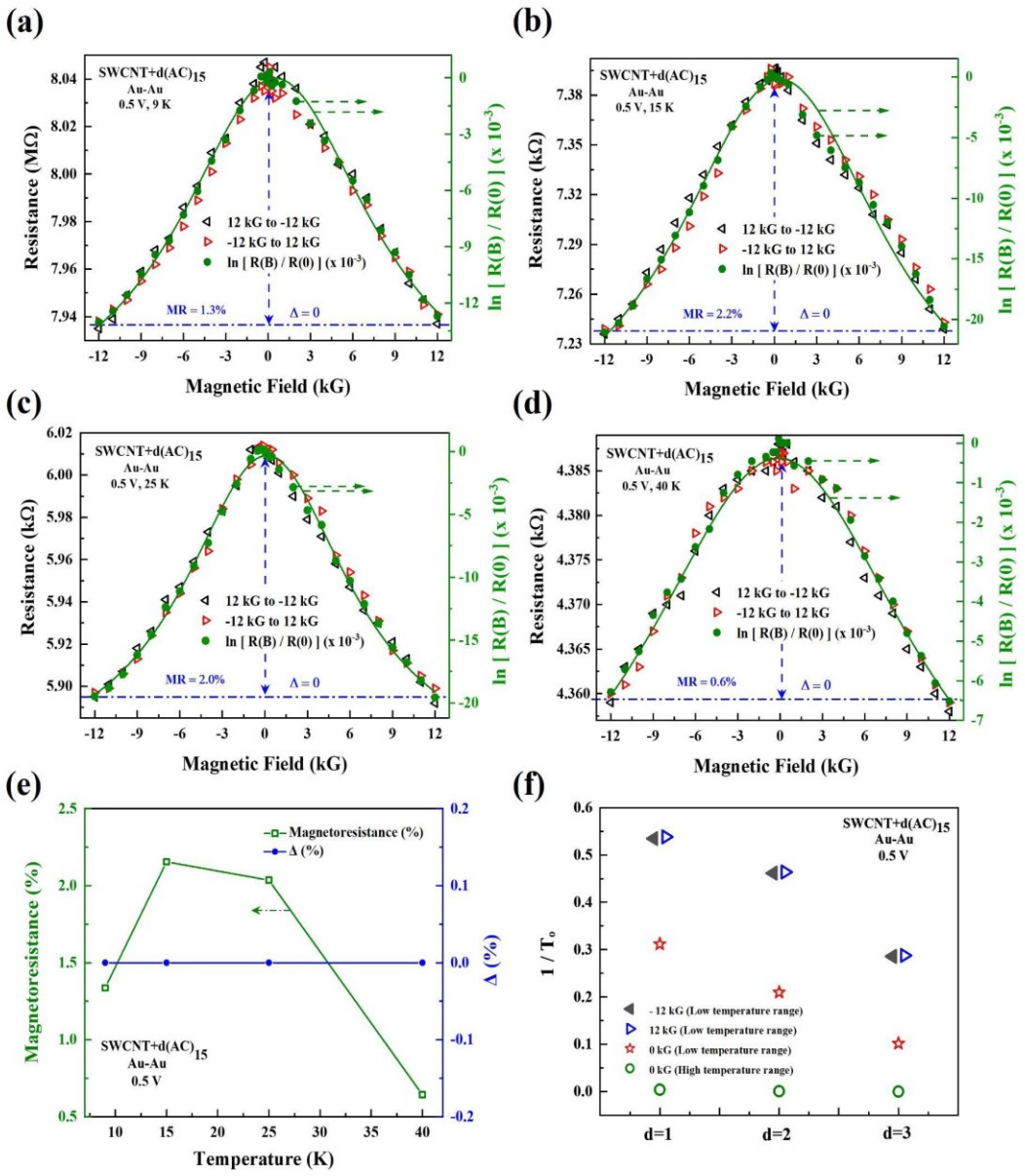

Figure 4. 3 (a)-(d) *Symmetric MR of $d(AC)_{15}$+SWCNTs with Au-Au contacts at different temperatures. MR is defined as [R (0 kG)-R (-12 kG)] / R (-12 kG) x 100%. The open triangles (red and black) represent experimental MR data for the forward and backward magnetic field scans. The green circles are the ln [R (B)/R (0)] values computed from the experimental data and the green line is a fit to the green circles.* ***(e)*** *Temperature dependence of background MR and Δ for $d(AC)_{15}$+SWCNTs with Au-Au contacts. A clear non-monotonicity is present in the MR signal. The MR is symmetric at all temperatures and hence Δ = 0. (f) Estimated 1/T0 (K-1) measured at 0.5 V under various conditions.*[139]

In Figures 4.2(b)-(d), temperature-dependent low-bias (~ 0.11V) resistance data has been fitted with the VRH model for the exponents 1/ (d +1) = ¼, ⅓ and ½ respectively. Best linear fit for the higher temperature range (60 K–300 K) has been observed for the exponents ⅓ and ¼. As the temperature is lowered, the slope decreases gradually in all cases. The observed T_0 values are

152 K in the low temperature range and 2094 K in the high temperature range for the exponent ⅓. As discussed above, low T_0 indicates that carriers gradually become less localized (higher ξ) as the temperature is lowered. This lowering of T_0 is counterintuitive and will be discussed later in this paper. We note that contrary to the present case, previous studies on non functionalized CNT networks reported linear VRH fit over the entire temperature range[180,198].

Figures 4.3(a)-(d) show the magnetoresistance (MR) data of $d(AC)_{15}$ wrapped CNTs contacted with Au-Au electrodes. Negative MR response has been observed in the ± 12 kG range of in-plane magnetic fields, which gradually disappears beyond ~ 40K. The MR is symmetric relative to the applied field *i.e.,* $\Delta = R$ (-12kG) - R (12kG) = 0 (Figure 4.3(e)). As mentioned before, series resistance of the contacts is insignificant, and they exhibit very weak positive MR at low temperatures (Figure AP 8 (b) in Appendix). Hence the observed behaviour must be understood in terms of charge transport through CNTs helically wrapped with $d(AC)_{15}$ strands. Commonly, such low-temperature negative MR effect is attributed to "weak localization", which occurs in weakly disordered metallic systems[87,199]. In such cases, the forward and backward scattered electron waves interfere constructively in the absence of a magnetic field and increases the probability of return at the starting point. When a magnetic field is applied, a phase difference is introduced between these paths, which suppresses the interference effect and leads to negative MR. In the present case, however, transport is through hopping between strongly localized states and hence alternative explanations must be sought.

In the strong localization regime, one possible origin of negative MR is due to forward interference of electrons undergoing tunnel hops.[197,200] According to this model, probability amplitude of hopping between an initial and final state, which are apart by a distance of r_{hop} and have energy difference of ~ few k_BT, is a coherent sum of amplitudes to tunnel along various directed paths between those states. These "directed paths" are contained between a cigar-shaped region of length rhop and width $(r_{hop}\xi)^{½}$ [197,200]. Each tunnel path consists of a sequence of localized states, transmission through which is facilitated by phonon absorption or emission. In the absence of a magnetic field, the amplitudes of each path are random, and hence they cancel each other. The presence of a magnetic field introduces phase factors to each path, which eliminates such cancellations, and hence increases the probability of the hop, leading to negative MR.[197,200]

In the above picture, numerical averaging of logarithmic conductivity over many possible paths, yields linear low-field negative MR.[200] This has been confirmed by analytical results that involve only single scattering paths.[184,201] Experimental results on nanotube networks have confirmed the same feature.[202] Alternatively, calculations using a critical percolation method instead of logarithmic averaging, yields a quadratic low-field negative MR. However, as seen from Figures 4.3(a)-(d) the logarithmic MR response (ln [R (B)/R (0)]) appears to have a Gaussian shape at all temperatures, which is in qualitative disagreement with the linear or the quadratic MR models. As shown in Figure 4.3(e), temperature dependence of the MR shows a clear non-monotonic trend, which is also not consistent with the forward interference model discussed above. The forward interference model predicts a monotonic decrease of the MR signal as temperature is increased. This is because, in this model, negative MR scales with the magnetic flux threading through the area of a coherent loop ($\sim r_{hop}^{3/2}\xi^{1/2}$) and rhop decreases with increasing temperature as indicated above[197].

Refs.[89,203] proposed an alternative interference-based mechanism that can result in negative MR in a strong localization regime. This mechanism is very similar to the weak localization mechanism in which the magnetic field breaks time-reversal symmetry between the forward and backward (hopping) paths. This results in an increased ξ with the magnetic field and hence negative MR. In quasi-one-dimensional systems (B)/ξ (0) is expected to be ~ 2.[89,203] To explore the relevance of this effect in the present case we collected I-V data at B = ± 12 kG (Figure AP 10 in Appendix). Low temperature resistance data (9–60 K range) has been fitted with the VRH model with the exponents of ⅓ and ¼ as in Figure 4.2(c). Resistance values were measured at 0.5 V bias at which the negative MR was observed (Figures 4.3, S3). From this analysis T_0 values were extracted at B = 0 kG and ± 12 kG. As mentioned earlier, for the exponent ⅓ (or, ¼), $T_0 \propto 1/g\xi^2$ (or $T_0 \propto 1/g\xi^3$). Assuming that the applied magnetic field does not change g (density of states at the Fermi level) appreciably, we estimate ξ (± 12 kG)/ξ (0 kG) ~ 1.49 (for ⅓ exponent) and 1.413 (for ¼ exponent), which is reasonably close to the theoretical value of 2. We note that further increasing the magnetic field could result in further enhancement of $\xi(B)$. Figure 4.3(f) summarizes the $1/T_0$ values under different conditions.

Negative MR can also manifest in graphitic samples due to formation of Landau levels.[185] In this mechanism, negative MR emerges when the Fermi level falls into a partially filled Landau

level. However, this mechanism is unlikely in the present situation because of the small magnetic field range employed in this study and the observation of non-monotonic temperature dependence of MR (Figure 4.3(e)), which cannot be explained using this model.

There exists one important distinction between the interference based theoretical models cited above and the DNA wrapped nanotubes considered here. In the present case, charge carriers in the nanotubes are expected to be spin-polarized due to the chiral helical potential of the DNA strands (the so-called "CISS effect").[14,138] In this effect the spin of the charge carriers is coupled to their momentum direction. This could affect the MR responses in the strong localization regime in non-trivial ways. For example, the localization model described in the previous paragraph does not predict non-monotonic negative MR with temperature. In this model, higher temperatures gradually destroy phase coherence between the forward and backward hopping paths, which results in a monotonic decay of the MR signal with temperature.

The observed non-monotonicity in the temperature dependence of MR (Figure 4.3(e)) can be explained by invoking CISS. Since the carrier spin and momentum directions are coupled, for a carrier to backscatter it will not only need to change its momentum direction but also its spin. The former can be easily accomplished by a phonon or an impurity, but the latter is not, unless the scattering event is with a magnetic impurity or a chiral phonon.[204] Thus, at low temperatures where the CISS effect is dominant, backscattering events are suppressed, resulting in reduced carrier localization and hence weak negative MR. As the temperature is slightly increased, the CISS effect weakens, and the negative MR becomes stronger. However, beyond a certain temperature, phase randomization effects take over and MR starts to decrease. Thus, the CISS effect can introduce nontrivial features in the transport phenomena in strongly localized regimes. Suppression of carrier backscattering due to CISS also explains the reduced T_0 (or increased localization length ξ) in the low temperature range mentioned earlier in the discussion of Figure 4.2(b)-(d). This is also indicated in Figure 4.3(f). We estimate ξ (low T)/ξ (high T) to be ~ 15 for d = 2 and ξ (low T)/ξ (high T) to be ~ 9 for d = 3. Thus, approximately an order of magnitude increase in the localization length takes place as a result of the CISS effect (at zero magnetic field). We note that suppression of carrier backscattering could also be a possible reason behind the observed lower value of (± 12 kG)/ξ (0 kG) compared to the spin unpolarized case as discussed before.

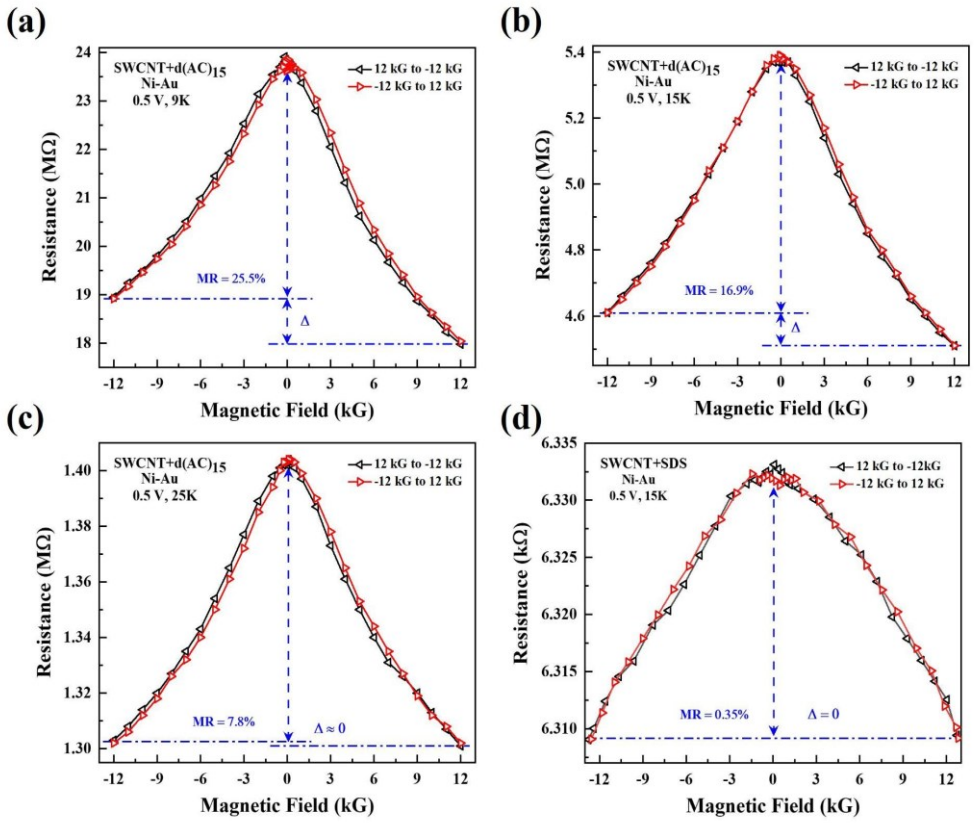

Figure 4. 4. *(a)-(c) Asymmetric MR and Δ for d(AC)$_{15}$+SWCNTs with Ni-Au contacts at different temperatures. (d) Symmetric background MR for SDS+SWCNTs with Ni-Au contacts. Applied bias is 0.5 V in all cases.*[139]

Presence of spin polarized carriers in such systems can be confirmed by replacing one of the Au contacts with Ni, which acts as a spin detector. In this configuration, unlike Figures 4.3(a)-(d), $\Delta = R\,(12\text{kG}) - R\,(-12\text{kG}) \neq 0$ (Figures 4.4 (a)-(c), Figure AP 11 in Appendix). This is because the Ni contact acts as a spin detector and it is expected to transmit the CISS-induced spins more (less) easily when its magnetization is parallel (antiparallel) to the spins. Such two-terminal detection of spins is precluded in the linear response regime, however, no such restriction is present in the non-linear regime as in the present case.[181,189] Origin of such two-terminal detection has attracted significant theoretical attention recently[99], as this method remains a simple way of detecting CISS-induced spin polarization. We note that the background negative MR is still present in Figures 4.4(a)-(c), as expected. The MR asymmetry Δ persists up to ~ 40K.

To confirm that the asymmetry Δ is not due to any artifact introduced by the Ni electrode, we prepared a set of control samples in which nanotubes are functionalized with SDS. Typical MR response from SDS coated nanotubes, measured using Ni-Au contact pairs, is shown in Figure

4.4(d). While a negative background MR is present, there is no asymmetry in MR (*i.e.*, $\Delta = 0$). This confirms that the observed Δ in Figure 4.4(a)-(c) is indeed due to helical DNA functionalization and not due to any measurement artifact. The negative MR in case of SDS functionalization is qualitatively different from the DNA functionalization, which is not surprising given their difference in carrier transport mechanisms, as discussed before.

4.3 Conclusion

Thus, in conclusion, we have explored the magnetoresistance effects in carbon nanotubes helically wrapped with DNA strands. By virtue of the CISS effect, such systems can be exploited as spin filters, without involving any magnetic element. Carrier transport in such systems is in the strong localization regime due to DNA functionalization and our results indicate that interference between forward and backward hopping paths play a critical role in carrier transport. Presence of CISS-induced spin polarization adds another layer of complexity to this problem which has not been theoretically addressed so far. It has been estimated that carrier localization length increases by an order of magnitude at the onset of CISS effect, which appears at low temperatures in these systems. Coupling of spin and momentum in this regime results in novel features that are not observed in conventional systems.

Chapter 5. Spin-dependent Phenomena in Two-dimensional (2D) Carbon Nanotube Networks[**]

5.1 Introduction

Intersections of the apparently disparate areas of organic chemistry, carbon nanotubes and spintronics have intrigued the scientific community for several decades. Organic molecular functionalization of carbon nanotubes is a common technique for various nanotechnology applications.[145,205–209] Spin transport in carbon nanotubes has been explored extensively due to its potential application in future information technology.[187,210] The area of "organic spintronics" (or "molecular spintronics") explores spin transport in organic molecular systems and has found surprisingly long spin lifetimes which could be useful for quantum information processing and other applications.[211] Recent developments in this area have unraveled an intriguing connection between organic molecular chirality and carrier spin polarization, often dubbed as "chirality-induced spin selectivity" or CISS.[212–214] The key observation is that the transmission of spin unpolarized electrons through chiral molecules can polarize the carrier spins *via* a spin filtering effect, and that the spin orientation is determined by molecular chirality (left or right-handed)[214]. CISS effect has been extensively studied using single molecule or self-assembled monolayers of DNA strands[90], oligopeptides[6], helicenes[91], polymers[92], metal-organic frameworks[93] and crystals[94], supramolecular nanofibers[95] *etc.*

While organic molecules offer virtually limitless chemical tunability, they behave as insulators in terms of their bulk (long-range) electronic properties, which inhibits their direct integration with mainstream electronics or emerging two-dimensional (2D) nanoelectronics[11,12]. This can potentially be remedied by CNT-based CISS systems, which are more conductive than their organic molecular counterparts, and could provide a useful platform for practical spintronics devices. Initial studies have reported CISS effect in one or few carbon nanotubes which are functionalized with helical single-stranded DNA[13,14,137–139,195]. Whether this effect persists in a two-dimensional nanotube network remains unknown. Ability to induce spin polarization in 2D

[**] Parts of this chapter have been submitted in – Md. Wazedur Rahman, M.C. Torres, J.M. Cuerva, Luis Á.C. and Sandipan Pramanik, 'Molecular Functionalization and Emergence of Long-range Spin-dependent Phenomena in Two-dimensional (2D) Carbon Nanotube Networks', ACS Nano 2021, 15, 12, 20056–20066.

CNT network would allow imparting spintronic functionalities to myriads of devices developed on this platform over the past few decades[205].

Despite significant experimental evidence in support of the CISS effect, a comprehensive theoretical understanding of this phenomenon remains elusive. Most theoretical models invoke molecular spin-orbit interaction to explain this effect, although according to some studies, organic molecules polarize the orbital angular momentum, rather than the spin.[8] Recent studies have indicated that CISS effect may not require a helical geometry, just the existence of chirality may be sufficient.[8,9] It has also been suggested that CISS effect could arise from the intrinsic inversion-asymmetry of the molecules and in principle, achiral inversion-asymmetric systems could also exhibit similar spin-selective phenomena.[8,10] Given that a wide range of organic molecules form efficient non-covalent binding with CNTs in water *via* hydrophobic interactions[108,145,215], it remains unknown what role, if any, they play in inducing spin polarization in carbon nanotubes.

To shed light on some of these unknowns, in this study we consider two-dimensional SWCNT networks as our conductive medium of choice. Such 2D SWCNT networks offer a high degree of electrical conductivity, which is tunable with CNT concentration, doping *etc.* These networks are easy to fabricate using commercially available SWCNTs, their transport properties are well understood[180,193,198], and they find a multitude of applications in electronics, optoelectronics and thermoelectrics.[205] As functionalization entities we choose dipeptides linked to Fmoc (N-Fluorenylmethoxycarbonyl) molecules (Figure 1(a)). Fmoc has a planar, aromatic achiral structure, which efficiently binds with CNTs[108–110] (as well as other Fmoc molecules[111–114]) in water, mainly *via* π-stacking interactions and form a three-dimensional network. Chirality can be introduced by appropriately choosing the side chains R1 and R2 (Figure 1a) in the amino acids that constitute the dipeptide. For example, Fmoc-diglycine (Fmoc-GG; R1 = R2 = H) is achiral whereas Fmoc-dialanine (Fmoc-AA; R1 = R2 = -CH3) or Fmoc-diphenylalanine (Fmoc-FF; R1 = R2 = -CH2Ph) are chiral and therefore the spin filtering effect can be studied in both enantiomers using L and D amino acids. In addition, among the various side chains, the ones with aromatic rings (such as FF) are expected to bind with CNTs more efficiently than the ones without (such as AA and GG). In this work amino acids having identical side chains and chirality were chosen (*i.e.*, R1 = R2, LL or DD) for ease of comparison between different data sets.

We note that the average diameter of the nanotubes is ~ 0.84 nm, with a nominal circumference of ~ 2.64 nm, whereas the Fmoc-dipeptide molecules are approximately ~2 nm in length[182]. Thus, the nanotube wall can accommodate both the Fmoc and its side chain. This is supported by the Raman data discussed later in the paper. The choice of Fmoc-dipeptides as functionalization entities thus allows us to investigate the spin-dependent effects in a systematic way. We also note that Fmoc is a widely used protecting group in peptide chemistry and Fmoc-dipeptides are commonly used as supramolecular hydrogels and scaffolds for complex three-dimensional nanostructures.[110,216–218]

The key findings of this work are as follows:

(a) We show for the first time that CISS effect can be induced in two-dimensional conductive SWCNT networks using appropriate chiral functionalizations. This effect is immune to nanotube disorder and does not require helical functionalization of individual nanotubes. The spin signal is "long-range" and routinely survives length scales significantly exceeding 1μm. This observation effectively bridges the gap between molecular spintronics and carbon-based two-dimensional (2D) nanoelectronics.

(b) Presence of aromatic ring in the chiral side chain is necessary to observe the CISS effect, presumably due to their more efficient binding with CNTs.

(c) Surprisingly, a non-zero spin signal has been observed in the case of a non-aromatic chiral group side chain. This effect, hitherto unreported, is independent of molecular chirality and hence cannot be ascribed to "chirality-induced" spin selective effect.

(d) Finally, angle-dependent measurements show that the CISS signal not only depends on the chirality of the molecule but also on the applied magnetic field direction. To our knowledge this has not been reported before and we show that our results are qualitatively consistent with a recently proposed theoretical model.

5.2 Synthesis of Fmoc-dipeptides + SWCNTs

Fabrication of CNT hydrogel networks functionalized with Fmoc-FF, Fmoc-AA and Fmoc-GG has been described below using a modified protocol previously described by us[110]. Briefly, a suspension of SWCNTs was prepared in an aqueous basic solution of Fmoc-dipeptide,

followed by sonication and centrifugation. Gelification in this case was triggered using Na_2CO_3 instead of using δ-gluconolactone to avoid additional chiral molecules in the media.[219–221] A slice of the gel is placed on Ni-Au electrode pairs (~ 100 nm thick, nominal electrode gap ~ 1–2 μm) fabricated on SiO_2/Si, dried at room temperature and subsequently annealed. Helium ion microscopic image of the final device structure is shown in Figure 5.1(b). Two-dimensional nanotube network, functionalized with Fmoc-dipeptides, is connected between the contacts. The SWCNTs used in this work are achiral.

(a) Reagents and materials.

N-Fluorenylmethoxycarbonyl-L-diphenylalanine (Fmoc-FF(L)), N-Fluorenylmethoxycarbonyl-L-dialanine (Fmoc-AA (L)), and N-Fluorenylmethoxycarbonyl-diglycine (Fmoc-GG) were purchased from Bachem Co., Switzerland and were used without further purification. N-Fluorenylmethoxycarbonyl-D-diphenylalanine (Fmoc-FF (D)) and N-Fluorenylmethoxycarbonyl-D-dialanine (Fmoc-AA (D)) were purchased from LifeTein, USA and were used without further purification. Sodium carbonate ≥ 99.9%, was purchased from Alfa Aesar, Germany. Sodium hydroxide (for analysis) was purchased from Merck, Germany. SWCNT was purchased from Sigma-Aldrich, USA (Product Name: Carbon nanotube, single walled 95% carbon as SWCNT, Product Number: 775533, CAS Number: 308068-56-6, https://www.sigmaaldrich.com/ES/es/product/aldrich/775533?context=product)

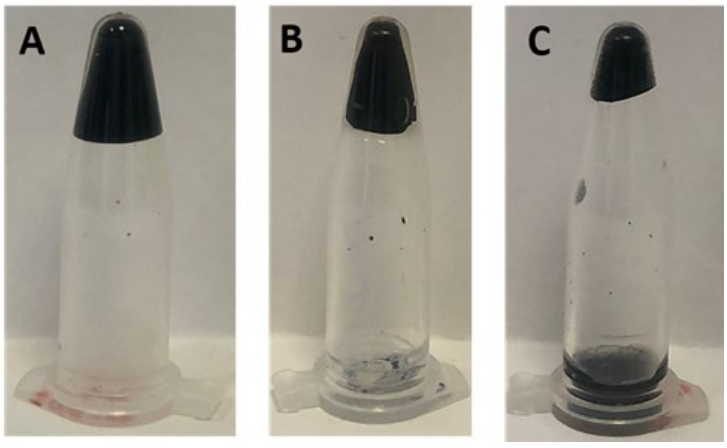

Figure 5. 1 *Image of the composite hydrogel formed in an Eppendorf in presence of sodium carbonate with different peptides:* ***(a)*** *Fmoc-FF (L) with SWCNT (0.7 mg/mL);* ***(b)*** *Fmoc-AA (L) with SWCNT (0.7 mg/mL) (after gelling a reduction in the size of the hydrogel was observed). With D amino acids the result is the same;* ***(c)*** *Fmoc-GG with SWCNT (0.7 mg/mL) (with Fmoc-GG an inconsistent gel was formed).*[140]

(b) Hydrogel Control Preparation.

Fmoc-FF (L and D), Fmoc-AA (L and D) and Fmoc-GG peptides were weighed separately into vial and deionised water was added to obtain a final concentration of 10 mM. The suspension was sonicated (in a HSt Powersonic 603-ultrasonic bath) for 1 hour. Then, a NaOH solution (0.5 M) was added dropwise until a clear solution (pH=10.5) was obtained. The pH was measured using a HACH sension PH 3 pH meter. The pH meter was calibrated using pH 4, pH 7 and pH 10 buffer solutions. Gelation was induced by adding sodium carbonate to final concentration of 25 mM and mixed by vortexing using the protocol described elsewhere.[221]

(c) Composite Hydrogel Preparation.

To prepare hydrogels with carbon nanotubes, 0.7 mg of SWCNT were weighed into a vial tube. The carbon nanotubes were suspended in 1 mL of an aqueous basic solution of: Fmoc-FF (L or D), Fmoc-AA (L or D) or Fmoc-GG 0.5% w/v (prepared above). The suspension was sonicated for 2 h in a cold ultrasonic bath and then centrifuged for 5 min at 10,000 rpm (Sigma 1-14 centrifuge). Finally, the supernatant was collected carefully.[135] Gelation was then carried out following the same method described above for the hydrogel control.

5.3 Results and Discussion

Raman characterization (Figure 5.2(c)) performed on the xerogels shows that the Fmoc-dipeptide molecules are indeed interacting with the CNTs. Intensity of the G^- peak (~ 1540 cm^{-1}), which arises due to the transverse vibration of the carbon atoms, gets suppressed as a result of functionalization. The FF molecules (both L and D) are most effective in suppressing this peak, whereas the effect is weakest for GG and AA has an intermediate effect (GG < AA < FF). This trend is summarized in Figure 5.2(d), which shows the G^-/G^+ intensity ratio for each functionalization, measured on multiple samples. Apart from the intensity ratio, locations of all the signature peaks such as RBM (radial breathing mode, ~250-300 cm^{-1}), G^- (discussed above) and G^+ (~ 1590 cm^{-1}, which arises due to the longitudinal vibrations of the carbon atoms) are shifted as a result of functionalization (Figure 5.2(c)), indicating fractional charge transfer between the molecules and nanotubes[80,110]. This data is summarized in the Supplementary Section (Figure AP 12 in Appendix).

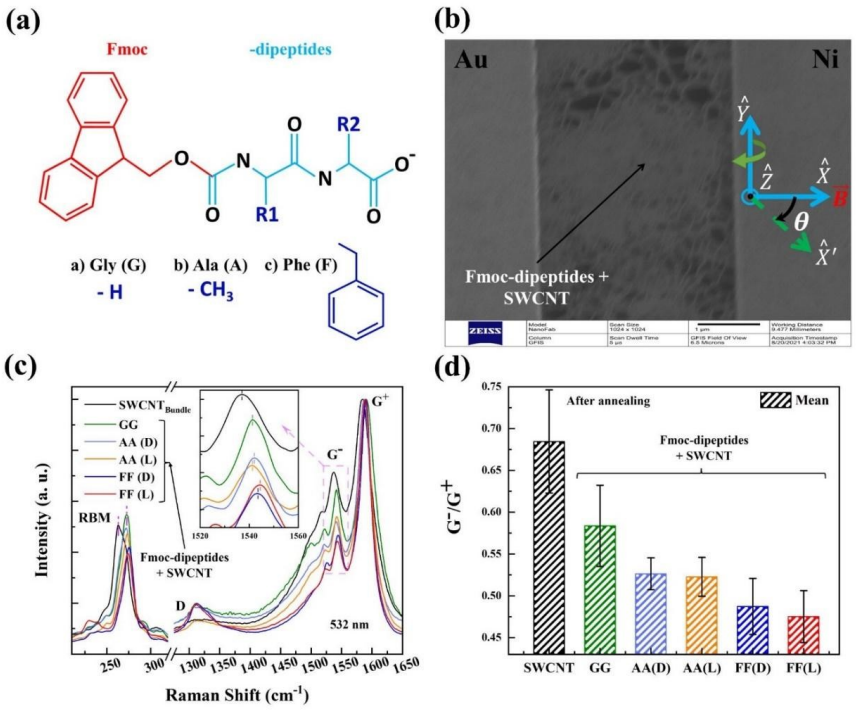

Figure 5. 2 (a) *Molecular structure of Fmoc–dipeptides and the chosen side groups (R1, R2): (a) Gly (G), (b) Ala (A), and (c) Phe (F).* ***(b)*** *Helium ion microscope (HiM) image of a typical device. Two-dimensional functionalized carbon nanotube networks are connected between Au and Ni electrodes. Channel length ~ 2μm. For angle (θ)-dependent measurements, the sample is rotated relative to the y axis as shown. Sample plane is X-Y, with the X axis coinciding with the magnetic field B for θ = 0o.* ***(c)***, ***(d)*** *Raman characterization of the functionalized nanotubes.*[140]

As expected, the observed trend of GG < AA < FF in reducing the intensity of the G^- band shows that Fmoc-FF is interacting more strongly with CNTs than Fmoc-AA and Fmoc-GG. As previously shown in ref.[108], among the hydrophobic interactions that bind together Fmoc-amino acids and CNTs, π-stacking interactions between the aromatic groups of the amino acids with the CNT show higher values of interaction energy. Additional hydrophobic interactions come from amino acid backbones, and the more hydrophobic Fmoc-AA backbone shows stronger interactions compared to that of Fmoc-GG.

Figures 5.3 (a), (c) show typical current-voltage (*I-V*) characteristics of the Fmoc-FF samples (both L and D, Ni-Au contacts) as a function of temperature (*T*). Typical semiconducting behaviour is observed at low temperatures which in some cases changes to weak metallic behaviour at high temperatures (*insets* of Figures 5.3 (a), (c)). This is a common occurrence in two-dimensional SWCNT networks and has been reported by various groups in the past[137,138,180,193,194,198]. This has been explained using a "heterogenous model" in which transport is viewed as metallic conduction in the tubes, interrupted by hopping or tunneling through small

electrical barriers that arise from molecular functionalization, tangled regions, inter-tube junctions or tube defects[193]. In the low temperature range, conduction is therefore thermally activated, whereas at higher temperatures metallic conduction manifests. Figures 5.3 (b) and (d) show fitting of temperature-dependent resistance $R(T)$ with the two dimensional variable range hopping model: $R(T) \propto exp\ (T_0/T)^{1/3}$, where T_0 is a parameter often referred to as the "characteristic temperature"[197]. A linear dependence is observed over a wide temperature range. Small deviations are observed at the low and high temperature limits, the latter due to the metallic conduction as described above. Deviations at low temperatures are consistent with the CISS phenomenon, as reported before[138].

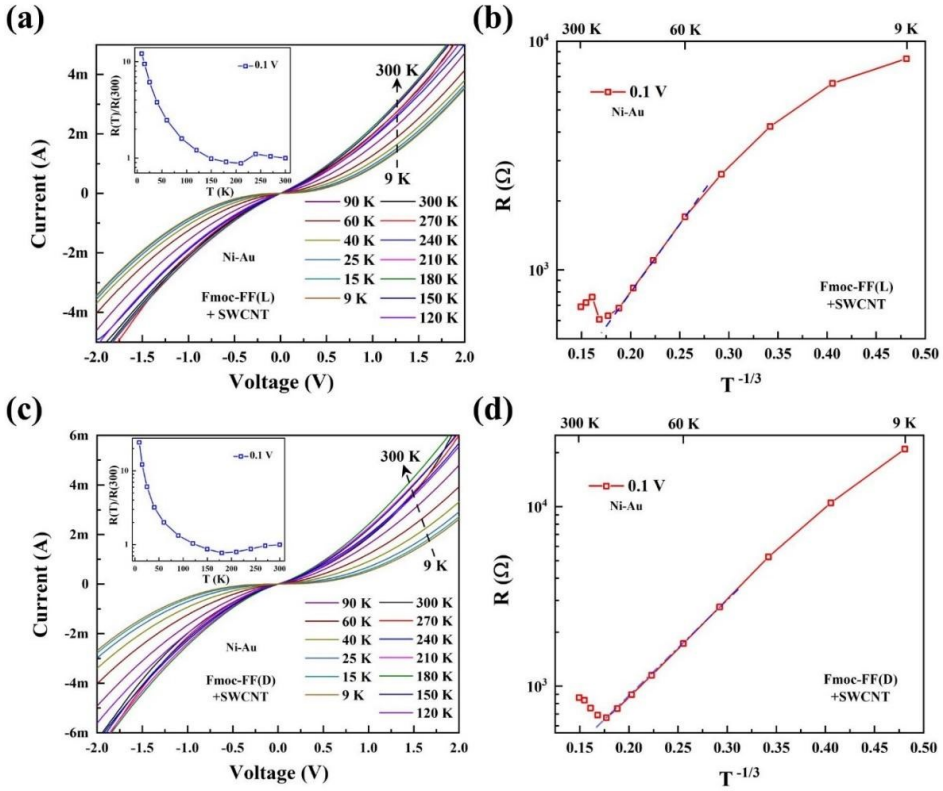

Figure 5. 3 *Current-voltage (I-V) characteristics of* ***(a)*** *Fmoc-FF (L) and* ***(c)*** *Fmoc-FF (D) functionalized SWCNTs with Ni-Au contacts.* ***(b)****,* ***(d)*** *Fitting of device resistance R (= dV/dI) with the variable range hopping model for d = 2.*[140]

Figure AP 13 in Appendix shows R(9K)/R(300K) for various functionalizations. For Fmoc-GG samples, the ratio is small (~2; also Figure AP 14 in Appendix), whereas for the Fmoc-FF samples the ratio is large (~10; also Figures 5.2 (a), (c) *insets*) and Fmoc-AA samples (Figure 5.4) fall in between. This is consistent with the GG < AA < FF trend observed from the Raman data

earlier. Due to strong interaction with the CNTs, Fmoc-FF functionalized samples appear to suppress metallic conduction in the tubes and contribute additional potential barriers, which makes the conduction strongly thermally activated.

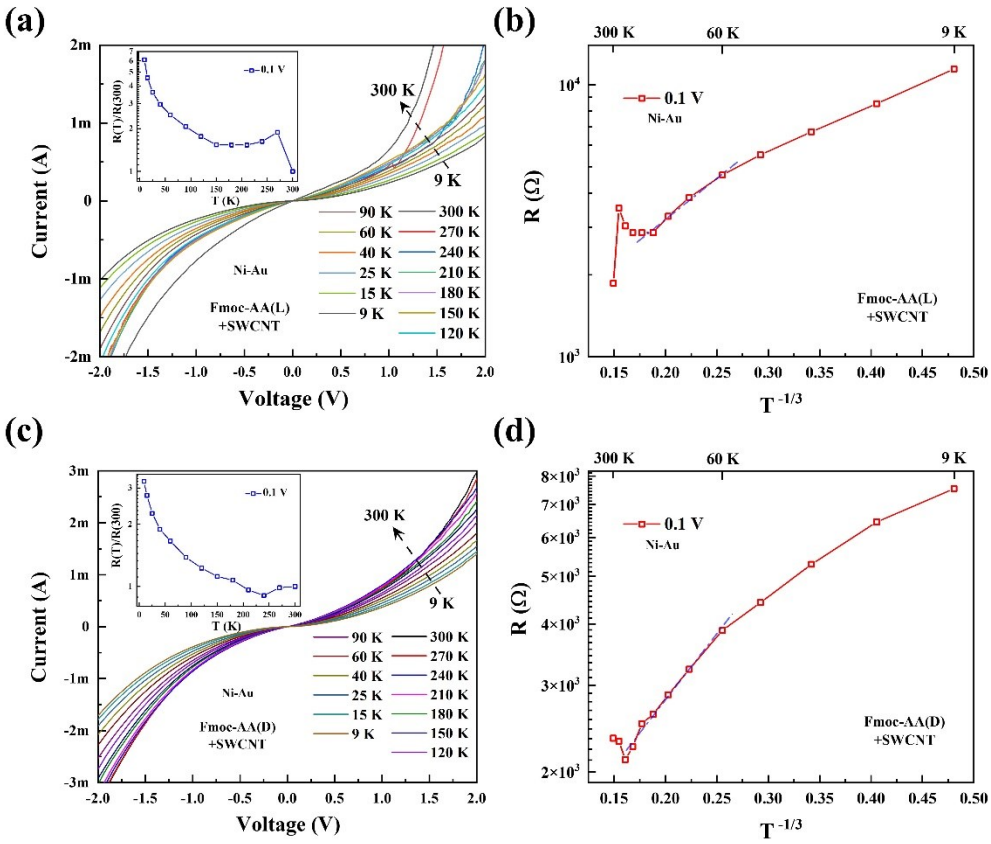

Figure 5. 4 *Current-voltage (I-V) characteristics of* ***(a)*** *Fmoc-AA (L) and* ***(c)*** *Fmoc-AA (D) functionalized SWCNTs with Ni-Au contacts.* ***(b)****,* ***(d)*** *Fitting of device resistance R (= dV/dI) with the variable range hopping model for d = 2.*[140]

Electrical detection of the CISS effect typically involves a two-terminal geometry in which the chiral layer is contacted between a magnetic (such as Ni) and a non-magnetic (such as Au) electrode.[212] Device resistances (R) are measured for two opposite magnetizations ($\pm\,\hat{m}$) of Ni and due to the CISS effect, unequal resistances are observed. Defining the CISS signal as $[R\,(-\hat{m}) - R\,(+\hat{m})]$ / min $[R\,(\pm\,\hat{m})] = \Delta$, the sign of Δ reverses as the chirality is reversed. Physically, carrier propagation in chiral systems generates chirality-dependent spin polarization, which either get transmitted or blocked depending on the direction of $\hat{m}$, giving rise to non-zero Δ. Another property of CISS systems is that for a given chirality, $I\,(+V, \pm\hat{m}) = I\,(-V, \pm\hat{m})$[212], *i.e.*, for a given $\hat{m}$, reversal of applied bias does not alter the conductance state of the device.

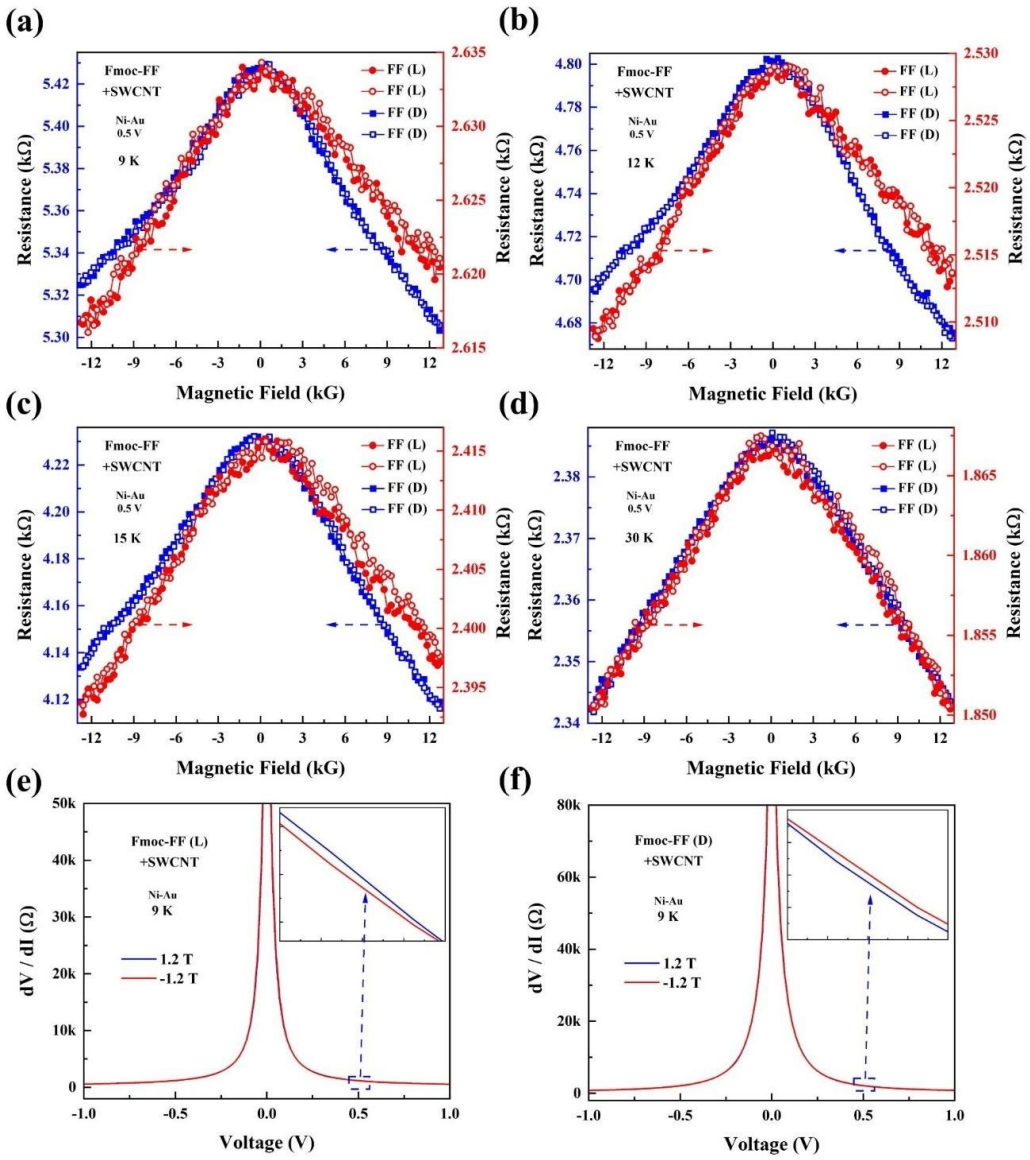

Figure 5. 5 (a)-(d) *Asymmetric MR ($\theta = 90^o$) of achiral SWCNTs functionalized with Fmoc-FF (L or D) at various temperatures. Applied bias is 0.5 V in all cases. Solid (open) symbols indicate magnetic field scan from negative (positive) to positive (negative) fields. MR asymmetry has been found to be chirality dependent.* ***(e), (f)*** *Differential resistance (dV/dI) vs bias (V).*[140]

Origin of two-terminal magnetoresistance (MR) Δ in CISS systems has been discussed extensively in recent literature.[99,181,189] Based on Onsager reciprocity argument, it has been pointed out that the above two-terminal geometry cannot result in a non-zero Δ in the *linear response* regime *i.e.*, when the *I-V* characteristics is linear, which typically happens in the low bias range.[181,189] However, no such restriction applies in the non-linear regime, where most of the experimental observations are made.[181,189,212] Recent experiments have shown non-zero two-terminal MR in both linear and non-linear regimes[222]. These results have been explained using a

model proposed in ref.[197], which suggests that in a two-terminal geometry true equilibrium is reached with local spin accumulation on the non-magnetic electrode, which depends on $\hat{m}$ as well as molecular chirality. Reversing $\hat{m}$ changes the local magnetization, which results in different conductance for $\pm\hat{m}$.

Figures 5.5(a)-(d) show two-terminal MR measurements on Fmoc-FF (L and D) samples. Direction of the magnetic field is perpendicular to the sample plane (θ = 90°), *i.e.*, Ni magnetization is out-of-plane. A background negative MR is observed, which is a common occurrence in CNT networks[138,139,180,198,223], and originates from the magnetic field dependence of hopping conductivities in these samples.[139,180,184,198,200] Most importantly, we observe a non-zero Δ (= R (-12 kG) − R (+12 kG) / min [R (±12 kG)]) for each functionalization. For the L samples Δ is negative, whereas for the D samples Δ is positive. Figures 5.5(e), (f) show bias dependence of resistance (computed by numerical differentiation of the *I-V* data), which shows the symmetric nature of device conduction for $\pm V$. This data unequivocally demonstrates that CISS effect is induced in two-dimensional CNT networks by Fmoc-FF functionalization. We note that this effect is "long-range" *i.e.*, it survives long channel length of ~ 2 μm, even in the presence of significant nanotube disorder. The experimentally accessible signal Δ is an "ensemble average", and surprisingly the MR signal is still approximately in the same range of those obtained from ordered chiral molecules under comparable conditions.[212] In addition, due to the planar geometry, these devices do not suffer from the reliability issues encountered in the vertically stacked geometry.[224]

Figures 5.6(a), (b) show the temperature dependences of background MR (defined as (R (0) – min [R (±12 kG)])/ min [R (±12 kG)]) and Δ respectively, as observed in Figure 5.5. The MR responses of both L and D follow a similar non-monotonic trend and gradually decrease with temperature. MR nonmonotonicity in CNT based chiral systems has been reported before[14,15,137,138], which arises due to an interplay between the quantum interference effect between the forward and reverse hopping paths and simultaneous suppression of carrier backscattering due to the CISS effect at low temperatures. The magnitude of the MR asymmetry signal Δ decays monotonically with temperature. This is presumably due to enhanced spin scattering at higher temperatures in CNTs, which has been reported before.[210] An interesting observation from Figure 5.6(b) is that the CISS signal Δ from the D molecules is stronger than that of L. Origin of this will be discussed later in the paper.

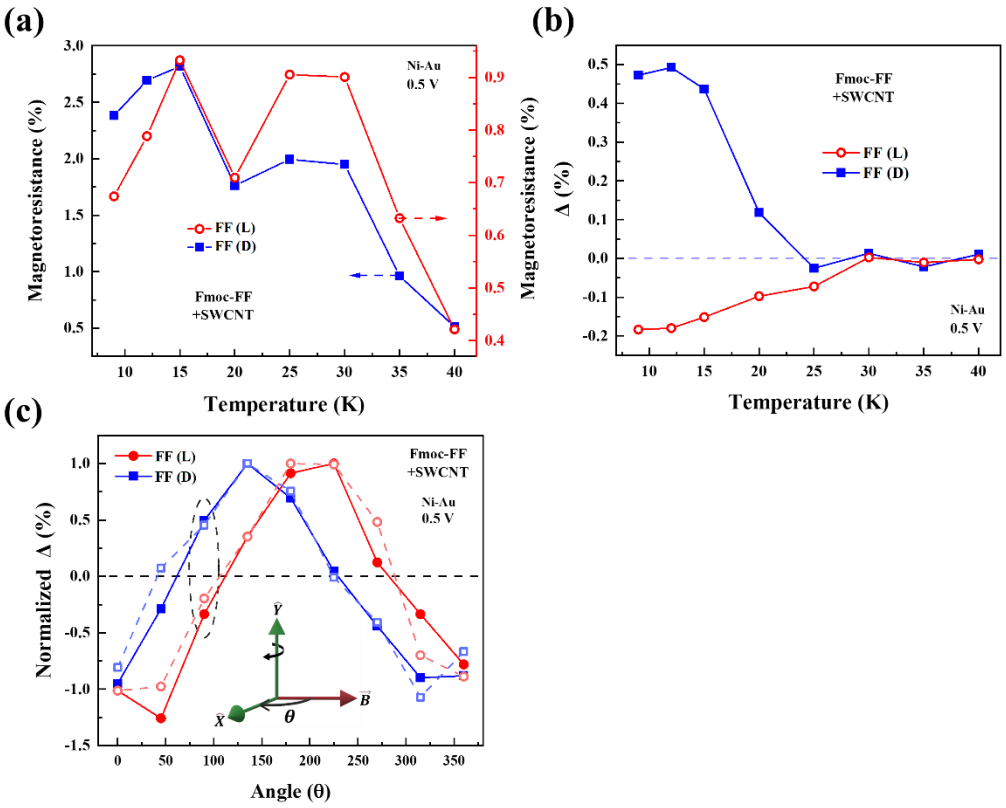

Figure 5. 6 (a) *Temperature dependence of background MR (at $\theta = 90^o$) for Fmoc-FF (L or D) functionalized SWCNTs.* ***(b)*** *MR asymmetry Δ (%) as a function of temperature (at $\theta = 90^o$).* ***(c)*** *Normalized Δ (%) at different orientations of Ni magnetization. Sample is in the X-Y plane. For each sample, normalization is done relative to the corresponding maximum value of Δ. Responses from two different samples are shown for each functionalization. Applied bias is 0.5 V in all cases.*[140]

Figure 5.6(c) shows angle (θ) dependence of *normalized* Δ as observed from multiple samples (both L and D). In each case normalization has been done relative to the corresponding maximum value of Δ (say Δ_{max}) for ease of comparison. The MR responses shown earlier in Figure 5.5 are for $\theta = 90^o$, which corresponds to out-of-plane magnetic field (and hence out-of-plane Ni magnetization $\hat{m}$); similarly, $\theta = 0^o$ corresponds to in-plane magnetic field and in-plane $\hat{m}$). Interestingly, we notice that for some angle ranges Δ has the *same* sign for both chiralities. Thus, the chirality-dependent response exists only in a few narrow ranges of θ (in the vicinity of 90^o and 270^o). Overall, Δ has a periodicity of ~360^o. This is consistent with the general CISS behaviour in which Ni magnetization and chirality jointly select one direction along which current flow is favoured.

Dependence of Δ on both $\hat{m}$ and chirality is consistent with recent theoretical models. According to the model proposed in ref.[99] the nonmagnetic contact (Au) is locally magnetized

under equilibrium. This occurs as a result of transient spin transfer from the magnetic lead (Ni) through the chiral medium to Au, which ensures zero current under equilibrium. The induced local magnetization of the Au contact (say $\widehat{m'}$) depends on $\hat{m}$ as well as molecular chirality. The induced magnetization $\widehat{m'}$ can be decomposed into two components that are perpendicular and parallel to Ni magnetization $\hat{m}$**.** The perpendicular component changes sign as $\hat{m}$ is reversed, but the parallel component remains unchanged. Thus, as $\hat{m}$ is changed $\widehat{m'}$changes as well in a non-trivial way. Under small, applied bias this setup generates non-zero Δ, which will clearly be dependent on $\hat{m}$ as well as molecular chirality.

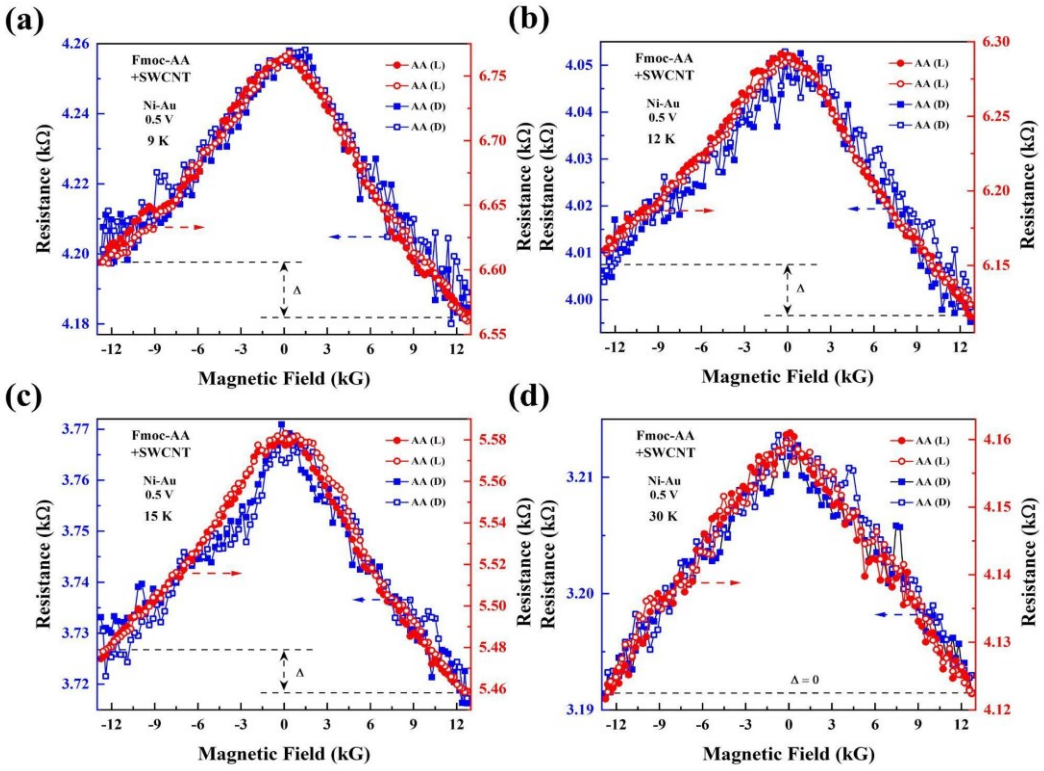

Figure 5. *7 (a)-(d) Asymmetric MR of Fmoc-AA (L or D) functionalized SWCNTs using Ni-Au contacts at various temperatures (θ = 90°). Applied bias is 0.5 V in all cases. Solid (open) symbols indicate magnetic field scan from negative (positive) to positive (negative) fields. MR asymmetry is independent of molecular chirality.*[140]

To explore the existence of the CISS effect for other types of chiral molecular functionalization, we chose Fmoc-AA. Although Fmoc-AA is chiral, unlike Fmoc-FF its side chain is non-aromatic and hence it is expected to have weaker interaction with the CNTs. The Raman and transport data presented earlier confirms that this is indeed the case. Figure 5.7 shows MR responses of Fmoc-AA functionalized CNTs for θ = 90°. Background negative MR is present as before. Asymmetric MR (*i.e.*, non-zero Δ) is present as well, which indicates spin-dependent

transmission through the Ni spin detector. However, unlike Fmoc-FF the sign of Δ is *independent* of molecular chirality, and it is *positive* for both L and D samples. Chirality independence of Δ can be rationalized by invoking weak interaction of the chiral side chain with CNTs as discussed above. However, it remains unclear why the MR asymmetry Δ manifested in the first place, since the chiral interaction is weak.

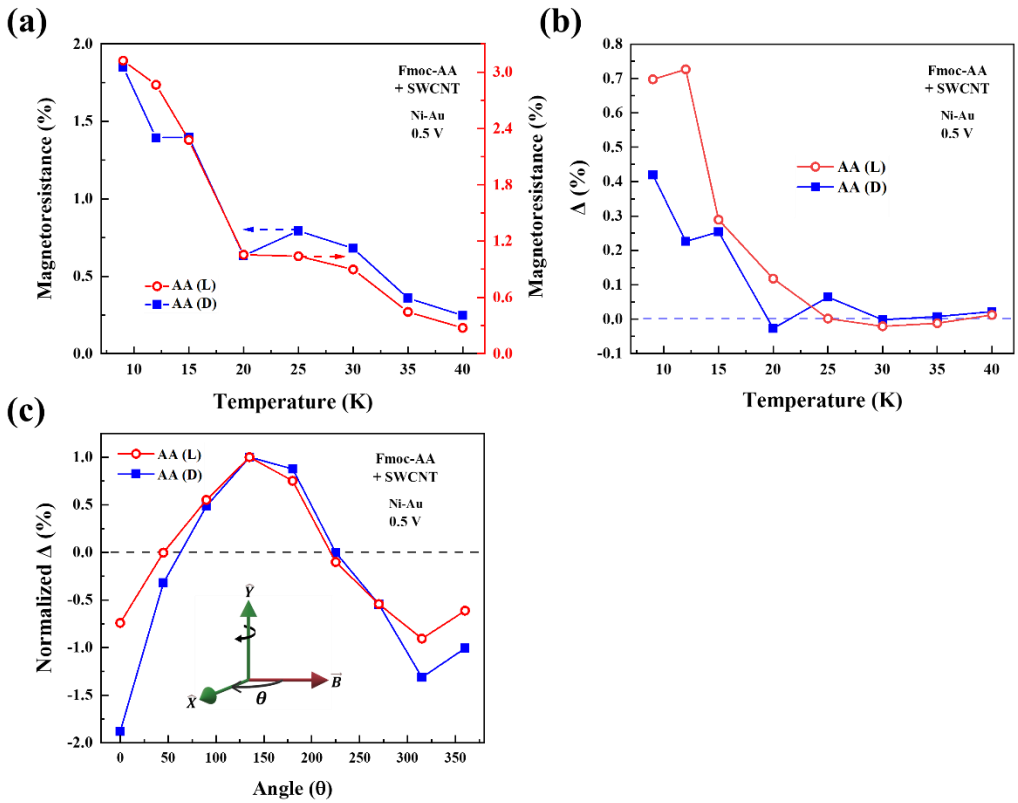

Figure 5. 8 (a) *Temperature dependence of background MR (θ = 90°) for Fmoc-AA (L or D) functionalized SWCNTs.* ***(b)*** *Δ (%) as a function of temperature.* ***(c)*** *Normalized Δ (%) at different magnetization orientations of Ni. Sample is in the X-Y plane. For each type of sample, normalization is done relative to the corresponding maximum value of Δ. Applied bias is 0.5 V in all cases.*[140]

Figure 5.8 summarizes the salient features of the MR responses observed in Figure 5.7 such as (*i*) non-monotonic temperature dependence of the background MR (Figure 5.8 (a)) and (*ii*) gradual decay of Δ with temperature. Unlike Fmoc-FF, in the case of Fmoc-AA Δ has the same sign (positive) for both L and D functionalizations. Figure 5.8(c) shows Δ as a function of Ni magnetization orientation θ. Unlike Fmoc-FF, the sign of Δ is virtually the same for L and D molecules at all measurement angles θ, which precludes detection of any "chirality-dependent" behaviour at any angle.

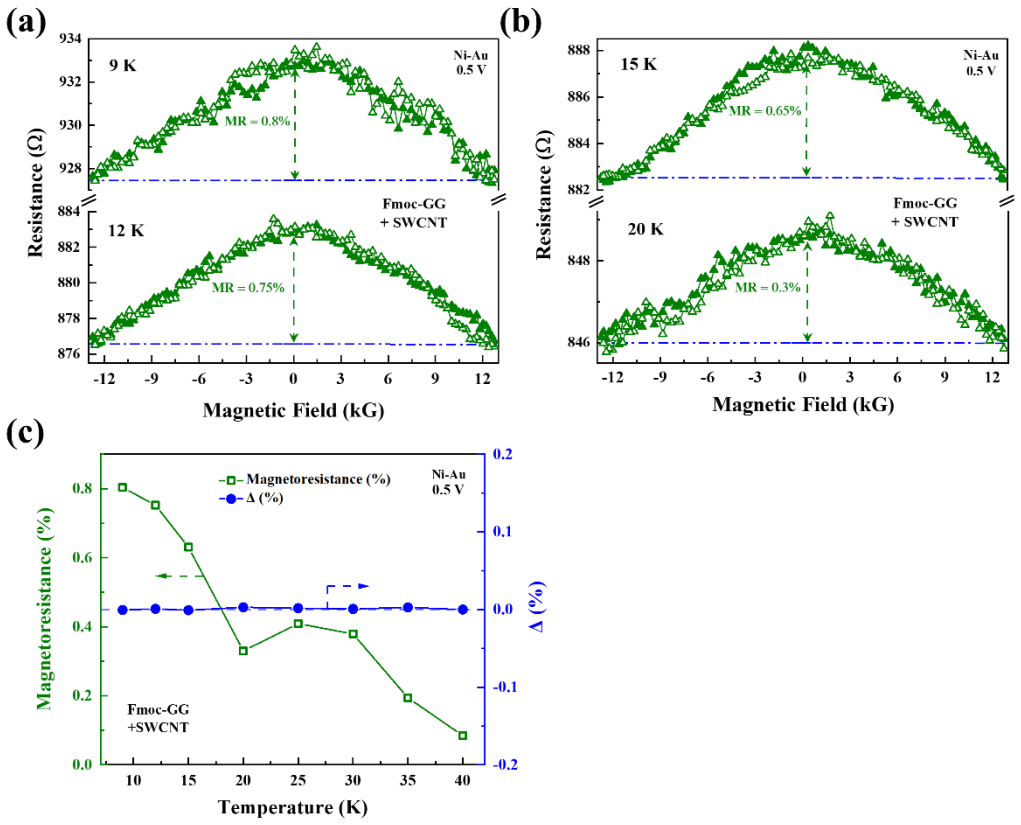

Figure 5. 9 (a), (b) *Symmetric MR of Fmoc-GG functionalized SWCNTs using Ni-Au contacts at various temperatures (θ = 90°).* ***(c)*** *Temperature dependence of background MR. MR asymmetry signal Δ is zero (below the noise margin of the measurements) for Fmoc-GG functionalization.*[140]

Since side chain interaction with CNTs appears to have an influence on Δ, next we chose Fmoc-GG as the functionalization agent. Fmoc-GG is achiral and has the weakest interaction with SWCNTs compared to Fmoc-AA and Fmoc-FF as discussed earlier. Figure 5.9 shows the MR responses of Fmoc-GG functionalized SWCNTs. The background negative MR is present, but MR asymmetry Δ could barely be detected above the noise level (for θ = 90° and other angles). Combined with the Fmoc-FF and Fmoc-AA data presented above, this shows that the side chain interaction with SWCNT plays a central role in determining Δ, which is related to the spin polarization of the carriers.

There are two primary sources of interaction between Fmoc-dipeptides and CNTs: (a) interaction of the aromatic rings belonging to the Fmoc group with CNTs and (b) interaction of the dipeptide side chains with CNTs. The former is common for all the molecules discussed above, and the latter is variable with a trend GG < AA < FF as discussed before. In case of Fmoc-GG,

side chain interaction is negligible, and hence absence of Δ in this case indicates that the interaction of the Fmoc group aromatic rings with CNT does not result in any spin-polarization of the charge carriers.

The MR asymmetry Δ (implying carrier spin polarization) in case of Fmoc-AA must therefore be attributed to the peptide side chain interaction with the CNTs. However, this induced spin polarization is not dependent on molecular chirality, as demonstrated in Figures 5.7 and 5.8, and hence doesn't fall under the category of "chirality-induced" spin selectivity (CISS). As discussed earlier, this could be related to the *inherent inversion asymmetry* of the chiral molecules considered.[8,10] Chirality independence of Δ could be attributed to the weak interaction of the chiral side chain with CNTs.

If the above hypothesis is correct then this inversion-asymmetry related Δ should also be present in case of Fmoc-FF, although in this case strong side chain interaction dominates the MR response and gives rise to CISS effect. This underlying inversion asymmetry effect could explain why the Δ signals have different magnitudes for Fmoc-FF (L) and Fmoc-FF(D) as shown in Figure 5.6(b). As seen from Figure 5.7, this inversion asymmetry effect results in positive Δ, which will oppose the CISS signal for Fmoc-FF (L) and aid the CISS signal for Fmoc-FF (D). Therefore, the D signal (positive Δ) in Figure 5.6(b) is stronger than the L signal (negative Δ), because it is a combined effect of the molecular chirality as well as inherent inversion asymmetry.

5.3 Conclusion

To summarize, in this study we have tested the role of molecular functionalization on inducing spin polarization in two-dimensional carbon nanotube networks. Achiral, aromatic interactions (such as the Fmoc group with CNT in the case of Fmoc-GG) did not result in any detectable spin signal. "Weak" chirality was then introduced in the system by replacing the side group with a non-aromatic but chiral entity (the case of Fmoc-AA, which interacts weakly with CNT). This resulted in a *chirality-independent* spin signal, presumably due to the inversion asymmetry of the system. Next, "strong" chirality was introduced by replacing the side chain with an aromatic chiral entity (the case of Fmoc-FF, which interacts strongly with CNT). This resulted in a spin signal which is a combination of the chirality dependent part as well as the inversion asymmetric part. Effect of inversion asymmetry on spin signals is a virtually unexplored area,

especially compared to their CISS counterpart. Further studies in this area are needed to generate a coherent understanding of these phenomena.

Looking at the bigger picture, this study indicates that long-range (~ 1–2 μm) spin dependent effects can be induced in a wide variety of two-dimensional carbon-based materials functionalized with appropriate chiral entities. We offer preliminary "rules of thumb" regarding what molecular structural features could be most appropriate for this purpose. Since the CISS effect is enhanced with the spatial extent of the chiral scattering path, the proposed scheme can result in even longer-range (presumably tens of microns or more) spin information transmission. Some of these studies are currently in progress.

Chapter 6. Exploration of CISS Effect in 2D CNT Networks in the Presence of Multiple Chiral Sources

6.1 Introduction

In our previous chapter, we explored spin polarization in 2D CNT network by functionalizing carbon nanotubes with one type of chiral molecules - Fmoc-dipeptides. These dipeptides show "chirality dependent spin selectivity (CISS)" only when an aromatic ring is present on the chiral side chain, presumably because aromatic rings bind more efficiently with CNTs *via* π-π interaction. In particular, Fmoc-FF was used to demonstrate this effect. Chiral sidechain of Fmoc-FF (L) chain has two chiral centers with an absolute configuration of (S, S) and Fmoc-FF (D) has two chiral centers with an absolute configuration of (R, R), as shown in Figures 1.5 and 6.1 (a).[115] These two molecules are enantiomers, meaning they are non-superimposable mirror images of each other, *i.e.*, if Fmoc-FF (L) is levorotatory then Fmoc-FF (D) is dextrorotatory. These chiral sidechains interact strongly with the CNTs, which manifests in the Raman and transport characterization studies as discussed earlier. As carriers travel through the CNT networks, they undergo spin dependent scattering from these chiral sidechains which are bound with CNTs *via* π-stacking and results in chirality dependent spin signal. As reported in our earlier work, such signals decrease gradually with temperature and also depend on the magnetic field angle relative to the 2D plane. In particular, chirality dependent effect was observed when the magnetic field was perpendicular to the 2D plane.

In order to explore tunability of the observed spin signals by engineering the chiral scattering centers, we introduce mixed chirality in the medium by incorporating another molecule glucono-δ-lactone (GdL) in the synthesis process. GdL plays a crucial role in carbohydrate metabolism and is found in many biological systems.[118] Addition of GdL in the synthesis process results in a CNT peptides hydrogel.[124,125,135] In this work we compare and contrast transport data for samples with and without this additional chiral source (GdL). For the samples without GdL, synthesis was performed using sodium carbonate, which are achiral.

There are six carbon (C) atoms (Figure 6.1 (a)) in the GdL ring, and every C atom is attached to a group of oxygen (OH).[121] Each carbon that bear both hydrogen and hydroxyl, will be a chiral center. GdL has four chiral centers - 3R,4S,5S,6R - where the number defines the position

of the chiral carbon.[122] The chirality of GdL will add additional chiral center along with the Fmoc-dipeptides in the system.

In principle, during the synthesis process, GdL should not bind with CNTs, and hence it is not expected to directly influence CISS effect in the CNT network. However, as we report below, its presence in the chiral medium (trapped between the peptides and the CNTs when the gel dries), does have an impact on the CISS effect. Introduction of such additional chiral centers could offer a way to tune the CISS effect in 2D CNT networks.

6.2 Results and Discussion

Fabrication of CNT hydrogel networks functionalized with GdL and Fmoc-dipeptides has been described previously.[135] Briefly, a suspension of SWCNTs was prepared in an aqueous basic solution of Fmoc-dipeptide, followed by sonication and centrifugation. Gelification in this case was triggered using GdL.[219–221] A slice of the gel is placed on Ni-Au electrode pairs (~ 100 nm thick, nominal electrode gap ~ 1–2 μm) fabricated on SiO_2/Si, dried at room temperature and subsequently annealed. FESEM image of the final device structure is shown in Figure 6.1 (b). Two-dimensional nanotube network, functionalized with Fmoc-dipeptides, is connected between the contacts. Both chiral and achiral SWCNTs (6, 5) were tested in this work. No significant effect of CNT chirality on CISS was observed. Control samples sans GdL were prepared either sodium carbonate or caprolactone. The synthesis process were performed by our collaborators at Universidad de Granada, 18071 Granada, Spain. Fabrication of the device as well as spin transport experiments were performed by us.

The xerogel's Raman analysis (Figure 6.1 (c-e), with and without GdL) demonstrates that GdL molecules do not significantly alter interaction of CNTs with Fmoc-dipeptides. Figure 6.1 (c) shows Raman characterization of SWCNTs functionalized with Fmoc-dipeptides and GdL. The intensity of the G- peak (1540 cm^{-1}, which is caused by the transverse vibration of the carbon atoms) is suppressed as a result of functionalization, as shown in Figure 6.1 (c). The FF molecules are the most effective at suppressing this peak, whereas GG has the least effect and AA falls somewhere in between (GG < AA < FF). Figure 6.1 (d) summarizes G-/G+ intensity ratio for each functionalization as assessed on numerous samples (~15) to highlight this pattern. The G-/G+ intensity ratio with and without GdL are compared in Figure 6.1 (e). No significant difference was observed, which is consistent with the fact that GdL does not directly bind with CNTs, rather they

are trapped in the chiral medium between the CNTs and the peptides. The G+ peak (1590 cm^{-1}) in Figure 6.1 (c) represents the longitudinal vibrations of carbon atoms, which gets narrowed as a result of functionalization (Figure 6.2 (a)). Aside from affecting the G-/G+ intensity ratio, functionalization causes all characteristic peaks to upshift as seen from Figure 6.1 (c) and Figure 6.2 (b-d). This indicates fractional charge transfer between molecules and nanotubes.

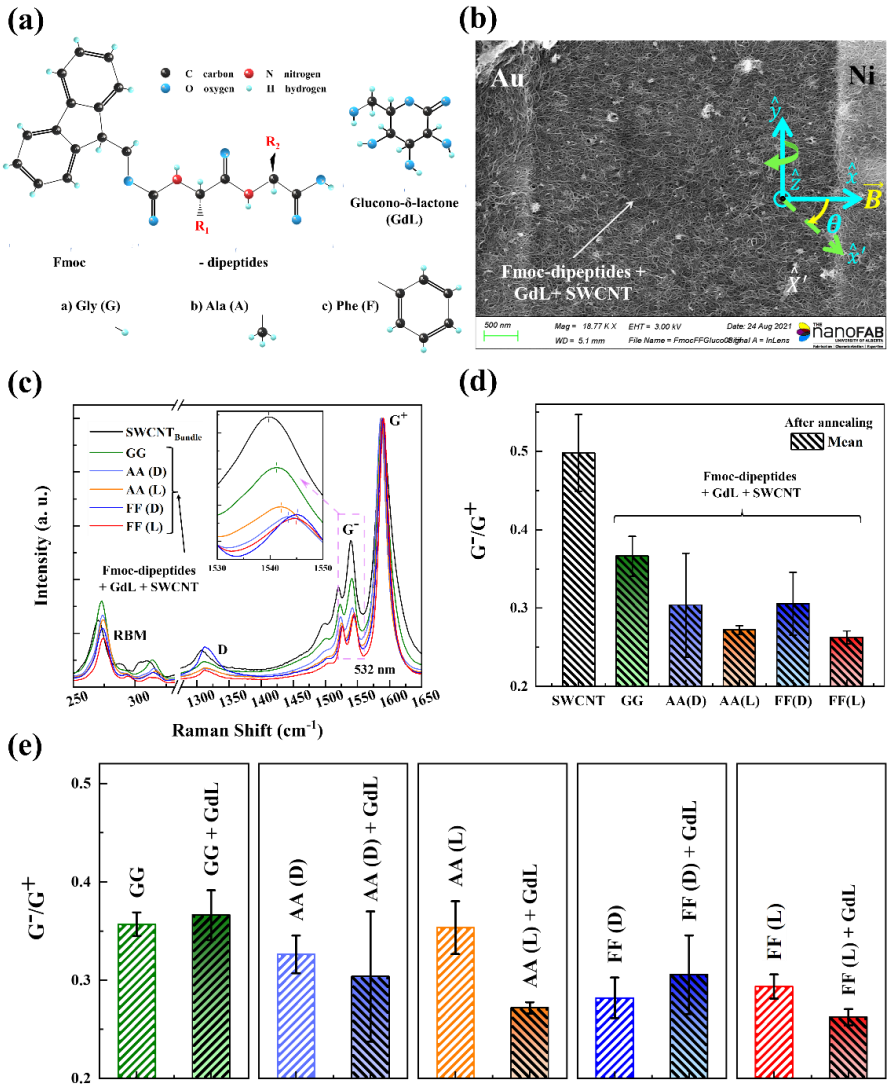

Figure 6. 1. (a) *Molecular structure of Fmoc–dipeptides + GdL and the chosen side groups (R_1, R_2): (a) Gly (G), (b) Ala (A), and (c) Phe (F).* ***(b)*** *FESEM image of a typical device. Two-dimensional functionalized carbon nanotube networks are connected between Au and Ni electrodes. Channel length ~ 2μm. For angle (θ)-dependent measurements, the sample is rotated relative to the y axis as shown. The sample plane is X-Y, with the X-axis coinciding with the magnetic field B for θ = 0º,* ***(c)-(e)*** *Raman characterization of the functionalized nanotubes.*

The observed tendency of GG < AA < FF in suppressing the intensity of the G− band indicates that Fmoc-FF binds more strongly with CNTs than Fmoc-AA and Fmoc-GG. As observed previously[108], π-stacking interactions between the aromatic groups of the amino acids and CNT have greater interaction energies. Additional hydrophobic interactions are provided by amino acid backbones, with the more hydrophobic Fmoc-AA backbone exhibiting stronger interactions than the Fmoc-GG backbone.

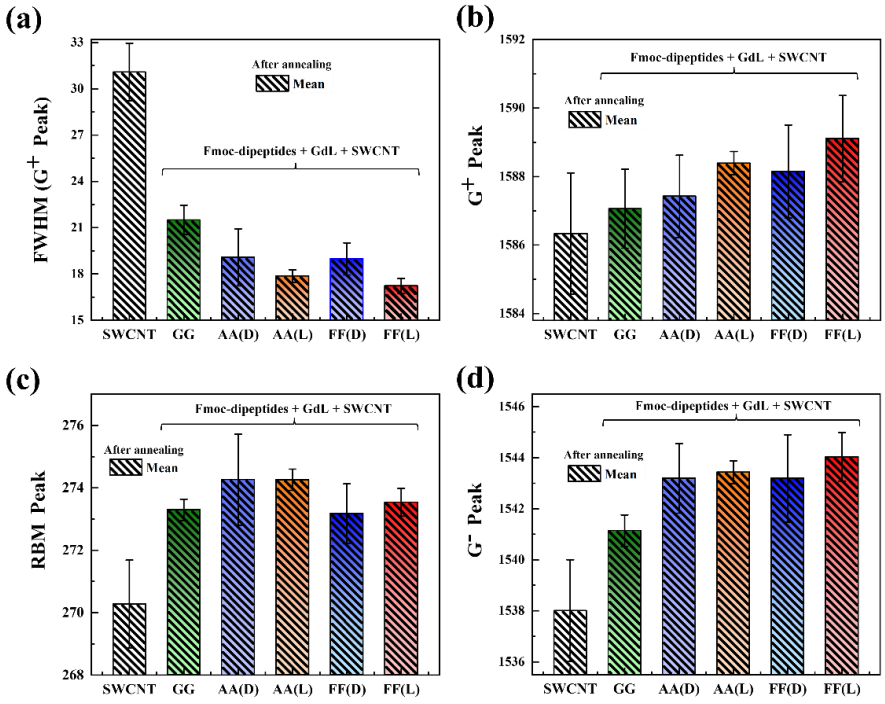

Figure 6. 2. (a) *Full-width half maximum (FWHM) of G+ peak,* ***(b)-(d)*** *G+ peak, RBM peak, and G- peak positions as a function of molecular functionalization.*

The current-voltage I-V characteristics of Fmoc-GG + GdL samples are shown in the Figures 6.3 (a). Typical semiconducting behaviour is observed as a function of temperature (T) and temperature dependence is comparatively higher at low temperatures. Fmoc-GG + GdL samples, unlike Fmoc-GG, do not exhibit weak metallic behaviour at high temperatures (*insets* of Figures 6.3 (c)). Figures 6.3 (b) illustrate the temperature-dependent resistance R(T) fitting with the two-dimensional variable range hopping model discussed in earlier chapters. Over a large temperature range, a linear relationship is seen.

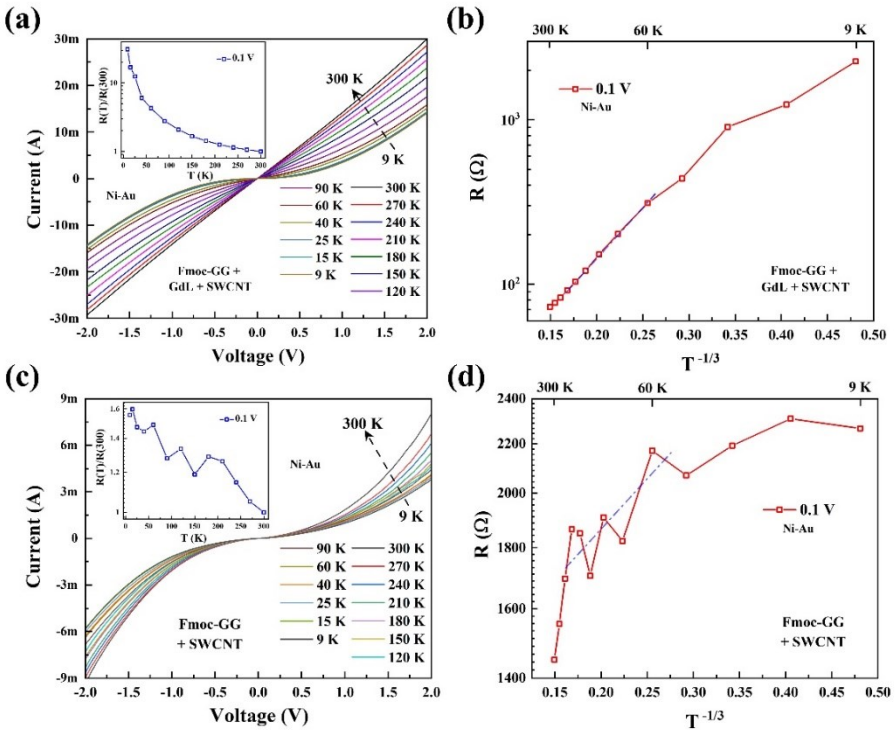

Figure 6. 3. (a) *Current-voltage (I-V) characteristics of Fmoc-GG + GdL + SWCNTs with Ni-Au contacts,* ***(b)*** *Fitting of device resistance R (= dV/dI) with the variable range hopping model for d = 2,* ***(c)*** *Current-voltage (I-V) characteristics of Fmoc-GG + SWCNTs with Ni-Au contacts, and Fitting of device resistance R (= dV/dI) with the variable range hopping model for d = 2.*

Achiral dipeptides, Fmoc-GG, which has the lowest interaction with SWCNTs, demonstrated negative MR responses. The magnetic field dependent hopping conductivity causes the background negative MR, as discussed in earlier works.[138,139] Figures 6.4 (a)-(b) demonstrate MR asymmetry (*i.e.*, non-zero Δ (Δ = *R* (-12 kG) - *R* (+12 kG) / min [*R* (±12 kG)])) for Fmoc-GG + GdL, whereas Figure 6.4 (c) shows symmetric MR for Fmoc-GG. The MR asymmetry observed in Figure 6.4 (a)-(b) can therefore be attributed to the presence of GdL in the chiral medium. This observation is somewhat surprising since GdL does not interact strongly with CNTs as observed from Raman data. Figure 6.4 (d) shows the MR responses and Δ with temperature for the Fmoc-GG + GdL functionalized samples. The normalized Δ (at 9K) with a 360-degree periodicity is shown in Figure 6.4 (e). On the other hand, MR responses for Fmoc-GG functionalized sample do not display a prominent second peak, and delta is zero for all temperature ranges. The MR response of Fmoc-GG + GdL functionalized CNTs lasted ~10K longer when the temperature was raised than that of just Fmoc-GG functionalized CNTs (Figure 6.4 (d), (f)). Therefore, the existence of GdL in the medium appears to make the MR responses more temperature responsive.

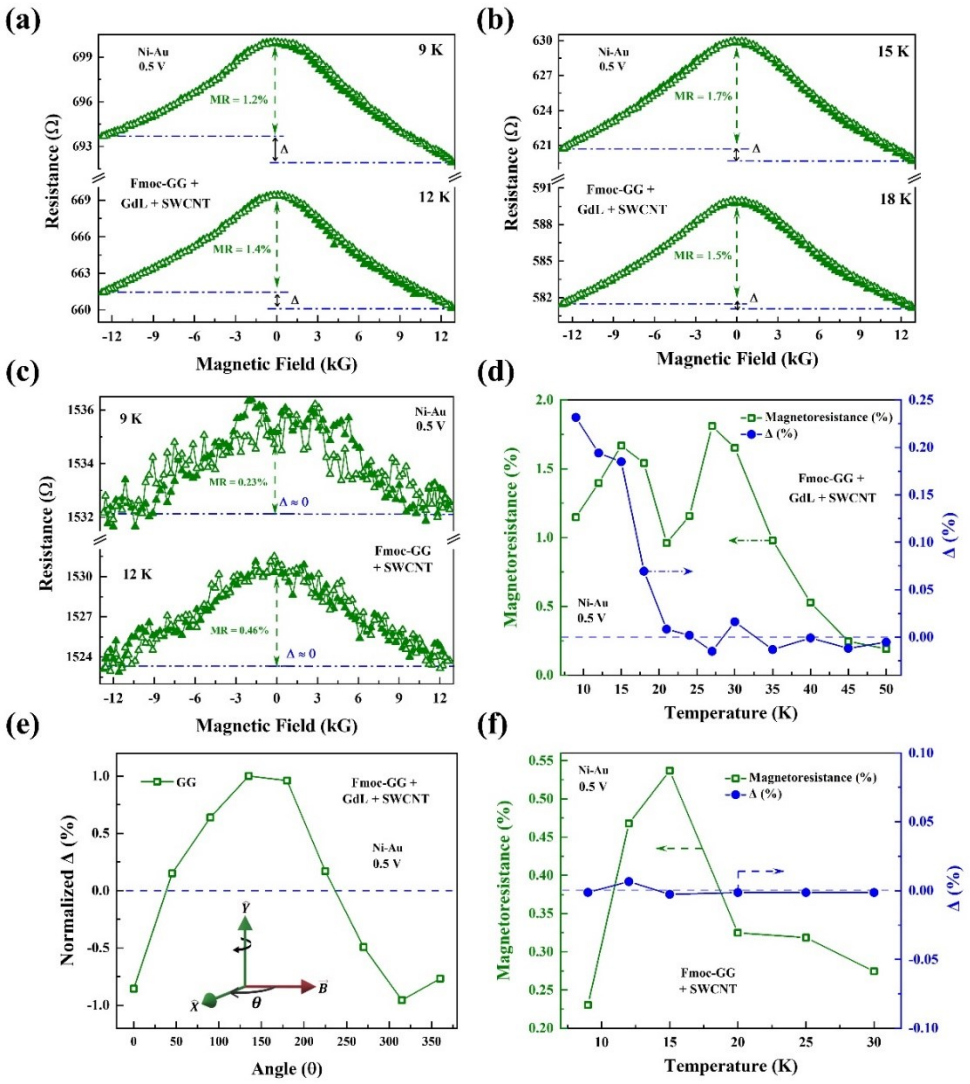

***Figure 6. 4. (a)**, **(b)** Asymmetric MR of Fmoc-GG + GdL functionalized SWCNTs using Ni-Au contacts at various temperatures ($\theta = 90^o$) **(c)** Temperature dependence of background MR ($\theta = 90^o$) and Δ (%) as a function of temperature for Fmoc-GG + GdL functionalized SWCNTs. **(d)** Normalized Δ (%) at different magnetization orientations of Ni. The sample is in the X-Y plane. For each type of sample, normalization is done relative to the corresponding maximum value of Δ. Applied bias is 0.5 V in all cases. **(e)** Temperature dependence of background MR ($\theta = 90o$) and Δ (%) as a function of temperature for Fmoc-GG + GdL functionalized SWCNTs, **(f)** Symmetric MR of Fmoc-GG functionalized SWCNTs using Ni-Au contacts at various temperatures ($\theta = 90^o$).*

Next, we conducted our experiments with Fmoc-AA + GdL. Fmoc-AA is chiral, its side chain is non-aromatic and is known to have a poorer interaction with the CNTs than Fmoc-FF and slightly higher than Fmoc-GG. This is supported by the Raman presented previously and transport data on Figure 6.5 (a)-(d). The current-voltage I-V characteristics of the Fmoc-AA + GdL samples are shown in Figures 6.5 (a), (c). Typical semiconducting behaviour is observed as a function of temperature (T) and temperature dependence is comparatively higher at low temperatures.

Similarly, Fmoc-AA + GdL samples do not exhibit weak metallic behaviour at high temperatures (*insets* of Figures 6.5 (a), (b)). Figures 6.5 (b), (d) illustrate the temperature-dependent resistance R(T) fitting (mostly linear).

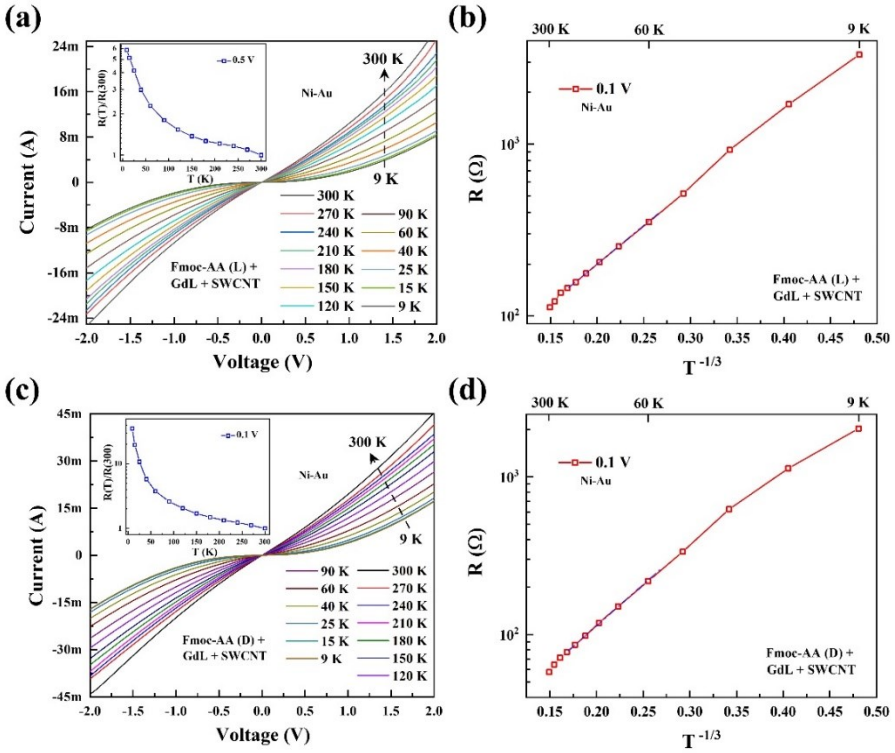

Figure 6. 5. *Current-voltage (I-V) characteristics of* ***(a)*** *Fmoc-AA (L)+ GdL and (c) Fmoc-AA (D)+ GdL functionalized SWCNTs with Ni-Au contacts.* ***(b)****,* ***(d)*** *Fitting of device resistance R (= dV/dI) with the variable range hopping model for d = 2.*

The MR responses of Fmoc-AA + GdL functionalized (Figure 6.6 (a), (c), (e)) CNTs and only Fmoc-AA functionalized (Figure 6.6 (b), (d), (f)) CNTs at $\theta = 90^{o}$ shows similar negative MR in the background. Asymmetric MR is also present, indicating spin-dependent transmission *via* the Ni spin detector. However, because the chiral interaction is weak, it is unknown why the MR asymmetry manifests in the first place for both Fmoc-AA + GdL and Fmoc-GG + GdL. For the instance of Fmoc-AA + GdL functionalized CNTs also, MR response lasted for ~10K higher temperature compared to only Fmoc-AA functionalized CNTs as temperature increased (Figure 6.7 (a), (b)). The asymmetry (Δ) follows a similar pattern of extended range as the temperature rises, although it is comparatively small. Observation of MR asymmetry in these cases most likely originate from the intrinsic "inversion asymmetry" experienced by the carriers as they traverse the

CNTs in the present of multiple scattering centers. It appears that the presence of multiple chiral centers in the medium tends to make the MR asymmetry more immune to temperature.

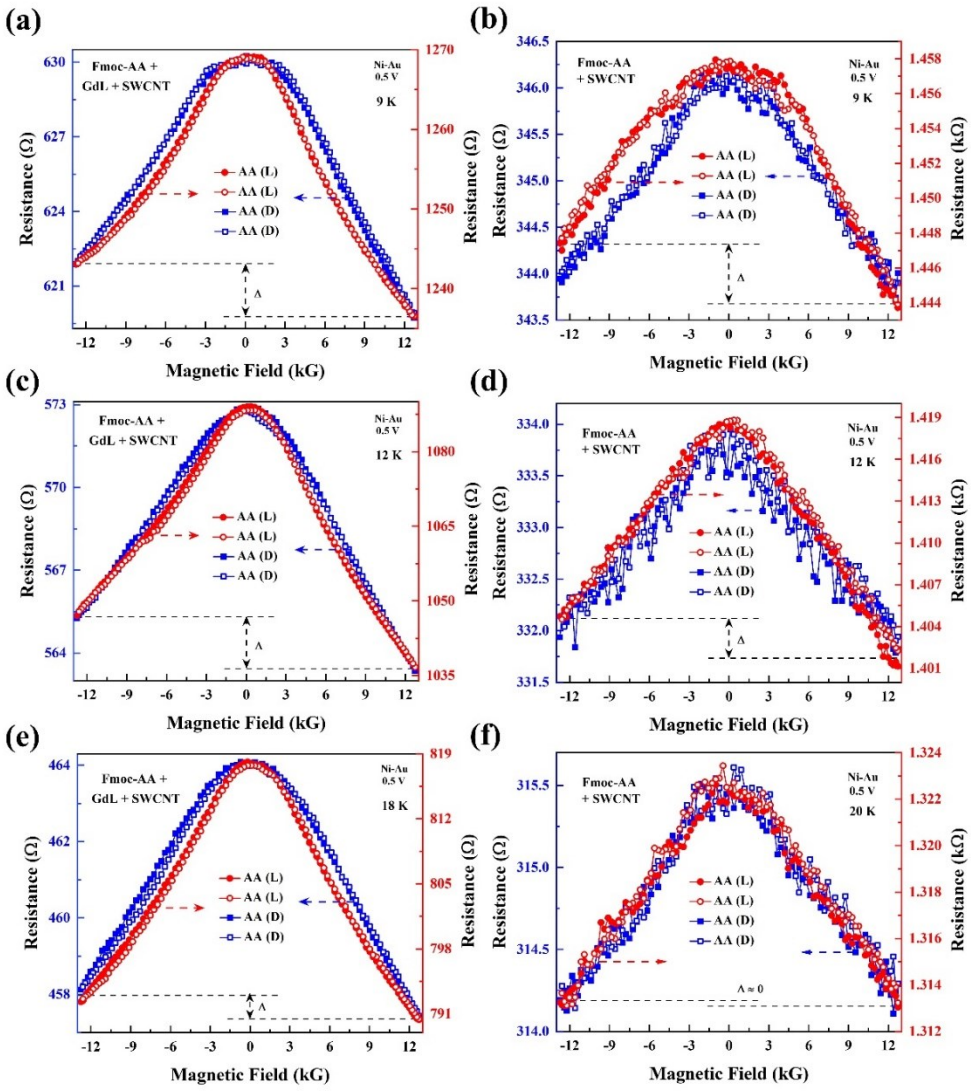

Figure 6. 6. (a), (c), (e) *Asymmetric MR (∅ = 90°) of chiral SWCNTs functionalized with Fmoc-AA (L/D) + GdL at various temperatures.* ***(b), (d), (f)*** *Asymmetric MR (∅ = 90°) of chiral SWCNTs functionalized with only Fmoc-AA (L/D) at various temperatures. Applied bias is 0.5 V in all cases. Solid (open) symbols indicate magnetic field scan from negative (positive) to positive (negative) fields. MR asymmetry has been found to be chirality dependent.*

However, similar to Fmoc-AA, Fmoc-AA (L and D) + GdL functionalized CNT samples are also *independent* of molecular chirality, and it is *positive* for both L and D samples Figure 6.7 (c), (d). The angle dependent normalized Δ (Figure 6.7 (e), (f)) behaviour is the same in both situations of Fmoc-AA and Fmoc-AA (L and D) + GdL. The chirality independence can be explained by referencing the above-mentioned weak interaction of the chiral side chain with CNTs.

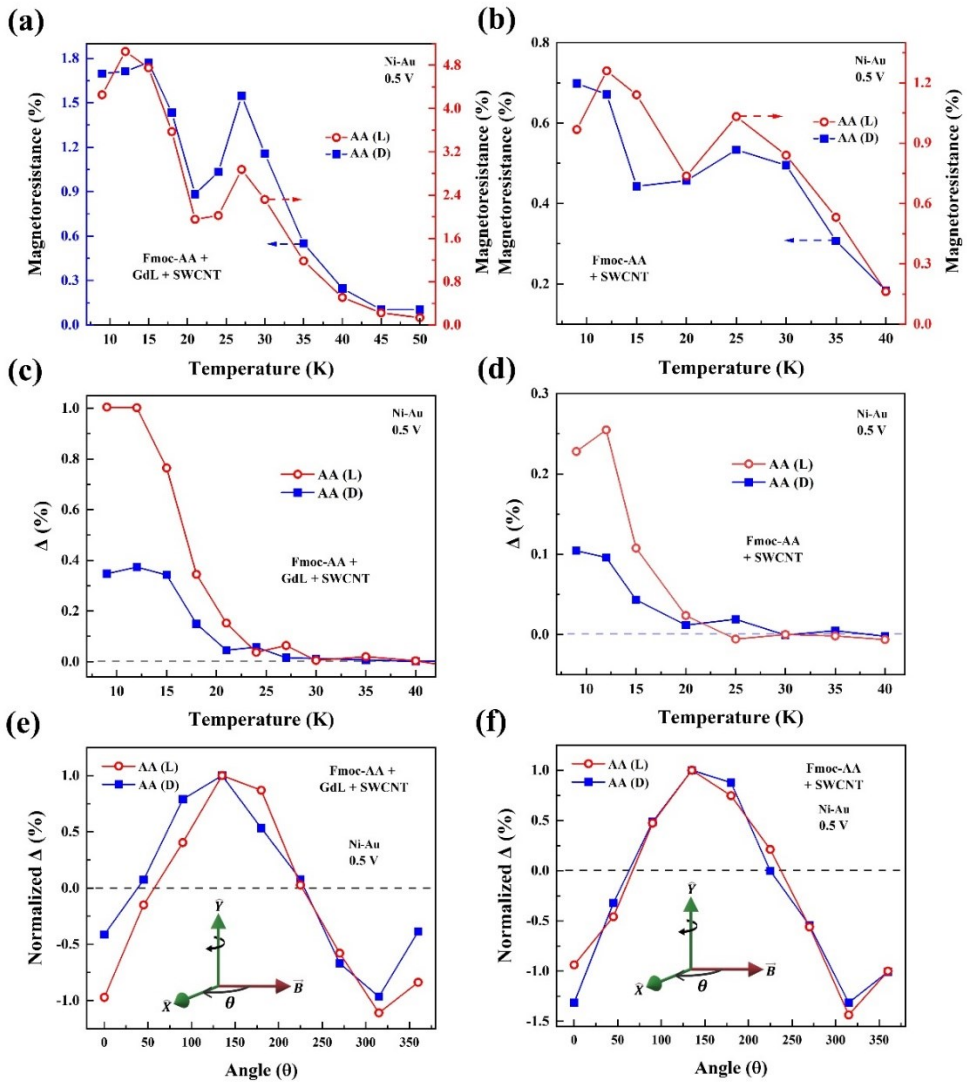

Figure 6. 7. (a), (b) *Temperature dependence of background MR (at $\theta = 90^{o}$) for Fmoc-AA (L/D) + GdL functionalized and only Fmoc-AA (L/D) functionalized SWCNTs respectively.* ***(c), (d)*** *MR asymmetry Δ (%) as a function of temperature (at $\theta = 90^{o}$) for Fmoc-AA (L/D) + GdL functionalized and only Fmoc-AA (L/D) functionalized SWCNTs respectively.* ***(e), (f)*** *Normalized Δ (%) at different orientations of Ni magnetization. Sample is in the X-Y plane for Fmoc-AA (L/D) + GdL functionalized and only Fmoc-AA (L/D) functionalized SWCNTs respectively. For each sample, normalization is done relative to the corresponding maximum value of Δ. Responses from two different samples are shown for each functionalization. Applied bias is 0.5 V in all cases.*

To obtain a better understanding of the sources of CISS and the influence of multiple molecular chirality, we functionalized CNTs using Fmoc-FF (L or D) + GdL. Fmoc-FF has an aromatic ring on its side chain and interacts with CNTs more strongly than the others. The current-voltage I-V characteristics of the Fmoc-FF + GdL samples (both L and D) are shown in the Figures 6.8 (a), (c). The Fmoc-FF + GdL samples have the same semiconducting behaviour and do not display weak metallic behaviour at high temperatures like only Fmoc-FF (*insets* of Figures 6.8 (a),

(c)). The temperature-dependent resistance R(T) fitting using the 2D VRH model is shown in Figures 6.8 (b), (d), where a linear trend is observed over a wide temperature range.

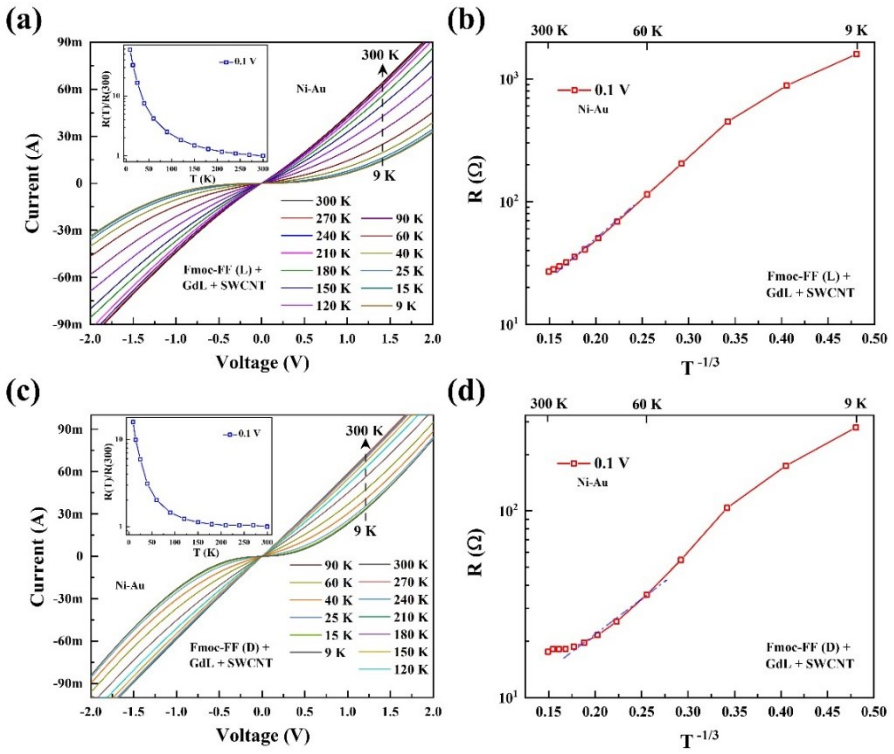

Figure 6. 8. *Current-voltage (*I-V*) characteristics of* ***(a)*** *Fmoc-FF (L) + GdL and* ***(c)*** *Fmoc-FF (D) + GdL functionalized SWCNTs with Ni-Au contacts.* ***(b), (d)*** *Fitting of device resistance* R *(= d*V*/d*I*) with the variable range hopping model for* d *= 2.*

Fmoc-FF (L and D) + GdL exhibits a non-zero Δ for each functionalization, as do Fmoc-FF samples shown in Figures 6.9 (a)-(f). However, Fmoc-FF (L and D) + GdL functionalized samples, the L samples are positive, and the D samples are negative (Figures 6.9 (a), (c), (e)), which is exactly the opposite behaviour observed with only Fmoc-FF functionalized samples (Figures 6.9 (b), (d), (f)). This indicates that despite GDL not directly interacting with the CNTs, it influences the CISS behaviour indirectly by additional chiral center in the medium.

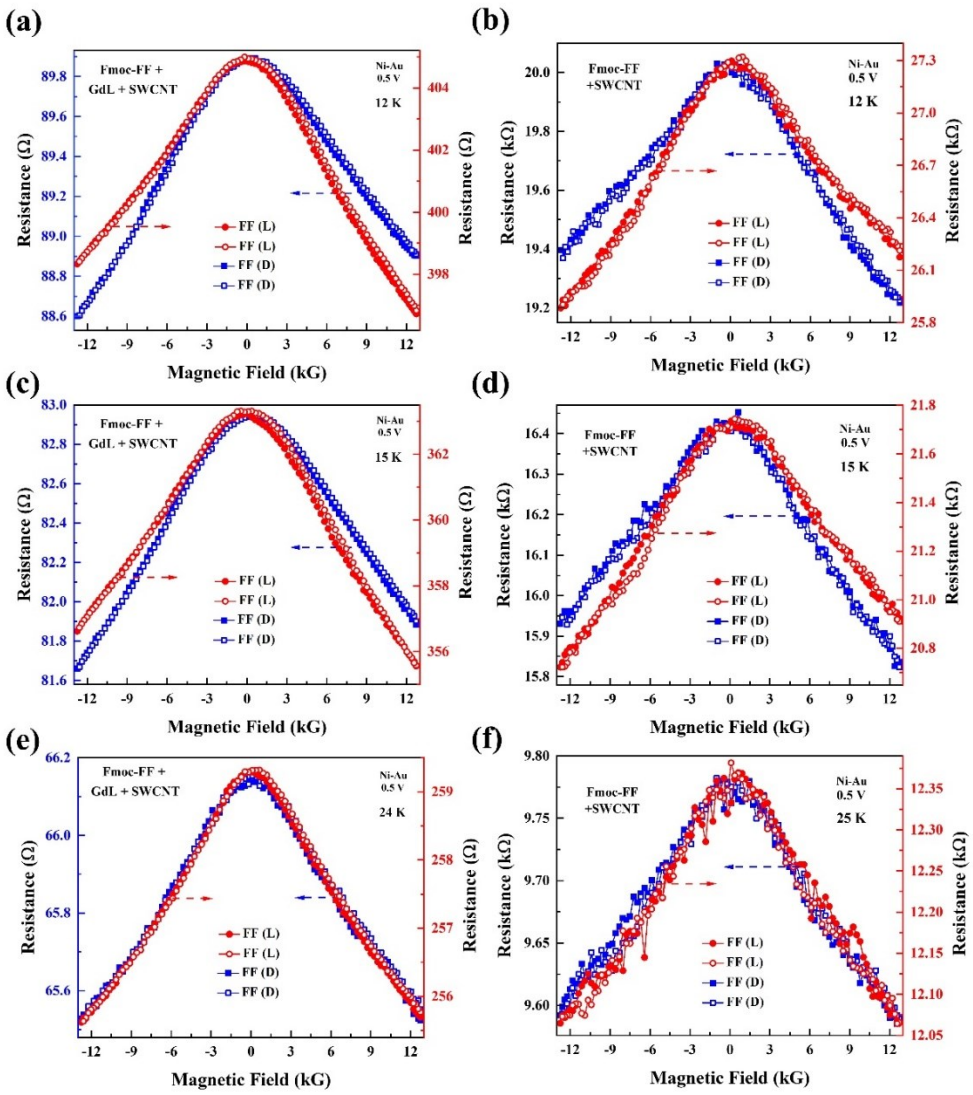

Figure 6. 9. (a), (c), (e) *Asymmetric MR ($\theta = 90^{o}$) of chiral SWCNTs functionalized with Fmoc-FF (L/D) + GdL at various temperatures.* ***(b), (d), (f)*** *Asymmetric MR ($\theta = 90^{o}$) of chiral SWCNTs functionalized with only Fmoc-FF (L/D) at various temperatures. Applied bias is 0.5 V in all cases. Solid (open) symbols indicate magnetic field scan from negative (positive) to positive (negative) fields. MR asymmetry has been found to be chirality dependent.*

Figures 6.10 (a)-(c) depicts the bias dependence of resistance at 9K for both Fmoc-FF (L and D) + GdL functionalized samples (estimated by numerical differentiation of I-V data). Similarly, Figures 6.10 (b)-(d) depicts the bias dependence of resistance at 9K for both Fmoc-FF (L and D) functionalized samples. *Insets* of Figures 6.10 (a)-(b) shows the opposite behaviour for L and D. It's apparent that, Fmoc-FF (L and D) + GdL functionalized samples exhibit the opposite tendency as Fmoc-FF (L and D) functionalized samples.

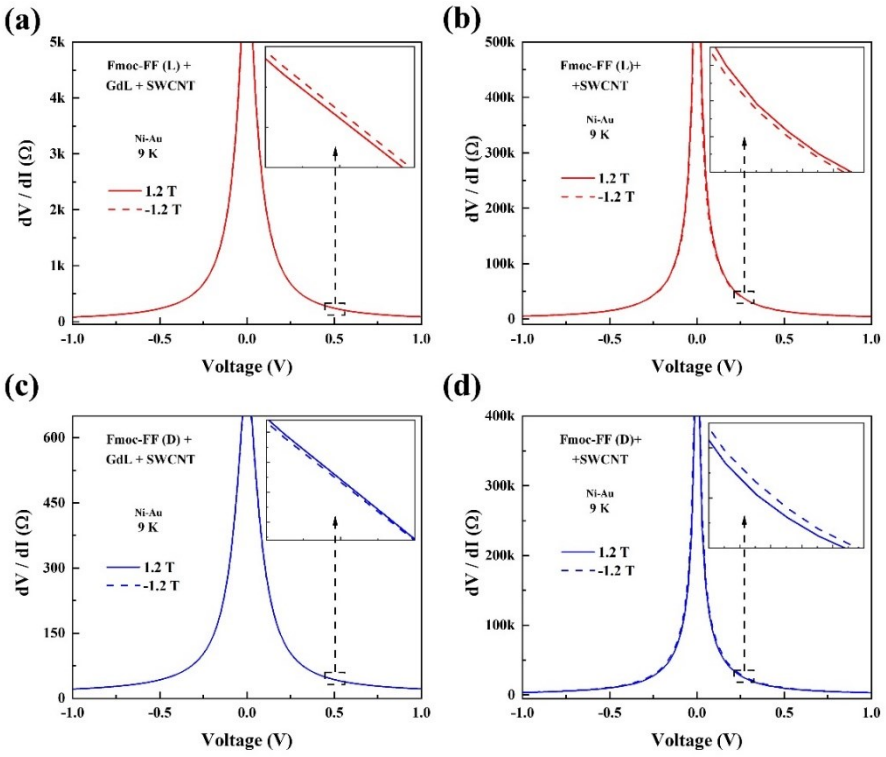

Figure 6. 10. (a), (c) *Differential resistance (dV/dI) vs bias (V) of chiral SWCNTs functionalized with Fmoc-FF (L/D) + GdL at various temperatures (θ = 90°).* ***(b), (d)*** *Differential resistance (dV/dI) vs bias (V) of chiral SWCNTs functionalized with only Fmoc-FF (L/D) at various temperatures (θ = 90°).*

All these findings, MR responses and *normalized* Δ with temperature are presented in the Figure 6.11 (a)-(c) for the Fmoc-FF (L and D) + GdL functionalized samples. The angle (θ ~ 0°-360°) dependent normalized Δ (at 9*K*) Figure 6.11 (e), demonstrate that the chirality-dependent response appears only in a few limited ranges of θ (in the vicinity of 90° and 270°), where Δ has a periodicity of ~360°. This is in line with the usual CISS behaviour, in which Ni magnetization and chirality work together to favor one direction for current flow. However, MR responses, *normalized* Δ with temperature and angle dependent *normalized* Δ (at 9*K*) for only Fmoc-FF (L and D) functionalized samples are presented in the Figure 6.11 (b), (d), (f). Interestingly, MR responses, *normalized* Δ with temperature and angle dependent *normalized* Δ behaviour of Fmoc-FF (L and D) + GdL samples exhibited the opposite trend as the Fmoc-FF samples.

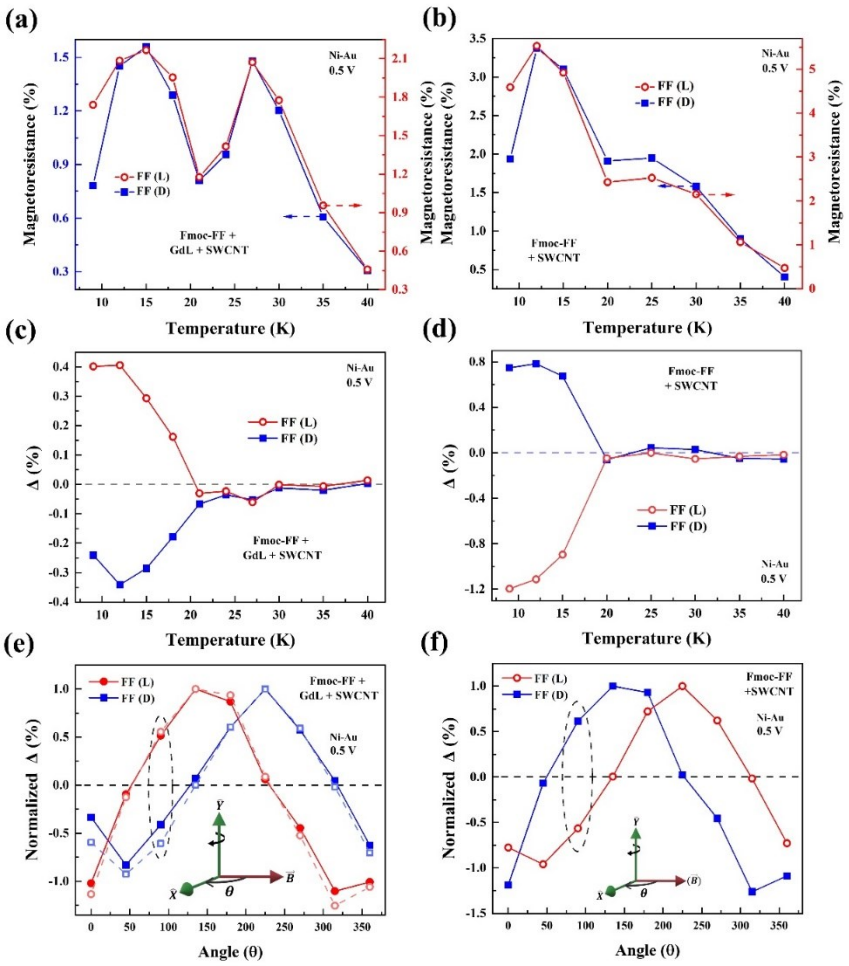

Figure 6. 11. (a), (b) *Temperature dependence of background MR (at $\theta = 90^{o}$) for Fmoc-FF (L/D) + GdL functionalized and only Fmoc-FF (L/D) functionalized SWCNTs respectively.* ***(c), (d)*** *MR asymmetry Δ (%) as a function of temperature (at $\theta = 90^{o}$) for Fmoc-FF (L/D) + GdL functionalized and only Fmoc-FF (L/D) functionalized SWCNTs respectively.* ***(e), (f)*** *Normalized Δ (%) at different orientations of Ni magnetization. Sample is in the X-Y plane for Fmoc-FF (L/D) + GdL functionalized and only Fmoc-FF (L/D) functionalized SWCNTs respectively. For each sample, normalization is done relative to the corresponding maximum value of Δ. Responses from two different samples are shown for each functionalization. Applied bias is 0.5 V in all cases.*

6.3 Conclusion

The purpose of this study was to test the role of multiple molecular functionalizations on spin polarization in two-dimensional carbon nanotube networks. It has been shown that presence of a different chiral molecules (such as GdL) can flip the CISS polarity even though it is not directly interacting with the CNTs. This observation indicates possibility of tuning the CISS effect further by adding even more chiral molecules in the medium. Presence of multiple scattering centers may make the MR signals more immune to temperature. We will explore these aspects in the next chapter.

Chapter 7. Future work – Further Exploration of Spin-Dependent Phenomena in Mixed Chiral Media

7.1 Introduction

Earlier chapter indicated that introduction of mixed chiral molecules in 2D CNT networks can change the spin signal in a non-trivial way. In our previous experiment, however, GdL didn't bind directly with CNTs, but still affected the spin-dependent response. Here we introduce another molecule (L-) Lysozyme (LZM), which binds with CNTs along with Fmoc-FF. Our initial studies on $\theta = 0^{o}$ are presented below. Analysis for other angles, especially 90^{o}, are in progress.

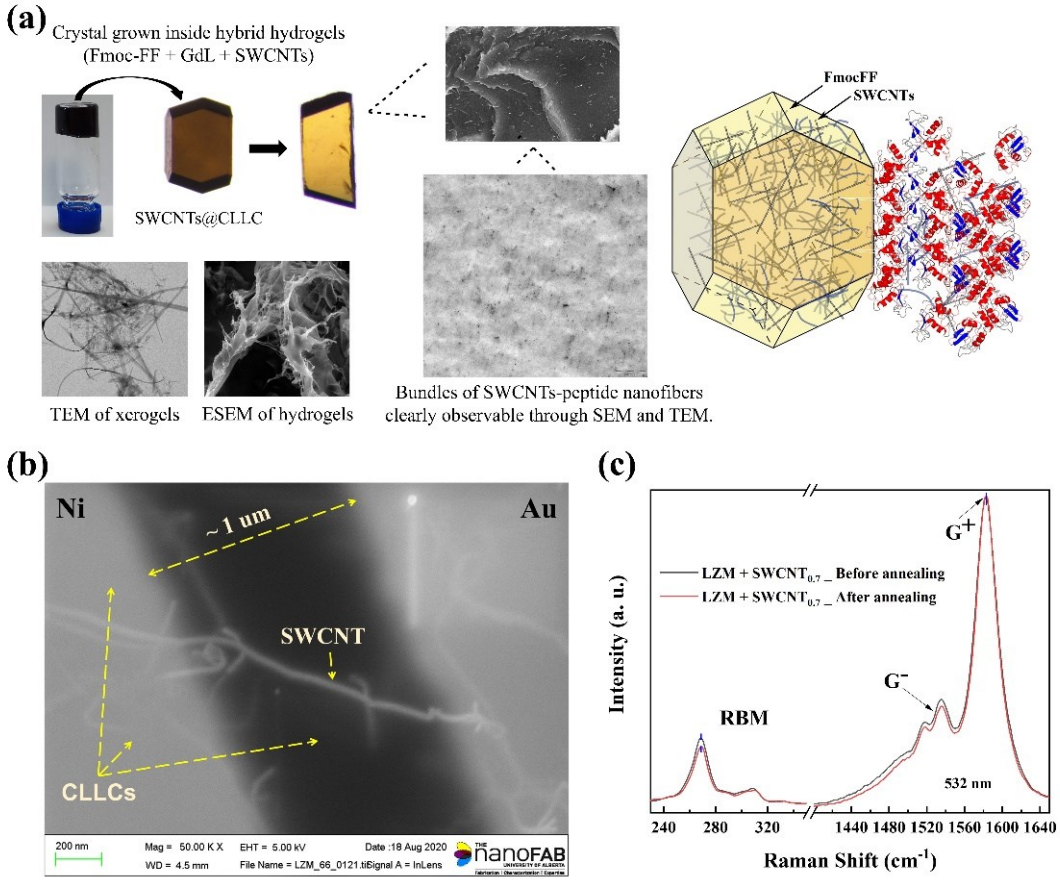

Figure 7. 1 (a) *Cross-linked lysozyme crystal (SWCNT@CLLC) and its internal structure.* ***(b)*** *FESEM image of LZM+CNTs (0.7 mg/ml) on top of pre-patterned Ni-Au electrodes.* ***(c)*** *Raman characterization of LZM+CNTs (0.7 mg/ml).*

7.2 Sample Synthesis

Using a protocol described in a recent work,[135] controlled amounts of SWCNT (single wall carbon nanotube, Sigma-Aldrich, 308068-56-6, ~95% semiconducting with ~41% having (6, 5) chirality) bundles were introduced inside LZM matrix to form a SWCNT-loaded cross-linked lysozyme crystal (SWCNT@CLLC). Briefly, as described in the previous chapter, SWCNTs were first incorporated in Fmoc-diphenylalanine (Fmoc-FF) peptide hydrogels, which are chosen to be either L- or D-chiral. Next, protein solution was inter-diffused into the composite hydrogel and where GdL was added. Finally, SWCNT@CLLC crystals were precipitated by adding a precipitant solution (sodium chloride 6% w/v in 50×10^{-3} M sodium acetate pH 4.5). Thus, the CNTs in the SWCNT@CLLC crystal experience three chiral sources - (a) L-chiral LZM and (b) L- or D-chiral Fmoc-FF, and (c) GdL, as described schematically in Figure 7.1(a). The above-described synthesis process were performed by our collaborators at Universidad de Granada, 18071 Granada, Spain. Fabrication of the device as well as spin transport experiments were performed by us.

7.3 Results and Discussion

The following samples have been tested: SWCNT@CLLC crystals with varying SWCNT concentrations (0.1, 0.25, 0.5 and 0.7 mg/ml) and with two different chiralities of Fmoc-FF. We also tested two types of control samples: LZM crystals grown in water (no Fmoc-FF or SWCNT) and LZM crystals grown in Fmoc-FF (no SWCNT).

For transport experiments, devices were fabricated as follows. The samples described above were embedded in epoxy resin EMbed-812 (Electron Microscopy Sciences, USA) and placed in a 60°C oven for 48–72 hours for polymerization. Serial ultrathin sections (~ 100–900 nm range) were sliced sequentially by a Reichert Ultracut S microtome (Leica Microsystems, Germany). Next, the sections were transferred on interdigitated Au-Au and Ni-Au electrodes (electrode thickness ~100 nm, electrode gap ~1 μm) photolithographically patterned on SiO_2 (500 nm)/Si wafer. Finally, the devices were vacuum annealed (200°C for 30 mins) to improve electrical contacts between the electrodes and the transferred sections. For Raman characterization, the sections were placed on glass substrates with all other fabrication steps described above remaining the same.

Figure 7.1(b) shows FESEM image of a section (0.7 mg/ml SWCNT) transferred on Ni/Au electrodes. The white strands in this image indicate interconnected SWCNT networks, embedded within the protein/gel crystal, extending between the two electrodes. Figure 7.1(c) shows representative Raman spectrum (532 nm excitation, room temperature) before and after annealing of the sections. Two main features of SWCNTs,[80] RBM mode and TM mode can be seen. Annealing doesn't appear to have any adverse effect on nanotube crystal structure or its interaction with the surrounding medium.

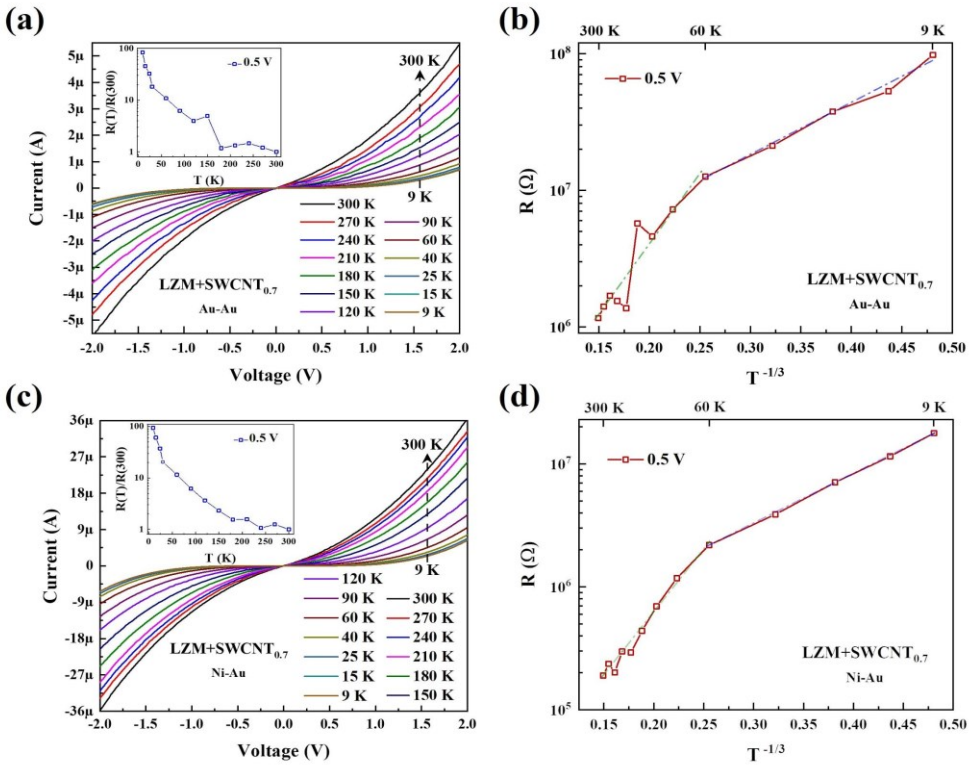

Figure 7. 2 *Current-voltage (I-V) characteristics at B = 0 and fitting with the VRH model with d = 2 for LZM + CNT (0.7 mg/ml) samples. (a), (b) Au-Au electrodes and (c), (d) Ni-Au electrodes. The insets show normalized resistance, measured at 0.5 V, as a function of temperature.*

To understand the electrical transport properties of the samples described above, temperature (T)-dependent (9 K–300 K) current-voltage (I-V) measurements have been performed using Au-Au and Ni-Au contacts under zero magnetic field. Figure 7.2 shows data from 0.7 mg/ml CNT samples, which exhibits semiconducting temperature-dependence. Data from 0.5 mg/ml CNT samples are presented in the Figure AP 15 in Appendix, which also exhibit the same temperature-dependence. The contact resistances are ~ 6 orders of magnitude smaller than the actual devices and hence their role in the electrical measurements is negligible. Control samples

with no SWCNT content (both LZM and LZM + Fmoc-FF) and low SWCNT content (0.1 and 0.25 mg/ml) show currents that are below the detection level of our measurement setup. Therefore, in this chapter we report data from samples with SWCNT concentrations of 0.5 and 0.7 mg/ml. This indicates that the chiral matrix does not directly participate in electron conduction, at least not on the length scale used in this experiment. Absence of significant conductance from lower nanotube concentration samples indicate absence of interconnecting nanotube networks extending between the electrodes in such samples. Sections with different thicknesses (100 nm, 300 nm, 500 nm, 700 nm, 900 nm) were also tested from 0.5 and 0.7 mg/ml SWCNT samples. Measurable current values were obtained only from 700 nm and 900 nm thick samples, indicating that in the thinner slices' nanotube networks are below the conduction percolation threshold. In this chapter we will report data from 900 nm thick samples.

Figures 7.2(a), (c) show *I-V* data from samples with 0.7 mg/ml SWCNT using Au-Au and Ni-Au contacts respectively. Transport is non-linear over the measured bias range. The *insets* show orders of magnitude decrease in device resistance R as the sample temperature is increased ($dR/dT < 0$). Such strong temperature-dependence is typically described using variable-range hopping (VRH) model[197] described in earlier chapters. Figures 7.2(b) and (d) show fittings with the VRH model for d = 2. Additional fitting with d = 1 has been shown in the Figure AP 16 in Appendix. Linear fit is observed over a wide temperature range (60–300K). At lower temperatures (9–60K), linear fit is still observed, albeit with a smaller slope. As seen from Figure AP 15 in Appendix, SWCNT@CLLC (0.5 mg/ml) samples also show qualitatively the same features.

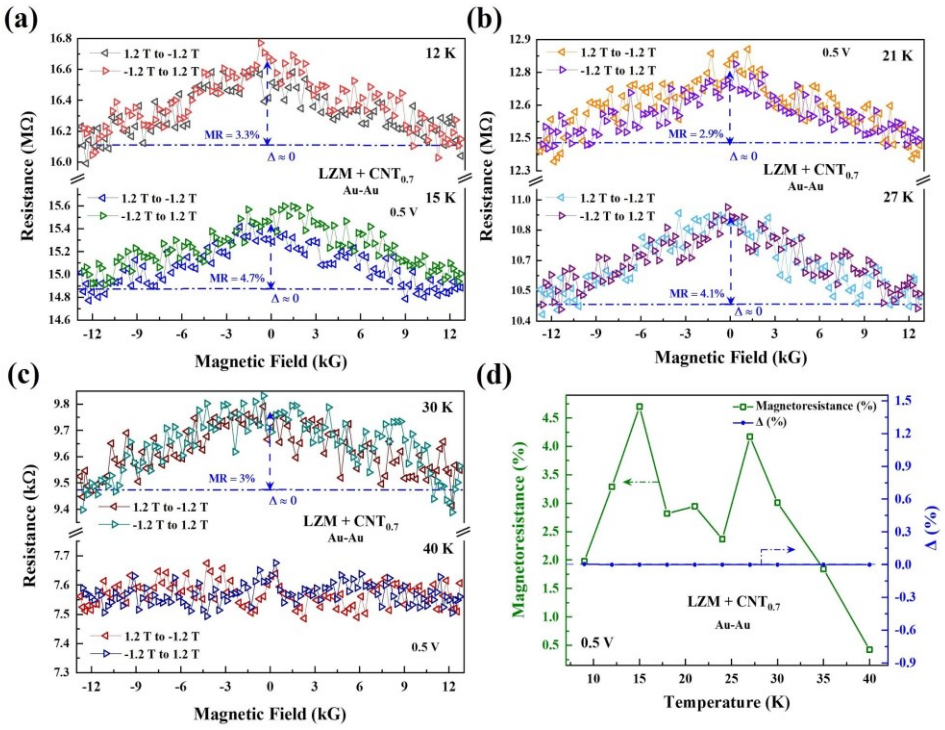

Figure 7. 3. (a)-(c) *Symmetric MR of LZM+CNTs (0.7 mg/ml) with Au-Au contacts at representative temperatures (applied bias is 0.5 V in all cases)* ***(d)*** *Temperature- dependence of background MR and Δ.*

Figures 7.3 (a)-(c) show representative magnetoresistance (MR) data from SWCNT@CLLC (0.7 mg/ml) samples in the range +/- 1.2 Tesla, measured at 0.5 V bias, using Au-Au contacts. The MR responses shown in Figure 7.3 are for $\theta = 0^{o}$, which corresponds to in-plane magnetic field. The MR studies for $\theta = 90^{o}$ are in progress. As expected, a negative background MR (~ 4%) is observed, which is symmetric ($\Delta = 0$) with respect to the magnetic field direction, at all temperatures (Figure 7.3(d)). As summarized in Figure 7.3(d), a "double peak" feature is observed in the background MR response. The background MR disappears at higher temperatures (> 60 K) in the measured field range. Multiple samples have been tested and they all exhibit the same behaviour.

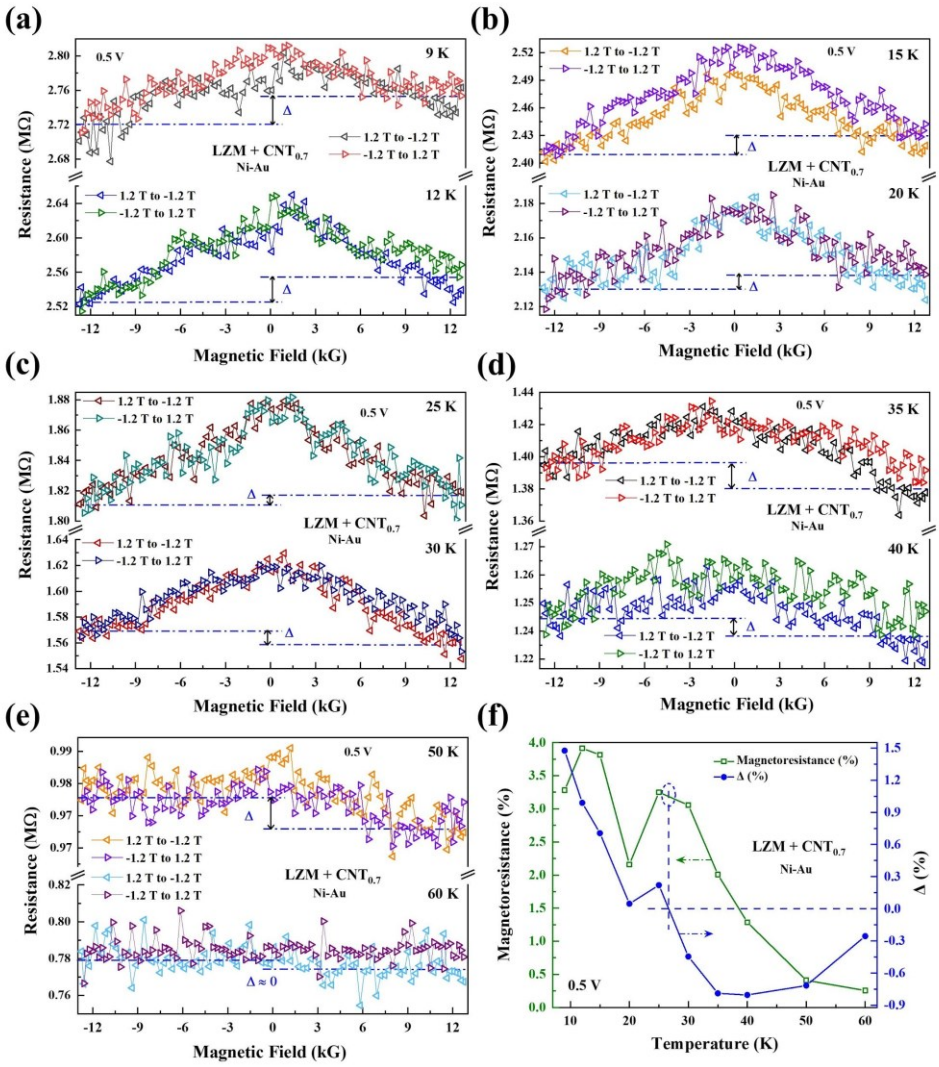

Figure 7. 4 (a)-(e) *Asymmetric MR of LZM+CNTs (0.7 mg/ml) with Ni-Au contacts at representative temperatures (applied bias is 0.5 V in all cases).* ***(f)*** *Temperature-dependence of background MR and Δ.*

Figure 7.4 (a)-(e) show MR data from SWCNT@CLLC (0.7 mg/ml) samples with Ni-Au contacts. The background MR and its non-monotonic dependence on temperature ("double peak" feature) observed before are still present, as summarized in Figure 7.4(f). The MR responses are asymmetric, resulting in non-zero Δ (~ 1.5%). As noted before, the chiral matrix is essentially insulating for the present set of measurements, so the asymmetry in MR cannot be explained by the CISS effect of the matrix itself. Interestingly, temperature evolution of Δ shows a zero-crossing and hence flipping of spin polarization, before it completely disappears at ~ 60 K. Temperature evolution of Δ is also shown in Figure 7.4(f). Especially noteworthy is that the zero crossing of Δ and the second MR peak occur in the same temperature range. Similar features have been observed

in SWCNT@CLLC (0.5 mg/ml) samples as well (Figure AP 15 in Appendix), however, magnitudes of MR and Δ are smaller in this case. Data from a second 0.7 mg/ml CNT sample is shown in Figure AP 17(a) in Appendix, which also shows the same features. This zero crossing Δ was completely missing in previous situations (Chapter 5 and 6) when SWCNT was functionalized using Fmoc-dipeptides and Fmoc-dipeptides+GdL.

CISS-induced spin signal (Δ) decays with temperature, because spin-polarized carriers travel through nanotubes, and it has been well-established in the earlier chapters (chapters 5 and 6) that in nanotube medium spin-polarization decays with temperature due to scattering effects.[187] What is new in this case is the observation of zero-crossing in the 20–30K range, which indicates spin flipping within the nanotube system. We also observe that the second MR peak and zero-crossing/spin-flipping occur in the same temperature range. These features have been observed in SWCNT@CLLC (0.5 mg/ml) samples as well (Figure AP 15(f)). We are working on additional experiments to understand the origin of these features.

Chapter 8. Conclusion

In conclusion, we have reported successful and reproducible fabrication of individual long (~2-4 x) carbon nanotubes wrapped with single-stranded DNA (Chapter 2). The wrapped tubes have been characterized extensively using various techniques, and they reveal a high degree of dispersion of nanotubes, complete DNA wrapping along nanotube length without any evidence of discontinuity and tight physical contact between DNA and nanotube. Long DNA-wrapped tubes are becoming increasingly important in the emerging area of chiral spintronics, where it has been found that longer tubes can increase the spin polarization of charge carriers in electrical transport devices. Later, we explored the effect of CISS on charge transport in CNTs (Chapter 3). This work demonstrates CISS as a mechanism to engineer not only spin polarization but also charge transfer processes at the nanoscale. In the following study (Chapter 4), we further investigated the observed negative background magnetoresistance, which originates from the interference effects between the forward and backward hopping paths. CISS-induced spin polarization has been estimated to increase the carrier localization length by an order of magnitude in the low temperature range and it affects the magnetoresistance effect in a non-trivial way that is not observed in conventional systems.

By using the versatility of peptide chemistry, we demonstrate in Chapter 5 how spin polarization depends on molecular structural features such as chirality (non-helical) as well as molecule-nanotube interactions. In addition to the more frequent chirality-dependent effect, a novel form of chirality-independent effect was discovered, and the total spin signal was found to be a mix of both. Finally, the magnetic field dependency of the spin signals was investigated, and the "chirality dependent" signal was shown to exist only at specific field angles. The influence of multiple chiral media on 2D carbon nanotube networks is investigated in the following experiments (Chapter 6 and 7). The results show that when two or more chiral systems are present, both chirality-dependent and chirality-independent processes contribute to the CISS effect.

References

(1) Fert, A.; Van Dau, F. N. Spintronics, from Giant Magnetoresistance to Magnetic Skyrmions and Topological Insulators. *Comptes Rendus Phys.* **2019**, *20* (7–8), 817–831. https://doi.org/10.1016/j.crhy.2019.05.020.

(2) Felser, C. *Spintronics: From Materials to Devices*; Springer Berlin Heidelberg: New York, 2013. https://doi.org/DOI 10.1007/978-90-481-3832-6.

(3) Naaman, R.; Paltiel, Y.; Waldeck, D. H. Chiral Molecules and the Spin Selectivity Effect. *J. Phys. Chem. Lett.* **2020**, *11* (9), 3660–3666. https://doi.org/10.1021/acs.jpclett.0c00474.

(4) Naaman, R.; Waldeck, D. H. Chiral-Induced Spin Selectivity Effect. *J. Phys. Chem. Lett.* **2012**, *3* (16), 2178–2187. https://doi.org/10.1021/jz300793y.

(5) Xie, Z.; Markus, T. Z.; Cohen, S. R.; Vager, Z.; Gutierrez, R.; Naaman, R. Spin Specific Electron Conduction through DNA Oligomers. *Nano Lett.* **2011**, *11* (11), 4652–4655. https://doi.org/10.1021/nl2021637.

(6) Kettner, M.; Göhler, B.; Zacharias, H.; Mishra, D.; Kiran, V.; Naaman, R.; Fontanesi, C.; Waldeck, D. H.; Sek, S.; Pawowski, J.; Juhaniewicz, J. Spin Filtering in Electron Transport Through Chiral Oligopeptides. *J. Phys. Chem. C* **2015**, *119* (26), 14542–14547. https://doi.org/10.1021/jp509974z.

(7) Naaman, R.; Waldeck, D. H. Spintronics and Chirality: Spin Selectivity in Electron Transport Through Chiral Molecules. *Annu. Rev. Phys. Chem.* **2015**, *66* (1), 263–281. https://doi.org/10.1146/annurev-physchem-040214-121554.

(8) Liu, Y.; Xiao, J.; Koo, J.; Yan, B. Chirality-Driven Topological Electronic Structure of DNA-like Materials. *Nat. Mater.* **2021**, *20* (5), 638–644. https://doi.org/10.1038/s41563-021-00924-5.

(9) Ghazaryan, A.; Paltiel, Y.; Lemeshko, M. Analytic Model of Chiral-Induced Spin Selectivity. *J. Phys. Chem. C* **2020**, *124* (21), 11716–11721. https://doi.org/10.1021/acs.jpcc.0c02584.

(10) Guo, A. M.; Pan, T. R.; Fang, T. F.; Xie, X. C.; Sun, Q. F. Spin Selectivity Effect in Achiral Molecular Systems. *Phys. Rev. B* **2016**, *94* (16), 1–5. https://doi.org/10.1103/PhysRevB.94.165409.

(11) Fiori, G.; Bonaccorso, F.; Iannaccone, G.; Palacios, T.; Neumaier, D.; Seabaugh, A.; Banerjee, S. K.; Colombo, L. Electronics Based on Two-Dimensional Materials. *Nat. Nanotechnol.* **2014**, *9* (10), 768–779. https://doi.org/10.1038/nnano.2014.207.

(12) Ferrari, A. C.; Bonaccorso, F.; Fal'ko, V.; Novoselov, K. S.; Roche, S.; Bøggild, P.; Borini, S.; Koppens, F. H. L.; Palermo, V.; Pugno, N.; Garrido, J. A.; Sordan, R.; Bianco, A.; Ballerini, L.; Prato, M.; Lidorikis, E.; Kivioja, J.; Marinelli, C.; Ryhänen, T.; Morpurgo, A.; Coleman, J. N.; Nicolosi, V.; Colombo, L.; Fert, A.; Garcia-Hernandez, M.; Bachtold, A.; Schneider, G. F.; Guinea, F.; Dekker, C.; Barbone, M.; Sun, Z.; Galiotis, C.; Grigorenko, A. N.; Konstantatos, G.; Kis, A.; Katsnelson, M.; Vandersypen, L.; Loiseau, A.; Morandi, V.; Neumaier, D.; Treossi, E.; Pellegrini, V.; Polini, M.; Tredicucci, A.; Williams, G. M.; Hee Hong, B.; Ahn, J. H.; Min Kim, J.; Zirath, H.; Van Wees, B. J.; Van Der Zant, H.; Occhipinti, L.; Di Matteo, A.; Kinloch, I. A.; Seyller, T.; Quesnel, E.; Feng, X.; Teo, K.; Rupesinghe, N.; Hakonen, P.; Neil, S. R. T.; Tannock, Q.; Löfwander, T.; Kinaret, J. Science and Technology Roadmap for Graphene, Related Two-Dimensional Crystals, and Hybrid Systems. *Nanoscale* **2015**, *7* (11), 4598–4810. https://doi.org/10.1039/c4nr01600a.

(13) Diniz, G. S.; Latgé, A.; Ulloa, S. E. Helicoidal Fields and Spin Polarized Currents in Carbon Nanotube-DNA Hybrids. *Phys. Rev. Lett.* **2012**, *108* (12), 1–4. https://doi.org/10.1103/PhysRevLett.108.126601.

(14) Alam, K. M.; Pramanik, S. Spin Filtering through Single-Wall Carbon Nanotubes Functionalized with Single-Stranded DNA. *Adv. Funct. Mater.* **2015**, *25* (21), 3210–3218. https://doi.org/10.1002/adfm.201500494.

(15) Alam, K. M.; Pramanik, S. Spin Filtering with Poly-T Wrapped Single Wall Carbon Nanotubes. *Nanoscale* **2017**, *9* (16), 5155–5163. https://doi.org/10.1039/c6nr09395g.

(16) Baibich, M. N.; Broto, J. M.; Fert, A.; Van Dau, F. N.; Petroff, F.; Eitenne, P.; Creuzet, G.; Friederich, A.; Chazelas, J. Giant Magnetoresistance of (001)Fe/(001)Cr Magnetic Superlattices. *Phys. Rev. Lett.* **1988**, *61* (21), 2472–2475. https://doi.org/10.1103/PhysRevLett.61.2472.

(17) Grünberg, P. A. Nobel Lecture: From Spin Waves to Giant Magnetoresistance and Beyond. *Rev. Mod. Phys.* **2008**. https://doi.org/10.1103/revmodphys.80.1531.

(18) Reig, C.; Cardoso de Freitas, S.; Chandra Mukhopadhyay, S. *Giant Magnetoresistance (GMR) Sensors. From Basis to State-of-the-Art Applications*; 2013. https://doi.org/10.1007/978-3-642-37172-1.

(19) Ennen, I.; Kappe, D.; Rempel, T.; Glenske, C.; Hütten, A. Giant Magnetoresistance: Basic Concepts, Microstructure, Magnetic Interactions and Applications. *Sensors (Switzerland)* **2016**, *16* (6). https://doi.org/10.3390/s16060904.

(20) Chappert, C., Fert, A. & V. D. The Emergence of Spin Electronics in Data Storage. *Nat. Mater.* **2007**, *6* (11), 813–823. https://doi.org/10.1038/nmat2024.

(21) Awschalom, D. D.; Flatté, M. E. Challenges for Semiconductor Spintronics. *Nat. Phys.* **2007**, *3* (3), 153–159. https://doi.org/10.1038/nphys551.

(22) Rocha, A. R.; García-SUÁREZ, V. M.; Bailey, S. W.; Lambert, C. J.; Ferrer, J.; Sanvito, S. Towards Molecular Spintronics. *Nat. Mater.* **2005**, *4* (4), 335–339. https://doi.org/10.1038/nmat1349.

(23) *Organic Spintronics*, 1st ed.; Zeev Valy Vardeny, Ed.; CRC Press: New York, 2010.

(24) Dieny, B.; Speriosu, V. S.; Parkin, S. S. P.; Gurney, B. A.; Wilhoit, D. R.; Mauri, D. Giant Magnetoresistive in Soft Ferromagnetic Multilayers. *Phys. Rev. B* **1991**, *43* (1), 1297–1300. https://doi.org/10.1103/PhysRevB.43.1297.

(25) B. Dieny. Magnetism Giant Magnetoresistance in Spin-Valve Multilayers. *J. Magn. Magn. Mater.* **1994**, *136* (94), 335–359.

(26) Tsang, C.; Fontana, R. E.; Lin, T.; Heim, D. E.; Speriosu, V. S.; Gurney, B. A.; Williams, M. L. Design, Fabrication and Testing of Spin-Valve Read Heads for High Density Recording. In *IEEE Transactions on Magnetics*; 1994; Vol. 30, pp 3801–3806. https://doi.org/https://doi.org/10.1109/20.333909.

(27) Lodder, J. C.; Monsma, D. J.; Vlutters, R.; Shimatsu, T. Spin-Valve Transistor: Technologies and Progress. *J. Magn. Magn. Mater.* **1999**, *198*, 119–124. https://doi.org/10.1016/S0304-8853(98)01241-4.

(28) Quindeau, A.; Fina, I.; Marti, X.; Apachitei, G.; Ferrer, P.; Nicklin, C.; Pippel, E.; Hesse, D.; Alexe, M. Four-State Ferroelectric Spin-Valve. *Sci. Rep.* **2015**, *5*, 1–7. https://doi.org/10.1038/srep09749.

(29) Urdampilleta, M.; Klyatskaya, S.; Cleuziou, J. P.; Ruben, M.; Wernsdorfer, W. Supramolecular Spin Valves. *Nat. Mater.* **2011**, *10* (7), 502–506. https://doi.org/10.1038/nmat3050.

(30) Tombros, N.; Jozsa, C.; Popinciuc, M.; Jonkman, H. T.; Van Wees, B. J. Electronic Spin Transport and Spin Precession in Single Graphene Layers at Room Temperature. *Nature* **2007**, *448* (7153), 571–574. https://doi.org/10.1038/nature06037.

(31) Iqbal, M. Z.; Siddique, S.; Hussain, G. Spin Valve Effect of 2D-Materials Based Magnetic Junctions. *Adv. Eng. Mater.* **2018**, *20* (5), 1700692. https://doi.org/10.1002/adem.201700692.

(32) Julliere, M. Tunneling between Ferromagnetic Films. *Phys. Lett. A* **1975**, *54* (3), 225–226. https://doi.org/10.1016/0375-9601(75)90174-7.

(33) Moodera, J. S.; Kinder, L. R.; Wong, T. M.; Meservey, R. Large Magnetoresistance at Room Temperature in Ferromagnetic Thin Film Tunnel Junctions. *Phys. Rev. Lett.* **1995**, *74* (16), 3273–3276. https://doi.org/10.1103/PhysRevLett.74.3273.

(34) Yuasa, S.; Djayaprawira, D. D. Giant Tunnel Magnetoresistance in Magnetic Tunnel Junctions with a Crystalline MgO(0 0 1) Barrier. *J. Phys. D. Appl. Phys.* **2007**, *40* (21), 337–354. https://doi.org/10.1088/0022-3727/40/21/R01.

(35) Lee, Y. M.; Hayakawa, J.; Ikeda, S.; Matsukura, F.; Ohno, H. Effect of Electrode Composition on the Tunnel Magnetoresistance of Pseudo-Spin-Valve Magnetic Tunnel Junction with a MgO Tunnel Barrier. *Appl. Phys. Lett.* **2007**, *90* (21), 2005–2008. https://doi.org/10.1063/1.2742576.

(36) Tezuka, N.; Ikeda, N.; Mitsuhashi, F.; Sugimoto, S. Improved Tunnel Magnetoresistance of Magnetic Tunnel Junctions with Heusler Co2 FeAl0.5 Si0.5 Electrodes Fabricated by Molecular Beam Epitaxy. *Appl. Phys. Lett.* **2009**, *94* (16). https://doi.org/10.1063/1.3116717.

(37) Ikeda, S.; Hayakawa, J.; Ashizawa, Y.; Lee, Y. M.; Miura, K.; Hasegawa, H.; Tsunoda, M.; Matsukura, F.; Ohno, H. Tunnel Magnetoresistance of 604% at 300 K by Suppression of Ta Diffusion in CoFeBMgOCoFeB Pseudo-Spin-Valves Annealed at High Temperature. *Appl. Phys. Lett.* **2008**, *93* (8), 1–4. https://doi.org/10.1063/1.2976435.

(38) Dediu, V. A.; Hueso, L. E.; Bergenti, I.; Taliani, C. Spin Routes in Organic Semiconductors. *Nat. Mater.* **2009**, *8* (9), 707–716. https://doi.org/10.1038/nmat2510.

(39) Chiang, C. K.; C. R. Fincher, J.; Park, Y. W.; Heeger, A. J.; Shirakawa, H.; Louis, E. J.; Gau, S. C.; MacDiarmid, A. G. Electrical Conductivity in Doped Polyacetylene. *Phys. Rev. Lett.* **1977**, *39*, 1098. https://doi.org/https://doi.org/10.1103/PhysRevLett.39.1098.

(40) Geng, R.; Daugherty, T. T.; Do, K.; Luong, H. M.; Nguyen, T. D. A Review on Organic Spintronic Materials and Devices: I. Magnetic Field Effect on Organic Light Emitting Diodes. *J. Sci. Adv. Mater. Devices* **2016**, *1* (2), 128–140. https://doi.org/10.1016/j.jsamd.2016.05.002.

(41) Fahlman, M.; Fabiano, S.; Gueskine, V.; Simon, D.; Berggren, M.; Crispin, X. Interfaces in Organic Electronics. *Nat. Rev. Mater.* **2019**, *4* (10), 627–650. https://doi.org/10.1038/s41578-019-0127-y.

(42) Friend, R. Electroluminescence in Conjugated Polymers. *Nature* **1999**, *397*, 121–128. https://doi.org/https://doi.org/10.1038/16393.

(43) Horowitz, B. G. Organic Field-Effect Transistors. *Adv. Mater.* **1998**, No. 5, 365–377.

(44) Inganäs, O. Organic Photovoltaics over Three Decades. *Adv. Mater.* **2018**, *30* (35), 1–26. https://doi.org/10.1002/adma.201800388.

(45) Sekitani, T.; Nakajima, H.; Maeda, H.; Fukushima, T.; Aida, T.; Hata, K.; Someya, T. Stretchable Active-Matrix Organic Light-Emitting Diode Display Using Printable Elastic Conductors. *Nat. Mater.* **2009**, *8* (6), 494–499. https://doi.org/10.1038/nmat2459.

(46) Horiuchi, S. Organic Ferroelectrics. *Nat. Mater.* **2008**, *7*, 357–366. https://doi.org/https://doi.org/10.1038/nmat2137.

(47) Cinchetti, M.; Heimer, K.; Wüstenberg, J. P.; Andreyev, O.; Bauer, M.; Lach, S.; Ziegler, C.; Gao, Y.; Aeschlimann, M. Determination of Spin Injection and Transport in a Ferromagnet/Organic Semiconductor Heterojunction by Two-Photon Photoemission. *Nat. Mater.* **2009**, *8* (2), 115–119. https://doi.org/10.1038/nmat2334.

(48) Naber, W. J. M.; Faez, S.; Van Der Wiel, W. G. Organic Spintronics. *J. Phys. D. Appl. Phys.* **2007**, *40* (12). https://doi.org/10.1088/0022-3727/40/12/R01.

(49) Jang, H. J.; Richter, C. A. Organic Spin-Valves and Beyond: Spin Injection and Transport in Organic Semiconductors and the Effect of Interfacial Engineering. *Advanced Materials*. 2017. https://doi.org/10.1002/adma.201602739.

(50) Li, B.; Kao, C. Y.; Yoo, J. W.; Prigodin, V. N.; Epstein, A. J. Magnetoresistance in an All-Organic-Based Spin Valve. *Adv. Mater.* **2011**, *23* (30), 3382–3386. https://doi.org/10.1002/adma.201100903.

(51) Schmidt, G.; Ferrand, D.; Molenkamp, L. W. Fundamental Obstacle for Electrical Spin Injection from a Ferromagnetic Metal into a Diffusive Semiconductor. *Phys. Rev. B* **2000**, *62* (8). https://doi.org/https://doi.org/10.1103/PhysRevB.62.R4790.

(52) Wagemans, W.; Koopmans, B. Spin Transport and Magnetoresistance in Organic Semiconductors. *Phys. Status Solidi Basic Res.* **2011**, *248* (5), 1029–1041. https://doi.org/10.1002/pssb.201046383.

(53) Coropceanu, V.; Cornil, J.; da Silva Filho, D. A.; Olivier, Y.; Silbey, R.; Brédas, J. L. Charge Transport in Organic Semiconductors. *Chem. Rev.* **2007**, *107* (4), 926–952. https://doi.org/10.1021/cr050140x.

(54) Le Guennec, P. On the Concept of Chirality. *J. Math. Chem.* **1998**, *23* (3–4), 429–439. https://doi.org/10.1023/A:1019197930712.

(55) Naaman, R.; Paltiel, Y.; Waldeck, D. H. Chiral Molecules and the Electron Spin. *Nature Reviews Chemistry*. Nature Publishing Group April 1, 2019, pp 250–260. https://doi.org/10.1038/s41570-019-0087-1.

(56) Tsymbal, E. Y.; Mryasov, O. N.; LeClair, P. R. Spin-Dependent Tunnelling in Magnetic Tunnel Junctions. *J. Phys. Condens. Matter* **2003**, *15* (4). https://doi.org/10.1088/0953-8984/15/4/201.

(57) Göhler, B.; Hamelbeck, V.; Markus, T. Z.; Kettner, M.; Hanne, G. F.; Vager, Z.; Naaman, R.; Zacharias, H. Spin Selectivity in Electron Transmission through Self-Assembled Monolayers of Double-Stranded DNA. *Science (80-.).* **2011**, *331* (6019), 894–897. https://doi.org/10.1126/science.1199339.

(58) Guo, A. M.; Sun, Q. F. Spin-Selective Transport of Electrons in DNA Double Helix. *Phys. Rev. Lett.* **2012**, *108* (21), 1–5. https://doi.org/10.1103/PhysRevLett.108.218102.

(59) Gutierrez, R.; Díaz, E.; Naaman, R.; Cuniberti, G. Spin-Selective Transport through Helical Molecular Systems. *Phys. Rev. B - Condens. Matter Mater. Phys.* **2012**, *85* (8), 2–5. https://doi.org/10.1103/PhysRevB.85.081404.

(60) Dalum, S.; Hedegård, P. Theory of Chiral Induced Spin Selectivity. *Nano Lett.* **2019**, *19* (8), 5253–5259. https://doi.org/10.1021/acs.nanolett.9b01707.

(61) Mishra, S.; Mondal, A. K.; Pal, S.; Das, T. K.; Smolinsky, E. Z. B.; Siligardi, G.; Naaman, R. Length-Dependent Electron Spin Polarization in Oligopeptides and DNA. *J. Phys. Chem. C* **2020**, acs.jpcc.0c02291. https://doi.org/10.1021/acs.jpcc.0c02291.

(62) Vajtai, R. *Springer Handbook of Nanomaterials*; Springer Berlin Heidelberg, 2013. https://doi.org/10.1007/978-3-642-20595-8.

(63) Geim, A. K. Graphene : Status and Prospects. **2009**, *324* (June), 1530–1535.

(64) Geim, A. K.; Odom, T. W.; Huang, J. L.; Kim, P.; Lieber, C. M. Atomic Structure and Electronic Properties of Single-Walled Carbon Nanotubes. *J. Phys. Chem. B* **1998**, *104* (June), 1530–1535. https://doi.org/10.1038/34145.

(65) Odom, T. W.; Huang, J. L.; Kim, P.; Lieber, C. M. Structure and Electronic Properties of Carbon Nanotubes. *J. Phys. Chem. B* **2000**, *104* (13), 2794–2809. https://doi.org/10.1021/jp993592k.

(66) Baughman, R. H.; Cui, C.; Zakhidov, A. A.; Iqbal, Z.; Barisci, J. N.; Spinks, G. M.; Wallace, G. G.; Mazzoldi, A.; De Rossi, D.; Rinzler, A. G.; Jaschinski, O.; Roth, S.; Kertesz, M. Carbon Nanotube Actuators. *Science (80-.).* **1999**, *284* (5418), 1340–1344. https://doi.org/10.1126/science.284.5418.1340.

(67) Misewich, J. A.; Martel, R.; Avouris, P.; Tsang, J. C.; Heinze, S.; Tersoff, J. Electrically Induced Optical Emission from a Carbon Nanotube FET. *Science (80-.).* **2003**, *300* (5620), 783–786. https://doi.org/10.1126/science.1081294.

(68) Wang, F.; Dukovic, G.; Brus, L. E.; Heinz, T. F. The Optical Resonances in Carbon Nanotubes Arise from Excitons. *Science (80-.).* **2005**, *308* (5723), 838–841. https://doi.org/10.1126/science.1110265.

(69) Hone, J.; Whitney, M.; Zettl, A. *Science of Fullerenes and Carbon Nanotubes*; Elsevier Sequoia SA, 1999; Vol. 103. https://doi.org/10.1016/S0379-6779(98)01070-4.

(70) Hersam, M. C. Progress towards Monodisperse Single-Walled Carbon Nanotubes. *Nat. Nanotechnol.* **2008**, *3*, 387–394.

(71) Vajtai, R. *Springer Handbook of Nanomaterials*; Vajtai, R., Ed.; Springer: Houston, TX 77005-1827 USA, 2013. https://doi.org/10.1007/978-3-642-20595-8.

(72) Donaldson, K.; Aitken, R.; Tran, L.; Stone, V.; Duffin, R.; Forrest, G.; Alexander, A. Carbon Nanotubes: A Review of Their Properties in Relation to Pulmonary Toxicology and Workplace Safety. *Toxicol. Sci.* **2006**, *92* (1), 5–22. https://doi.org/10.1093/toxsci/kfj130.

(73) Kumar, M.; Ando, Y. Chemical Vapor Deposition of Carbon Nanotubes: A Review on Growth Mechanism and Mass Production. *J. Nanosci. Nanotechnol.* **2010**, *10* (6), 3739–3758. https://doi.org/10.1166/jnn.2010.2939.

(74) Dresselhaus, M. S.; Dresselhaus, G.; Eklund, P. C. Applications of Carbon Nanostructures. *Sci. Fullerenes Carbon Nanotub.* **1996**, 870–917. https://doi.org/10.1016/b978-012221820-0/50020-4.

(75) Henrard, L.; Hernández, E.; Bernier, P.; Rubio, A. Van Der Waals Interaction in Nanotube Bundles: Consequences on Vibrational Modes. *Phys. Rev. B - Condens. Matter Mater. Phys.* **1999**, *60* (12), R8521–R8524. https://doi.org/10.1103/PhysRevB.60.R8521.

(76) Tummala, N. R.; Striolo, A. SDS Surfactants on Carbon Nanotubes: Aggregate Morphology. *ACS Nano* **2009**, *3* (3), 595–602. https://doi.org/10.1021/nn8007756.

(77) Manchado, M. A. L.; Valentini, L.; Biagiotti, J.; Kenny, J. M. Thermal and Mechanical Properties of Single-Walled Carbon Nanotubes-Polypropylene Composites Prepared by Melt Processing. *Carbon N. Y.* **2005**, *43* (7), 1499–1505. https://doi.org/10.1016/j.carbon.2005.01.031.

(78) Zheng, M.; Jagota, A.; Strano, M. S.; Santos, A. P.; Barone, P.; Chou, S. G.; Diner, B. A.; Dresselhaus, M. S.; McLean, R. S.; Onoa, G. B.; Samsonidze, G. G.; Semke, E. D.; Usrey, M.; Watts, D. J. Structure-Based Carbon Nanotube Sorting by Sequence-Dependent DNA Assembly. *Science (80-.).* **2003**, *302* (5650), 1545–1548. https://doi.org/10.1126/science.1091911.

(79) Zheng, M.; Jagota, A.; Semke, E. D.; Diner, B. A.; McLean, R. S.; Lustig, S. R.; Richardson, R. E.; Tassi, N. G. DNA-Assisted Dispersion and Separation of Carbon Nanotubes. *Nat. Mater.* **2003**, *2* (5), 338–342. https://doi.org/10.1038/nmat877.

(80) Dresselhaus, M. S.; Dresselhaus, G.; Saito, R.; Jorio, A. Raman Spectroscopy of Carbon Nanotubes. *Phys. Rep.* **2005**, *409* (2), 47–99. https://doi.org/10.1016/j.physrep.2004.10.006.

(81) Dresselhaus, M. S.; Eklund, P. C. Phonons in Carbon Nanotubes. *Adv. Phys.* **2000**, *49* (6), 705–814. https://doi.org/10.1080/000187300413184.

(82) Jorio, A.; Saito, R.; Hafner, J. H.; Lieber, C. M.; Hunter, M.; McClure, T.; Dresselhaus, G.; Dresselhaus, M. S. Structural (n, m) Determination of Isolated Single-Wall Carbon Nanotubes by Resonant Raman Scattering. *Phys. Rev. Lett.* **2001**, *86* (6), 1118–1121. https://doi.org/10.1103/PhysRevLett.86.1118.

(83) Brown, S. D. M.; Jorio, A.; Corio, P. Origin of the Breit-Wigner-Fano Lineshape of the Tangential G -Band Feature of Metallic Carbon Nanotubes. **2001**, *63*, 1–8. https://doi.org/10.1103/PhysRevB.63.155414.

(84) Kawamoto, H.; Uchida, T.; Kojima, K.; Tachibana, M.; Kawamoto, H.; Uchida, T.; Kojima, K.; Tachibana, M. The Feature of the Breit-Wigner-Fano Raman Line in DNA-Wrapped Single-Wall Carbon Nanotubes The Feature of the Breit-Wigner-Fano Raman Line in DNA-Wrapped Single-Wall Carbon Nanotubes. *J. Appl. Phys.* **2008**, *094309* (2006). https://doi.org/10.1063/1.2196249.

(85) Goldberg, B. B.; Jorio, A.; Filho, A. G. S.; Dresselhaus, G.; Dresselhaus, M. S.; Swan, A. K. G -Band Resonant Raman Study of 62 Isolated Single-Wall Carbon Nanotubes. **2002**, *65*, 23–27. https://doi.org/10.1103/PhysRevB.65.155412.

(86) Gu, H.; Zhang, X.; Wei, H.; Huang, Y.; Wei, S.; Guo, Z. An Overview of the Magnetoresistance Phenomenon in Molecular Systems. *Chem. Soc. Rev.* **2013**, *42* (13), 5907–5943. https://doi.org/10.1039/c3cs60074b.

(87) Bergmann, G. *WEAK LOCALIZATION IN THIN FILMS a Time-of-Flight Experiment with Conduction Electrons*; 1984; Vol. 107.

(88) Bergmann, G. Physical Interpretation of Weak Localization: A Time-of-Flight Experiment with Conduction Electrons. *Phys. Rev. B* **1983**, *28* (6), 2914–2920. https://doi.org/10.1103/PhysRevB.28.2914.

(89) Pichard, J.-L.; Sanquer, M.; Slevin, K.; Debray, P. *Broken Symmetries and Localization Lengths in Anderson Insulators: Theory and Experiment*; 1990; Vol. 65.

(90) Xie, Z.; Markus, T. Z.; Cohen, S. R.; Vager, Z.; Gutierrez, R.; Naaman, R. Spin Specific Electron Conduction through DNA Oligomers. *Nano Lett.* **2011**, *11* (11), 4652–4655. https://doi.org/10.1021/nl2021637.

(91) Kiran, V.; Mathew, S. P.; Cohen, S. R.; Hernández Delgado, I.; Lacour, J.; Naaman, R. Helicenes - A New Class of Organic Spin Filter. *Adv. Mater.* **2016**, *28* (10), 1957–1962. https://doi.org/10.1002/adma.201504725.

(92) Mishra, S.; Mondal, A. K.; Smolinsky, E. Z. B.; Naaman, R.; Maeda, K.; Nishimura, T.; Taniguchi, T.; Yoshida, T.; Takayama, K.; Yashima, E. Spin Filtering Along Chiral Polymers. *Angew. Chemie - Int. Ed.* **2020**, *59* (34), 14671–14676. https://doi.org/10.1002/anie.202006570.

(93) Huizi-Rayo, U.; Gutierrez, J.; Seco, J. M.; Mujica, V.; Diez-Perez, I.; Ugalde, J. M.; Tercjak, A.; Cepeda, J.; San Sebastian, E. An Ideal Spin Filter: Long-Range, High-Spin Selectivity in Chiral Helicoidal 3-Dimensional Metal Organic Frameworks. *Nano Lett.* **2020**, *20* (12), 8476–8482. https://doi.org/10.1021/acs.nanolett.0c02349.

(94) Mondal, A. K.; Brown, N.; Mishra, S.; Makam, P.; Wing, D.; Gilead, S.; Wiesenfeld, Y.; Leitus, G.; Shimon, L. J. W.; Carmieli, R.; Ehre, D.; Kamieniarz, G.; Fransson, J.; Hod, O.; Kronik, L.; Gazit, E.; Naaman, R. Long-Range Spin-Selective Transport in Chiral Metal-Organic Crystals with Temperature-Activated Magnetization. *ACS Nano* **2020**, *14* (12), 16624–16633. https://doi.org/10.1021/acsnano.0c07569.

(95) Kulkarni, C.; Mondal, A. K.; Das, T. K.; Grinbom, G.; Tassinari, F.; Mabesoone, M. F. J.; Meijer, E. W.; Naaman, R. Highly Efficient and Tunable Filtering of Electrons' Spin by Supramolecular Chirality of Nanofiber-Based Materials. *Adv. Mater.* **2020**, *32* (7). https://doi.org/10.1002/adma.201904965.

(96) Iliafar, S.; Mittal, J.; Vezenov, D.; Jagota, A. Interaction of Single-Stranded DNA with Curved Carbon Nanotube Is Much Stronger than with Flat Graphite. *J. Am. Chem. Soc.* **2014**, *136* (37), 12947–12957. https://doi.org/10.1021/ja5055498.

(97) Roy, S.; Vedala, H.; Roy, A. D.; Kim, D. H.; Doud, M.; Mathee, K.; Shin, H. K.; Shimamoto, N.; Prasad, V.; Choi, W. Direct Electrical Measurements on Single-Molecule Genomic DNA Using Single-Walled Carbon Nanotubes. *Nano Lett.* **2008**, *8* (1), 26–30. https://doi.org/10.1021/nl0716451.

(98) WATSON, J. D.; CRICK, F. H. C. Molecular Structure of Nucleic Acids: A Structure for Deoxyribose Nucleic Acid. *Nature* **1953**, *171* (4356), 737–738. https://doi.org/10.1038/171737a0.

(99) Dalum, S.; Hedegård, P. Theory of Chiral Induced Spin Selectivity. *Nano Lett.* **2019**, *19* (8), 5253–5259. https://doi.org/10.1021/acs.nanolett.9b01707.

(100) Yarotski, D. A.; Kilina, S. V.; Talin, A. A.; Tretiak, S.; Prezhdo, O. V.; Balatsky, A. V.; Taylor, A. J. Scanning Tunneling Microscopy of DNA-Wrapped Carbon Nanotubes. *Nano Lett.* **2009**, *9* (1), 12–17. https://doi.org/10.1021/nl801455t.

(101) Li, W.; O'Brien-Simpson, N. M.; Hossain, M. A.; Wade, J. D. The 9-Fluorenylmethoxycarbonyl (Fmoc) Group in Chemical Peptide Synthesis-Its Past, Present, and Future. *Aust. J. Chem.* **2020**, *73* (4), 271–276. https://doi.org/10.1071/CH19427.

(102) Vijay, R.; Polavarapu, P. L. FMOC-Amino Acid Surfactants: Discovery, Characterization and Chiroptical Spectroscopy. *J. Phys. Chem. A* **2012**, *116* (44), 10759–10769. https://doi.org/10.1021/jp308134m.

(103) Xing, P.; Chu, X.; Li, S.; Ma, M.; Hao, A. Hybrid Gels Assembled from Fmoc-Amino Acid and Graphene Oxide with Controllable Properties. *ChemPhysChem* **2014**, *15* (11), 2377–2385. https://doi.org/10.1002/cphc.201402018.

(104) Adhikari, B.; Nanda, J.; Banerjee, A. Pyrene-Containing Peptide-Based Fluorescent Organogels: Inclusion of Graphene into the Organogel. *Chem. - A Eur. J.* **2011**, *17* (41), 11488–11496. https://doi.org/10.1002/chem.201101360.

(105) Pender, M. J.; Sowards, L. A.; Hartgerink, J. D.; Stone, M. O.; Naik, R. R. Peptide-Mediated Formation of Single-Wall Carbon Nanotube Composites. *Nano Lett.* **2006**, *6* (1), 40–44. https://doi.org/10.1021/nl051899r.

(106) Valenti, L. E.; Fiorito, P. A.; García, C. D.; Giacomelli, C. E. The Adsorption-Desorption Process of Bovine Serum Albumin on Carbon Nanotubes. *J. Colloid Interface Sci.* **2007**, *307* (2), 349–356. https://doi.org/10.1016/j.jcis.2006.11.046.

(107) Liu, S.; Cai, C. Immobilization and Characterization of Alcohol Dehydrogenase on Single-Walled Carbon Nanotubes and Its Application in Sensing Ethanol. *J. Electroanal. Chem.* **2007**, *602* (1), 103–114. https://doi.org/10.1016/j.jelechem.2006.12.003.

(108) Cousins, B. G.; Das, A. K.; Sharma, R.; Li, Y.; McNamara, J. P.; Hillier, I. H.; Kinloch, I. A.; Ulijn, R. V. Enzyme-Activated Surfactants for Dispersion of Carbon Nanotubes. *Small* **2009**, *5* (5), 587–590. https://doi.org/10.1002/smll.200801184.

(109) Roy, S.; Banerjee, A. Functionalized Single Walled Carbon Nanotube Containing Amino Acid Based Hydrogel: A Hybrid Nanomaterial. *RSC Adv.* **2012**, *2* (5), 2105–2111. https://doi.org/10.1039/c2ra00763k.

(110) Contreras-Montoya, R.; Escolano, G.; Roy, S.; Lopez-Lopez, M. T.; Delgado-López, J. M.; Cuerva, J. M.; Díaz-Mochón, J. J.; Ashkenasy, N.; Gavira, J. A.; Álvarez de Cienfuegos, L. Catalytic and Electron Conducting Carbon Nanotube–Reinforced Lysozyme Crystals. *Adv. Funct. Mater.* **2019**, *29* (5). https://doi.org/10.1002/adfm.201807351.

(111) Jayawarna, V.; Ali, M.; Jowitt, T. A.; Miller, A. F.; Saiani, A.; Gough, J. E.; Ulijn, R. V. Nanostructured Hydrogels for Three-Dimensional Cell Culture through Self-Assembly of Fluorenylmethoxycarbonyl-Dipeptides. *Adv. Mater.* **2006**, *18* (5), 611–614. https://doi.org/10.1002/adma.200501522.

(112) Mahler, A.; Reches, M.; Rechter, M.; Cohen, S.; Gazit, E. Rigid, Self-Assembled Hydrogel Composed of a Modified Aromatic Dipeptide. *Adv. Mater.* **2006**, *18* (11), 1365–1370. https://doi.org/10.1002/adma.200501765.

(113) Tao, K.; Levin, A.; Adler-Abramovich, L.; Gazit, E. Fmoc-Modified Amino Acids and Short Peptides: Simple Bio-Inspired Building Blocks for the Fabrication of Functional Materials. *Chem. Soc. Rev.* **2016**, *45* (14), 3935–3953. https://doi.org/10.1039/c5cs00889a.

(114) Fleming, S.; Ulijn, R. V. Design of Nanostructures Based on Aromatic Peptide Amphiphiles. *Chem. Soc. Rev.* **2014**, *43* (23), 8150–8177. https://doi.org/10.1039/c4cs00247d.

(115) Charalambidis, G.; Georgilis, E.; Panda, M. K.; Anson, C. E.; Powell, A. K.; Doyle, S.; Moss, D.; Jochum, T.; Horton, P. N.; Coles, S. J.; Linares, M.; Beljonne, D.; Naubron, J. V.; Conradt, J.; Kalt, H.; Mitraki, A.; Coutsolelos, A. G.; Balaban, T. S. A Switchable Self-Assembling and Disassembling Chiral System Based on a Porphyrin-Substituted Phenylalanine-Phenylalanine Motif. *Nat. Commun.* **2016**, *7*. https://doi.org/10.1038/ncomms12657.

(116) Zhu, H. *Organic Stereochemistry*; Wiley-VCH Verlag GmbH & Co. KGaA: Weinheim, Germany, 2015. https://doi.org/10.1002/9783527688166.

(117) Dybowska, B. E.; Fujio, Y. Optical Analysis of Glucono-δ-Lactone Induced Soy Protein Gelation. *Journal of Food Engineering*. 1998, pp 123–133. https://doi.org/10.1016/s0260-8774(98)00039-9.

(118) Hsia, S. Y.; Hsiao, Y. H.; Li, W. T.; Hsieh, J. F. Aggregation of Soy Protein-Isoflavone Complexes and Gel Formation Induced by Glucono-Î-Lactone in Soymilk. *Sci. Rep.* **2016**, *6* (October), 1–10. https://doi.org/10.1038/srep35718.

(119) Tsutsumi, N.; Oya, M.; Sakai, W. Biodegradable Network Polyesters from Gluconolactone and Citric Acid. *Macromolecules* **2004**, *37* (16), 5971–5976. https://doi.org/10.1021/ma049607g.

(120) Garésio, F.; Kardos, N.; Bonnevie, C.; Petit, S.; Luche, J. L. D-Gluconolactone: As a Precursor to New Environmentally Benign Tensioactive Agents. *Green Chem.* **2000**, *2* (1), 33–36. https://doi.org/10.1039/a908605f.

(121) Pocker, Y.; Green, E. Hydrolysis of D-Glucono-δ-Lactone. I. General Acid—Base Catalysis, Solvent Deuterium Isotope Effects, and Transition State Characterization. *J. Am. Chem. Soc.* **1973**, *95* (1), 113–119. https://doi.org/10.1021/ja00782a019.

(122) National Center for Biotechnology Information (2021). PubChem Compound Summary for CID 7027, Gluconolactone. Retrieved November 6, 2021 from https://pubchem.ncbi.nlm.nih.gov/compound/Gluconolactone.

(123) Arakawa, H.; Takeda, K.; Higashi, S. L.; Shibata, A.; Kitamura, Y.; Ikeda, M. Self-Assembly and Hydrogel Formation Ability of Fmoc-Dipeptides Comprising α-Methyl-L-Phenylalanine. *Polym. J.* **2020**, *52* (8), 923–930. https://doi.org/10.1038/s41428-019-0301-5.

(124) Zhang, Y.; Gu, H.; Yang, Z.; Xu, B. Supramolecular Hydrogels Respond to Ligand-Receptor Interaction. *J. Am. Chem. Soc.* **2003**, *125* (45), 13680–13681. https://doi.org/10.1021/ja036817k.

(125) Dasgupta, A.; Mondal, J. H.; Das, D. Peptide Hydrogels. *RSC Adv.* **2013**, *3* (24), 9117–9149. https://doi.org/10.1039/c3ra40234g.

(126) Ryan, K.; Beirne, J.; Redmond, G.; Kilpatrick, J. I.; Guyonnet, J.; Buchete, N. V.; Kholkin, A. L.; Rodriguez, B. J. Nanoscale Piezoelectric Properties of Self-Assembled Fmoc-FF Peptide Fibrous Networks. *ACS Appl. Mater. Interfaces* **2015**, *7* (23), 12702–12707. https://doi.org/10.1021/acsami.5b01251.

(127) Nepal, D.; Geckeler, K. E. PH-Sensitive Dispersion and Debundling of Single-Walled Carbon Nanotubes: Lysozyme as a Tool. *Small* **2006**, *2* (3), 406–412. https://doi.org/10.1002/smll.200500351.

(128) Nepal, D.; Balasubramanian, S.; Simonian, A. L.; Davis, V. A. Strong Antimicrobial Coatings: Single-Walled Carbon Nanotubes Armored with Biopolymers. *Nano Lett.* **2008**, *8* (7), 1896–1901. https://doi.org/10.1021/nl080522t.

(129) Swaminathan, R.; Ravi, V. K.; Kumar, S.; Kumar, M. V. S.; Chandra, N. *Lysozyme: A Model Protein for Amyloid Research*; 2011; Vol. 84. https://doi.org/10.1016/B978-0-12-386483-3.00003-3.

(130) Horn, D. W.; Tracy, K.; Easley, C. J.; Davis, V. A. Lysozyme Dispersed Single-Walled Carbon Nanotubes: Interaction and Activity. *J. Phys. Chem. C* **2012**, *116* (18), 10341–10348. https://doi.org/10.1021/jp300242a.

(131) Bomboi, F.; Bonincontro, A.; La Mesa, C.; Tardani, F. Interactions between Single-Walled Carbon Nanotubes and Lysozyme. *J. Colloid Interface Sci.* **2011**, *355* (2), 342–347. https://doi.org/10.1016/j.jcis.2010.12.026.

(132) Bomboi, F.; Tardani, F.; Gazzoli, D.; Bonincontro, A.; La Mesa, C. Lysozyme Binds onto Functionalized Carbon Nanotubes. *Colloids Surfaces B Biointerfaces* **2013**, *108*, 16–22. https://doi.org/10.1016/j.colsurfb.2013.02.034.

(133) Nie, H.; Wang, H.; Cao, A.; Shi, Z.; Yang, S. T.; Yuan, Y.; Liu, Y. Diameter-Selective Dispersion of Double-Walled Carbon Nanotubes by Lysozyme. *Nanoscale* **2011**, *3* (3), 970–973. https://doi.org/10.1039/c0nr00831a.

(134) Ding, Y.; Shi, L.; Wei, H. Protein-Directed Approaches to Functional Nanomaterials: A Case Study of Lysozyme. *J. Mater. Chem. B* **2014**, *2* (47), 8268–8291. https://doi.org/10.1039/c4tb01235f.

(135) Contreras-Montoya, R.; Escolano, G.; Roy, S.; Lopez-Lopez, M. T.; Delgado-López, J. M.; Cuerva, J. M.; Díaz-Mochón, J. J.; Ashkenasy, N.; Gavira, J. A.; Álvarez de Cienfuegos, L. Catalytic and Electron Conducting Carbon Nanotube–Reinforced Lysozyme Crystals. *Adv. Funct. Mater.* **2019**, *29* (5), 1–10. https://doi.org/10.1002/adfm.201807351.

(136) Kettner, M.; Göhler, B.; Zacharias, H.; Mishra, D.; Kiran, V.; Naaman, R.; Fontanesi, C.; Waldeck, D. H.; Sek, S.; Pawowski, J.; Juhaniewicz, J. Spin Filtering in Electron Transport Through Chiral Oligopeptides. *J. Phys. Chem. C* **2015**, *119* (26), 14542–14547. https://doi.org/10.1021/jp509974z.

(137) Rahman, M. W.; Alam, K.; Pramanik, S. Long Carbon Nanotubes Functionalized with DNA and Implications for Spintronics. *ACS Omega 3* (12), 17108–17115. https://doi.org/10.1021/acsomega.8b02237.

(138) Rahman, M. W.; Firouzeh, S.; Mujica, V.; Pramanik, S. Carrier Transport Engineering in Carbon Nanotubes by Chirality-Induced Spin Polarization. *ACS Nano 14* (3), 3389–3396. https://doi.org/10.1021/acsnano.9b09267.

(139) Rahman, M. W.; Firouzeh, S.; Pramanik, S. Carrier Localization and Magnetoresistance in DNA-Functionalized Carbon Nanotubes. *Nanotechnology* **2021**, *32* (45). https://doi.org/10.1088/1361-6528/ac18d9.

(140) Rahman, M. W.; Mañas-Torres, M. C.; Firouzeh, S.; Cuerva, J. M.; Álvarez de Cienfuegos, L.; Pramanik, S. Molecular Functionalization and Emergence of Long-Range Spin-Dependent Phenomena in Two-Dimensional Carbon Nanotube Networks. *ACS Nano* **2021**, acsnano.1c07739. https://doi.org/10.1021/acsnano.1c07739.

(141) Naaman, R.; Waldeck, D. H. Comment on "Spin-Dependent Electron Transmission Model for Chiral Molecules in Mesoscopic Devices." *Phys. Rev. B* **2020**, *101* (2), 3–5. https://doi.org/10.1103/PhysRevB.101.026403.

(142) Bandyopadhyay, S.; Cahay, M. Electron Spin for Classical Information Processing: A Brief Survey of Spin-Based Logic Devices, Gates and Circuits. *Nanotechnology* **2009**, *20* (41). https://doi.org/10.1088/0957-4484/20/41/412001.

(143) Gangoli, V. S.; Godwin, M. A.; Reddy, G.; Bradley, R. K.; Barron, A. R. The State of HiPco Single-Walled Carbon Nanotubes in 2019. *C — J. Carbon Res.* **2019**, *5* (4), 65. https://doi.org/10.3390/c5040065.

(144) Fujigaya, T.; Nakashima, N. Non-Covalent Polymer Wrapping of Carbon Nanotubes and the Role of Wrapped Polymers

as Functional Dispersants. *Sci. Technol. Adv. Mater.* **2015**, *16* (2). https://doi.org/10.1088/1468-6996/16/2/024802.

(145) Gao, C.; Guo, Z.; Liu, J. H.; Huang, X. J. The New Age of Carbon Nanotubes: An Updated Review of Functionalized Carbon Nanotubes in Electrochemical Sensors. *Nanoscale* **2012**, *4* (6), 1948–1963. https://doi.org/10.1039/c2nr11757f.

(146) Tu, X.; Zheng, M. A DNA-Based Approach to the Carbon Nanotube Sorting Problem. *Nano Res.* **2008**, *1* (3), 185–194. https://doi.org/10.1007/s12274-008-8022-7.

(147) Sanchez-Pomales, G.; Pagan-Miranda, C.; Santiago-Rodriguez, L.; R., C. DNA-Wrapped Carbon Nanotubes: From Synthesis to Applications. *Carbon Nanotub.* **2010**, 721–749. https://doi.org/10.5772/39450.

(148) Haggenmueller, R.; Rahatekar, S. S.; Fagan, J. A.; Chun, J.; Becker, M. L.; Naik, R. R.; Krauss, T.; Carlson, L.; Kadla, J. F.; Trulove, P. C.; Fox, D. F.; DeLong, H. C.; Fang, Z.; Kelley, S. O.; Gilrnan, J. W. Comparison of the Quality of Aqueous Dispersions of Single Wall Carbon Nanotubes Using Surfactants and Biomolecules. *Langmuir* **2008**, *24* (9), 5070–5078. https://doi.org/10.1021/la703008r.

(149) Hughes, J. M.; Cathcart, H.; Coleman, J. N. Dispersion and Exfoliation of Nanotubes with Synthetic Oligonucleotides: Variation of Dispersion Efficiency and Oligo-Nanotube Interaction with Base Type. *J. Phys. Chem. C* **2010**, *114* (27), 11741–11747. https://doi.org/10.1021/jp101834t.

(150) Mayo, M. L.; Chen, Z. Q.; Kilina, S. V. Computational Studies of Nucleotide Selectivity in DNA-Carbon Nanotube Hybrids. *J. Phys. Chem. Lett.* **2012**, *3* (19), 2790–2797. https://doi.org/10.1021/jz3011145.

(151) Lahiji, R. R.; Dolash, B. D.; Bergstrom, D. E.; Reifenberger, R. Oligodeoxyribonucleotide Association with Single-Walled Carbon Nanotubes Studied by SPM. *Small* **2007**, *47907* (11), 1912–1920. https://doi.org/10.1002/smll.200700184.

(152) Mclean, R. S.; Huang, X.; Khripin, C.; Jagota, A.; Zheng, M. Controlled Two-Dimensional Pattern of Spontaneously Aligned Carbon Nanotubes. *Nano Lett.* **2006**, *6* (1), 55–60. https://doi.org/10.1021/nl051952b.

(153) Gigliotti, B.; Sakizzie, B.; Bethune, D. S.; Shelby, R. M.; Cha, J. N. Sequence-Independent Helical Wrapping of Single-Walled Carbon Nanotubes by Long Genomic DNA. *Nano Lett.* **2006**, *6* (2), 159–164. https://doi.org/10.1021/nl0518775.

(154) Barisci, J. N.; Tahhan, M.; Wallace, G. G.; Badaire, S.; Vaugien, T.; Maugey, M.; Poulin, P. Properties of Carbon Nanotube Fibers Spun from DNA-Stabilized Dispersions. *Adv. Funct. Mater.* **2004**, *14* (2), 133–138. https://doi.org/10.1002/adfm.200304500.

(155) Cathcart, H.; Quinn, S.; Nicolosi, V.; Kelly, J. M.; Blau, W. J.; Coleman, J. N. Spontaneous Debundling of Single-Walled Carbon Nanotubes in DNA-Based Dispersions. *J. Phys. Chem. C* **2007**, *111* (1), 66–74. https://doi.org/10.1021/jp065503r.

(156) Cathcart, H.; Nicolosi, V.; Hughes, J. M.; Blau, W. J.; Kelly, J. M.; Quinn, S. J.; Coleman, J. N. Ordered DNA Wrapping Switches on Luminescence in Single-Walled Nanotube Dispersions. *J. Am. Chem. Soc.* **2008**, *130* (38), 12734–12744. https://doi.org/10.1021/ja803273s.

(157) Vogel, S. R.; Kappes, M. M.; Hennrich, F.; Richert, C. An Unexpected New Optimum in the Structure Space of DNA Solubilizing Single-Walled Carbon Nanotubes. *Chem. - A Eur. J.* **2007**, *13* (6), 1815–1820. https://doi.org/10.1002/chem.200600988.

(158) Vogel, S. R.; Müller, K.; Plutowski, U.; Kappes, M. M.; Richert, C. DNA-Carbon Nanotube Interactions and Nanostructuring Based on DNA. *Phys. Status Solidi Basic Res.* **2007**, *244* (11), 4026–4029. https://doi.org/10.1002/pssb.200776108.

(159) Xu, Y.; Pehrsson, P. E.; Chen, L.; Zhang, R.; Zhao, W. Double-Stranded DNA Single-Walled Carbon Nanotube Hybrids for Optical Hydrogen Peroxide and Glucose Sensing. *J. Phys. Chem. C* **2007**, *111* (24), 8638–8643. https://doi.org/10.1021/jp0709611.

(160) Yang, Q.; Wang, Q.; Gale, N.; Oton, C. J.; Cui, L.; Nandhakumar, I. S.; Zhu, Z.; Tang, Z. Loosening the DNA Wrapping around Single-Walled Carbon Nanotubes by Increasing the Strand Length. **2009**. https://doi.org/10.1088/0957-4484/20/19/195603.

(161) Kawamoto, H.; Uchida, T.; Kojima, K.; Tachibana, M. G Band Raman Features of DNA-Wrapped Single-Wall Carbon Nanotubes in Aqueous Solution and Air. *Chem. Phys. Lett.* **2006**, *432*, 172–176. https://doi.org/10.1016/j.cplett.2006.10.019.

(162) Talin, A. A.; Dentinger, P. M.; Jones, F. E.; Pathak, S.; Hunter, L.; Léonard, F.; Morales, A. M. Assembly and Electrical Characterization of DMA-Wrapped Carbon Nanotube Devices. *J. Vac. Sci. Technol. B Microelectron. Nanom. Struct.* **2004**, *22* (6), 3107–3111. https://doi.org/10.1116/1.1815304.

(163) Lewenstein, J. C.; Burgin, T. P.; Ribayrol, A.; Nagahara, L. A.; Tsui, R. K. High-Yield Selective Placement of Carbon

Nanotubes on Pre-Patterned Electrodes. *Nano Lett.* **2002**, *2* (5), 443–446. https://doi.org/10.1021/nl015690z.

(164) Bockrath, M.; Cobden, D. H.; McEuen, P. L.; Chopra, N. G.; Zettl, A.; Thess, A.; Smalley, R. E. Single-Electron Transport in Ropes of Carbon Nanotubes. *Science (80-.).* **1997**, *275* (5308), 1922–1925. https://doi.org/10.1126/science.275.5308.1922.

(165) Porath, D.; Bezryadin, A.; Vries, S. De; Dekker, C. Direct Measurement of Electrical Transport through DNA Molecules. *Nature* **2000**, *403* (February), 635–638. https://doi.org/10.1038/35001029.

(166) Storm, A. J.; Van Noort, J.; De Vries, S.; Dekker, C. Insulating Behavior for DNA Molecules between Nanoelectrodes at the 100 Nm Length Scale. *Appl. Phys. Lett.* **2001**, *79* (23), 3881–3883. https://doi.org/10.1063/1.1421086.

(167) Dekker, G.; Ratner, M. A. Electronic Properties of DNA. *Phys. World* **2001**, *14* (8), 29–33. https://doi.org/10.1088/2058-7058/14/8/33.

(168) Johnson, R. R. Probing the Structure of DNA-Carbon Nanotube Hybrids with Molecular Dynamics. *Nano Lett.* **2008**, *8* (1), 69–75. https://doi.org/10.1021/nl071909j.

(169) Johnson, R. R.; Charlie Johnson, A. T.; Klein, M. L. The Nature of DNA-Base-Carbon-Nanotube Interactions. *Small* **2010**, *6* (1), 31–34. https://doi.org/10.1002/smll.200901481.

(170) Gowtham, S.; Scheicher, R. H.; Pandey, R.; Karna, S. P.; Ahuja, R. First-Principles Study of Physisorption of Nucleic Acid Bases on Small-Diameter Carbon Nanotubes. *Nanotechnology* **2008**, *19* (12). https://doi.org/10.1088/0957-4484/19/12/125701.

(171) Johnson, R. R. Free Energy Landscape of a DNA-Carbon Nanotube Hybrid Using Replica Exchange Molecular Dynamics. *Nano Lett.* **2009**, *9* (2), 537–541. https://doi.org/10.1021/nl802645d.

(172) Das, A.; Sood, A. K.; Maiti, P. K.; Das, M.; Varadarajan, R.; Rao, C. N. R. Binding of Nucleobases with Single-Walled Carbon Nanotubes: Theory and Experiment. *Chem. Phys. Lett.* **2008**, *453* (4–6), 266–273. https://doi.org/10.1016/j.cplett.2008.01.057.

(173) Kawamoto, H.; Uchida, T.; Kojima, K.; Tachibana, M. G Band Raman Features of DNA-Wrapped Single-Wall Carbon Nanotubes in Aqueous Solution and Air. *Chem. Phys. Lett.* **2006**, *432* (1–3), 172–176. https://doi.org/10.1016/j.cplett.2006.10.019.

(174) Karachevtsev, V. A.; Glamazda, A. Y. Raman Spectroscopy of DNA-Wrapped Single-Walled Carbon Nanotube Films at 295 and 5K. *Low Temp. Phys.* **2010**, *36* (5), 373–381. https://doi.org/10.1063/1.3432244.

(175) Stepanian, S. G.; Karachevtsev, M. V.; Glamazda, A. Y.; Karachevtsev, V. A.; Adamowicz, L. Raman Spectroscopy Study and First-Principles Calculations of the Interaction between Nucleic Acid Bases and Carbon Nanotubes. *J. Phys. Chem. A* **2009**, *113* (15), 3621–3629. https://doi.org/10.1021/jp810205a.

(176) Karachevtsev, V. A.; Glamazda, A. Y.; Dettlaff-Weglikowska, U.; Leontiev, V. S.; Mateichenko, P. V.; Roth, S.; Rao, A. M. Spectroscopic and SEM Studies of SWNTs: Polymer Solutions and Films. *Carbon N. Y.* **2006**, *44* (7), 1292–1297. https://doi.org/10.1016/j.carbon.2005.08.008.

(177) Ioffe, L. B.; Spivak, B. Z. Giant Magnetoresistance in the Variable-Range Hopping Regime. *J. Exp. Theor. Phys.* **2013**, *117* (3), 551–569. https://doi.org/10.1134/S1063776113110101.

(178) Tang, Z. K.; Sun, H. D.; Wang, J. Electrical Transport Properties of Mono-Dispersed Single-Wall Carbon Nanotubes Formed in Channels of Zeolite Crystal. *Phys. B Condens. Matter* **2000**, *279* (1–3), 200–203. https://doi.org/10.1016/S0921-4526(99)00734-6.

(179) Kim, G. T.; Choi, E. S.; Kim, D. C.; Suh, D. S.; Park, Y. W. Magnetoresistance of an Entangled Single-Wall Carbon-Nanotube Network. *Phys. Rev. B* **1998**, *58* (24), 64–69. https://doi.org/https://doi.org/10.1103/PhysRevB.58.16064.

(180) Jaiswal, M.; Wang, W.; Fernando, K. A. S.; Sun, Y. P.; Menon, R. Magnetotransport in Transparent Single-Wall Carbon Nanotube Networks. *Phys. Rev. B - Condens. Matter Mater. Phys.* **2007**, *76* (11), 2–5. https://doi.org/10.1103/PhysRevB.76.113401.

(181) Yang, X.; Van Der Wal, C. H.; Van Wees, B. J. Spin-Dependent Electron Transmission Model for Chiral Molecules in Mesoscopic Devices. *Phys. Rev. B* **2019**, *99* (2), 1–16. https://doi.org/10.1103/PhysRevB.99.024418.

(182) Pichard, J. L.; Sanquer, M.; Slevin, K.; Debray, P. Broken Symmetries and Localization Lengths in Anderson Insulators: Theory and Experiment. *Phys. Rev. Lett.* **1990**, *65* (14), 1812–1815. https://doi.org/10.1103/PhysRevLett.65.1812.

(183) Nguen, V. L.; Spivak, B. Z.; Shklovskii, B. I. Tunnel Hopping in Disordered Systems. *Sov. Phys. JETP* **1985**, *62* (5), 1021–1029.

(184) Raikh, M. E.; Wessels, G. F. Single-Scattering-Path Approach to the Negative Magnetoresistance in the Variable-Range-Hopping Regime for Two-Dimensional Electron Systems. *Phys. Rev. B* **1993**, *47* (23), 15609–15621. https://doi.org/10.1103/PhysRevB.47.15609.

(185) Yazawa, K. Negative Magneto-Resistance in Pyrolytic Carbons. *J. Phys. Soc. Japan* **1969**, *26* (6), 1407–1419. https://doi.org/10.1143/JPSJ.26.1407.

(186) Fukuyama, H.; Yosida, K. Negative Magnetoresistance in the Anderson Localized States. II. Effect of Electron Correlations. *J. Phys. Soc. Japan* **1979**, *46* (5), 1522–1528. https://doi.org/10.1143/JPSJ.46.1522.

(187) Hueso, L. E.; Pruneda, J. M.; Ferrari, V.; Burnell, G.; Valdés-Herrera, J. P.; Simons, B. D.; Littlewood, P. B.; Artacho, E.; Fert, A.; Mathur, N. D. Transformation of Spin Information into Large Electrical Signals Using Carbon Nanotubes. *Nature* **2007**, *445* (7126), 410–413. https://doi.org/10.1038/nature05507.

(188) Gogolin, A. A.; Mel'Nikov, V. I.; Rashba, É. I. Conductivity in a Disordered One-Dimensional System Induced by Electron-Phonon Interaction. *Sov. Phys. JETP* **1976**, *42* (1), 168.

(189) Yang, X.; Van Der Wal, C. H.; Van Wees, B. J. Detecting Chirality in Two-Terminal Electronic Nanodevices. *Nano Lett.* **2020**, *20* (8), 6148–6154. https://doi.org/10.1021/acs.nanolett.0c02417.

(190) Sánchez-Pomales, G.; Santiago-Rodríguez, L.; Cabrera, C. R. DNA-Functionalized Carbon Nanotubes for Biosensing Applications. *Journal of Nanoscience and Nanotechnology*. April 2009, pp 2175–2188. https://doi.org/10.1166/jnn.2009.SE47.

(191) Baumgartner, G.; Carrard, M.; Zuppiroli, L.; Bacsa, W.; De Heer, W. A.; Forró, L. *PHYSICAL REVIEW B 15 MARCH 1997-I VOLUME*; 1997; Vol. 55.

(192) Ghanbari, R.; Ghorbani, S. R.; Arabi, H.; Foroughi, J. Magnetoresistance Mechanisms in Carbon-Nanotube Yarns. *Synth. Met.* **2018**, *242*, 55–60. https://doi.org/10.1016/j.synthmet.2018.04.007.

(193) Kaiser, A.; Düsberg, G.; Roth, S. Heterogeneous Model for Conduction in Carbon Nanotubes. *Phys. Rev. B - Condens. Matter Mater. Phys.* **1998**, *57* (3), 1418–1421. https://doi.org/10.1103/PhysRevB.57.1418.

(194) Yanagi, K.; Udoguchi, H.; Sagitani, S.; Oshima, Y.; Takenobu, T. Transport Mechanisms in Metallic and Semiconducting Single-Wall Carbon. **2010**, *4* (7), 4027–4032.

(195) Perlitz, Y.; Michaeli, K. Helical Liquid in Carbon Nanotubes Wrapped with DNA Molecules. *Phys. Rev. B* **2018**, *98* (19). https://doi.org/10.1103/PhysRevB.98.195405.

(196) Duan, W. H.; Wang, Q.; Collins, F. Dispersion of Carbon Nanotubes with SDS Surfactants: A Study from a Binding Energy Perspective. *Chem. Sci.* **2011**, *2* (7), 1407–1413. https://doi.org/10.1039/c0sc00616e.

(197) Ioffe, L. B.; Spivak, B. Z. Giant Magnetoresistance in the Variable-Range Hopping Regime. *J. Exp. Theor. Phys.* **2013**, *117* (3), 551–569. https://doi.org/10.1134/S1063776113110101.

(198) Kim, G. T.; Choi, E. S.; Kim, D. C.; Suh, D. S.; Park, Y. W.; Liu, K.; Duesberg, G.; Roth, S. *Magnetoresistance of an Entangled Single-Wall Carbon-Nanotube Network*.

(199) Bergmann, G. *Physical Interpretation of Weak Localization: A Time-of-Fiight Experiment with Conduction Electrons*; 1983; Vol. 28.

(200) Nguen, V. L.; Spivak, B. Z.; Shklovskii, B. I. Tunnel Hopping in Disordered Systems. *J. Exp. Theor. Phys.* **1985**, *89* (5), 1770–1784.

(201) Schirmacher, W.; De-Partment E13, P. *Quantum-Interference Magnetoconductivity in the Variable-Range-Hopping Regime*; 1990; Vol. 41.

(202) Sivan, U.; Entin-Wohlman, O.; Aviv, T.; Imry, Y. *Orbital Magnetoconductance in the Variable-Range-Hopping Regime*; 1988; Vol. 60.

(203) Lerner, I. V.; Imry, Y. Magnetic-Field Dependence of the Localization Length in Anderson Insulators. *Epl* **1995**, *29* (1), 49–54. https://doi.org/10.1209/0295-5075/29/1/009.

(204) Zhu, H.; Yi, J.; Li, M. Y.; Xiao, J.; Zhang, L.; Yang, C. W.; Kaindl, R. A.; Li, L. J.; Wang, Y.; Zhang, X. Observation of Chiral Phonons. *Science (80-.).* **2018**, *359* (6375), 579–582. https://doi.org/10.1126/science.aar2711.

(205) Wu, Y.; Zhao, X.; Shang, Y.; Chang, S.; Dai, L.; Cao, A. Application-Driven Carbon Nanotube Functional Materials. *ACS Nano* **2021**, *15* (5), 7946–7974. https://doi.org/10.1021/acsnano.0c10662.

(206) Marchesan, S.; Melchionna, M.; Prato, M. Wire Up on Carbon Nanostructures! How To Play a Winning Game. *ACS Nano* **2015**, *9* (10), 9441–9450. https://doi.org/10.1021/acsnano.5b04956.

(207) Iglesias, D.; Melle-Franco, M.; Kurbasic, M.; Melchionna, M.; Abrami, M.; Grassi, M.; Prato, M.; Marchesan, S. Oxidized Nanocarbons-Tripeptide Supramolecular Hydrogels: Shape Matters! *ACS Nano* **2018**, *12* (6), 5530–5538. https://doi.org/10.1021/acsnano.8b01182.

(208) Adorinni, S.; Rozhin, P.; Marchesan, S. Smart Hydrogels Meet Carbon Nanomaterials for New Frontiers in Medicine. *Biomedicines* **2021**, *9* (5), 1–22. https://doi.org/10.3390/biomedicines9050570.

(209) Rozhin, P.; Charitidis, C.; Marchesan, S. Self-Assembling Peptides and Carbon Nanomaterials Join Forces for Innovative Biomedical Applications. *Molecules* **2021**, *26* (13). https://doi.org/10.3390/molecules26134084.

(210) Cottet, A.; Kontos, T.; Sahoo, S.; Man, H. T.; Choi, M. S.; Belzig, W.; Bruder, C.; Morpurgo, A. F.; Schönenberger, C. Nanospintronics with Carbon Nanotubes. *Semicond. Sci. Technol.* **2006**, *21* (11). https://doi.org/10.1088/0268-1242/21/11/S11.

(211) Zhang, Y.; Guo, L.; Zhu, X.; Sun, X. The Application of Organic Semiconductor Materials in Spintronics. *Frontiers in Chemistry*. Frontiers Media S.A. October 22, 2020. https://doi.org/10.3389/fchem.2020.589207.

(212) Waldeck, D. H.; Naaman, R.; Paltiel, Y. The Spin Selectivity Effect in Chiral Materials. *APL Mater.* **2021**, *9* (4). https://doi.org/10.1063/5.0049150.

(213) Aiello, C. D.; Abbas, M.; Abendroth, J.; Banerjee, A. S.; Beratan, D.; Belling, J.; Berche, B.; Botana, A.; Caram, J. R.; Celardo, L.; Cuniberti, G.; Dianat, A.; Guo, Y.; Gutierrez, R.; Herrmann, C.; Hihath, J.; Kale, S.; Kurian, P.; Lai, Y.-C.; Medina, E.; Mujica, V.; Naaman, R.; Noormandipour, M.; Palma, J.; Paltiel, Y.; Petuskey, W.; Ribeiro-Silva, J. C.; Stemer, D.; Valdes-Curiel, A.; Varela, S.; Waldeck, D.; Weiss, P. S.; Zacharias, H.; Wang, Q. H. A Chirality-Based Quantum Leap: A Forward-Looking Review. **2020**.

(214) Naaman, R.; Paltiel, Y.; Waldeck, D. H. Chiral Molecules and the Electron Spin. *Nat. Rev. Chem.* **2019**, *3* (4), 250–260. https://doi.org/10.1038/s41570-019-0087-1.

(215) Tournus, F.; Latil, S.; Heggie, M. I.; Charlier, J.-C. <math Display="inline"> <mi>π</Mi> </Math> -Stacking Interaction between Carbon Nanotubes and Organic Molecules. *Phys. Rev. B* **2005**, *72* (7), 075431. https://doi.org/10.1103/PhysRevB.72.075431.

(216) Wei, G.; Su, Z.; Reynolds, N. P.; Arosio, P.; Hamley, I. W.; Gazit, E.; Mezzenga, R. Self-Assembling Peptide and Protein Amyloids: From Structure to Tailored Function in Nanotechnology. *Chem. Soc. Rev.* **2017**, *46* (15), 4661–4708. https://doi.org/10.1039/c6cs00542j.

(217) Levin, A.; Hakala, T. A.; Schnaider, L.; Bernardes, G. J. L.; Gazit, E.; Knowles, T. P. J. Biomimetic Peptide Self-Assembly for Functional Materials. *Nat. Rev. Chem.* **2020**, *4* (11), 615–634. https://doi.org/10.1038/s41570-020-0215-y.

(218) Contreras-Montoya, R.; Arredondo-Amador, M.; Escolano-Casado, G.; Mañas-Torres, M. C.; González, M.; Conejero-Muriel, M.; Bhatia, V.; Diáz-Mochón, J. J.; Martínez-Augustin, O.; De Medina, F. S.; Lopez-Lopez, M. T.; Conejero-Lara, F.; Gavira, J. A.; De Cienfuegos, L. álvarez. Insulin Crystals Grown in Short-Peptide Supramolecular Hydrogels Show Enhanced Thermal Stability and Slower Release Profile. *ACS Appl. Mater. Interfaces* **2021**. https://doi.org/10.1021/acsami.1c00639.

(219) Chen, L.; Pont, G.; Morris, K.; Lotze, G.; Squires, A.; Serpell, L. C.; Adams, D. J. Salt-Induced Hydrogelation of Functionalised-Dipeptides at High PH. *Chem. Commun.* **2011**, *47* (44), 12071–12073. https://doi.org/10.1039/c1cc15474e.

(220) Chen, L.; McDonald, T. O.; Adams, D. J. Salt-Induced Hydrogels from Functionalised-Dipeptides. *RSC Adv.* **2013**, *3* (23), 8714–8720. https://doi.org/10.1039/c3ra40938d.

(221) Mañas-Torres, M. C.; Gila-Vilchez, C.; González-Vera, J. A.; Conejero-Lara, F.; Blanco, V.; Cuerva, J. M.; Lopez-Lopez, M. T.; Orte, A.; Álvarez De Cienfuegos, L. In Situ Real-Time Monitoring of the Mechanism of Self-Assembly of Short Peptide Supramolecular Polymers. *Mater. Chem. Front.* **2021**, *5* (14), 5452–5462. https://doi.org/10.1039/d1qm00477h.

(222) Liu, T.; Wang, X.; Wang, H.; Shi, G.; Gao, F.; Feng, H.; Deng, H.; Hu, L.; Lochner, E.; Schlottmann, P.; Von Molnár, S.; Li, Y.; Zhao, J.; Xiong, P. Linear and Nonlinear Two-Terminal Spin-Valve Effect from Chirality-Induced Spin Selectivity. *ACS Nano* **2020**, *14* (11), 15983–15991. https://doi.org/10.1021/acsnano.0c07438.

(223) Lee, S. M.; Kim, J. H.; Ahn, J. H. Graphene as a Flexible Electronic Material: Mechanical Limitations by Defect Formation and Efforts to Overcome. *Mater. Today* **2015**, *18* (6), 336–344. https://doi.org/10.1016/j.mattod.2015.01.017.

(224) Michaeli, K.; Varade, V.; Naaman, R.; Waldeck, D. H. A New Approach towards Spintronics-Spintronics with No

Magnets. *J. Phys. Condens. Matter* **2017**, *29* (10). https://doi.org/10.1088/1361-648X/aa54a4.

Appendix

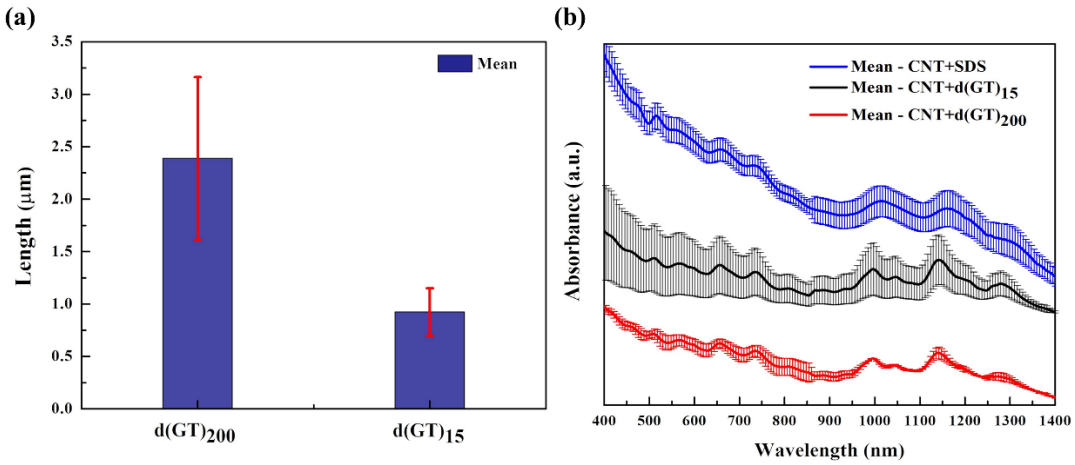

Figure AP 1. *(a) Average tube length and standard deviation computed over ~ 50 tubes. Sonication time is 90 minutes for both cases. Functionalization using $d(GT)_{200}$ results in a longer average length compared to $d(GT)_{15}$ (b) UV-Vis-near IR absorption spectra (multiple, ~3, scans), average scan and standard deviation at each data point.*

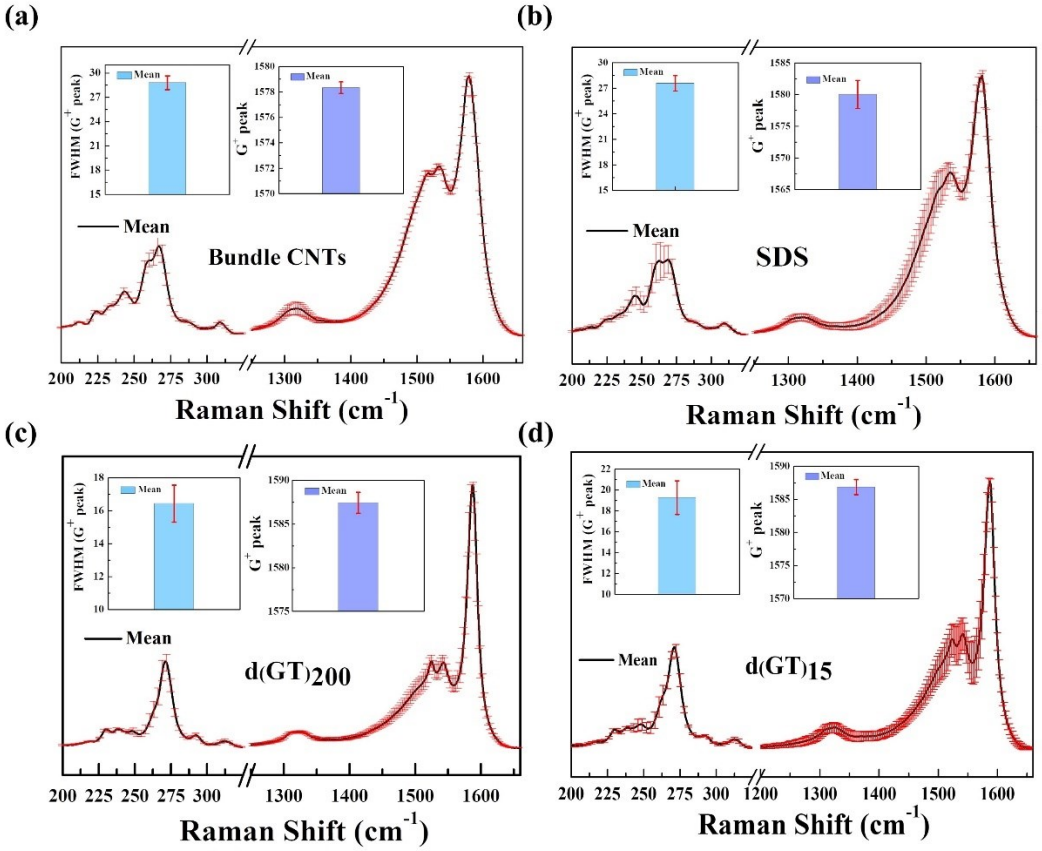

Figure AP 2. *Summary of multiple (~5) Raman scans. Average spectrum and standard deviation at each data point are shown. The general features described in chapter 2 are consistent with the statistical data.*

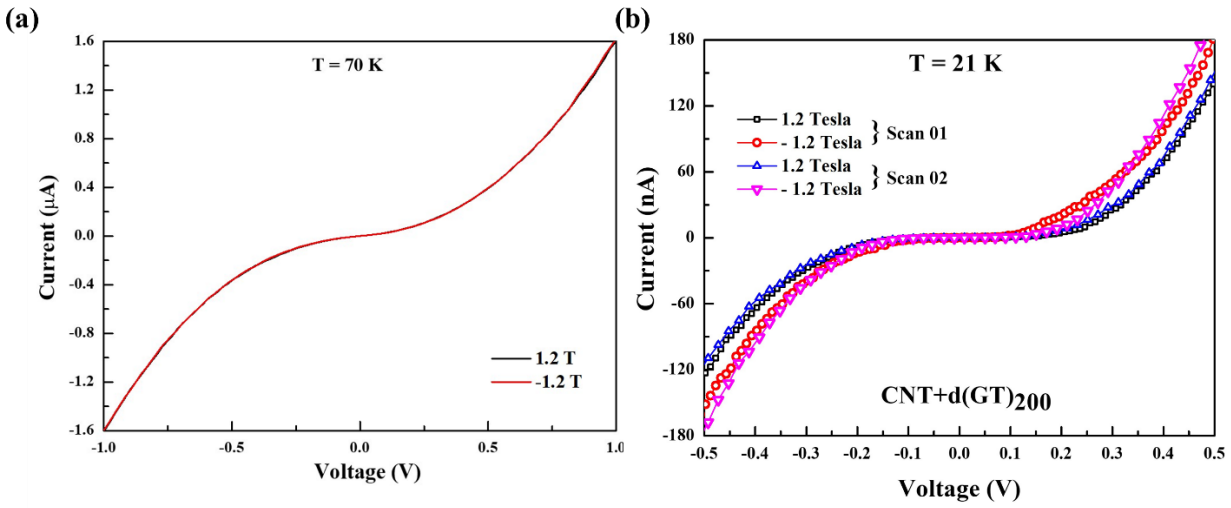

Figure AP 3. *(a) Negligible I-V splitting as a function of magnetic field at 70K for $d(GT)_{200}$ wrapped nanotubes. (b) Reproducibility of the I-V curves in presence of magnetic field.*

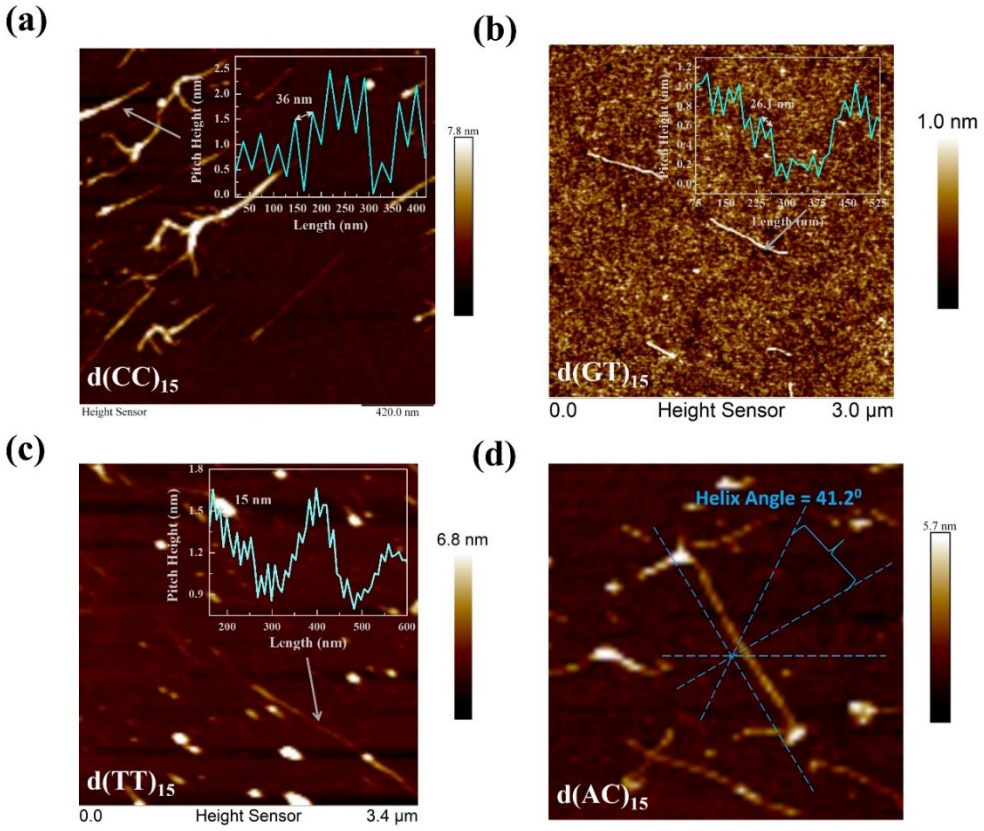

Figure AP 4. *Typical AFM images of (a) $d(CC)_{15}$, (b) $d(GT)_{15}$ and (c) $d(TT)_{15}$ wrapped nanotubes dispersed on SiO_2 substrate. Insets show line scan along nanotube lengths. Alternating bands of high and low regions are observed indicating helical wrapping. (d) Estimation of helix tilt angle from Fig. 3.2(a) in chapter 3.*

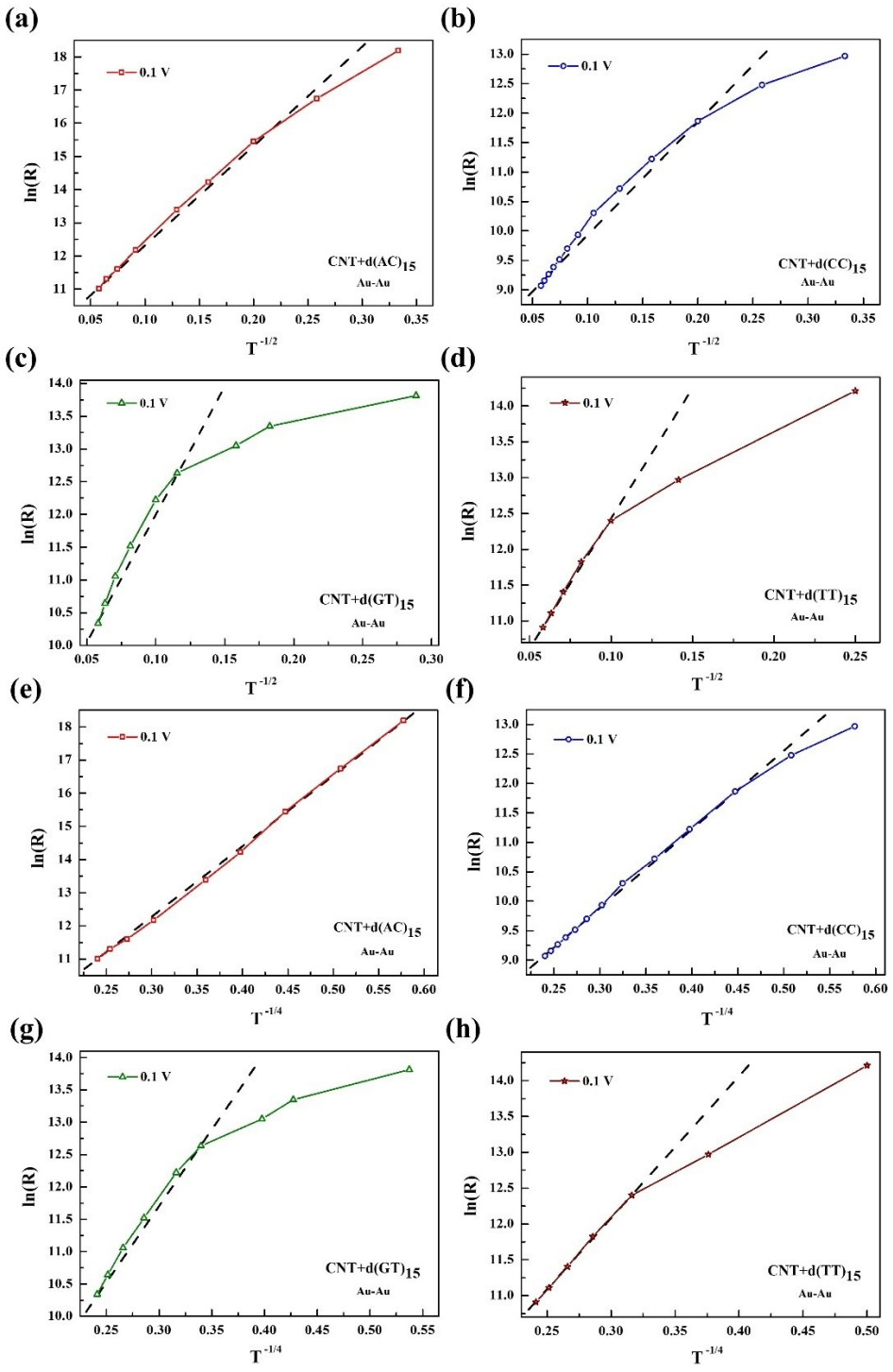

Figure AP 5. *ln R vs.* $(1/T)^{(1/(d+1))}$ *plots (VRH model) for (a)-(d) d = 1 and (e)-(h) d = 3. d(AC)$_{15}$ and d(CC)$_{15}$ functionalized samples show small deviations at low temperatures, whereas for d(GT)$_{15}$ and d(TT)$_{15}$ functionalizations, the deviation is significantly larger.*

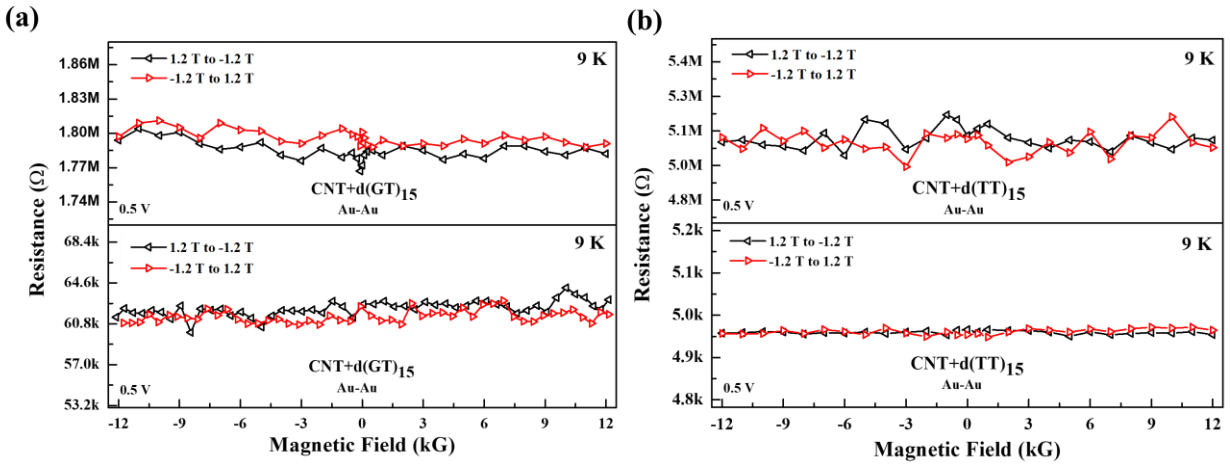

Figure AP 6. *Absence of any background negative MR in case of $d(GT)_{15}$ and $d(TT)_{15}$ functionalized CNTs ("strong coupling"). Data from multiple samples have been shown.*

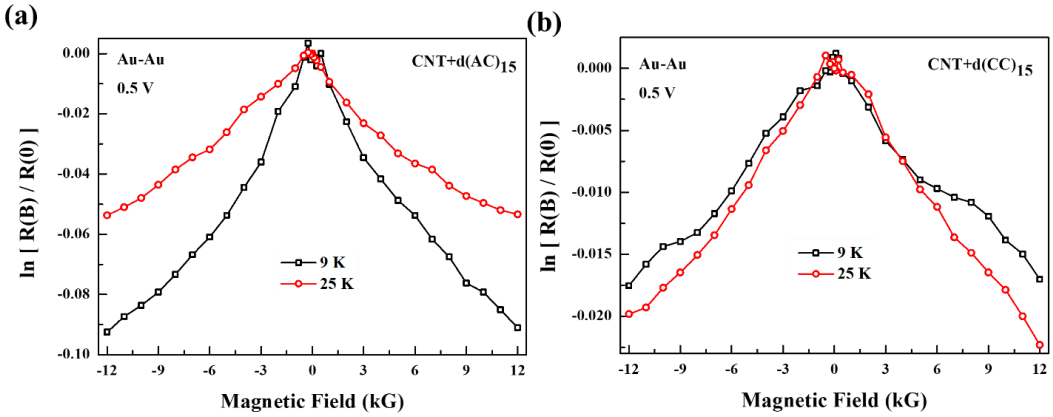

Figure AP 7. *Plot of ln (R (B)/R (0)) vs. B for $d(AC)_{15}$ and $d(CC)_{15}$ wrapped CNTs. Absence of a linear fit in the measured field range indicates that the "forward hopping" model described in chapter 3 is not the dominant transport mechanism.*

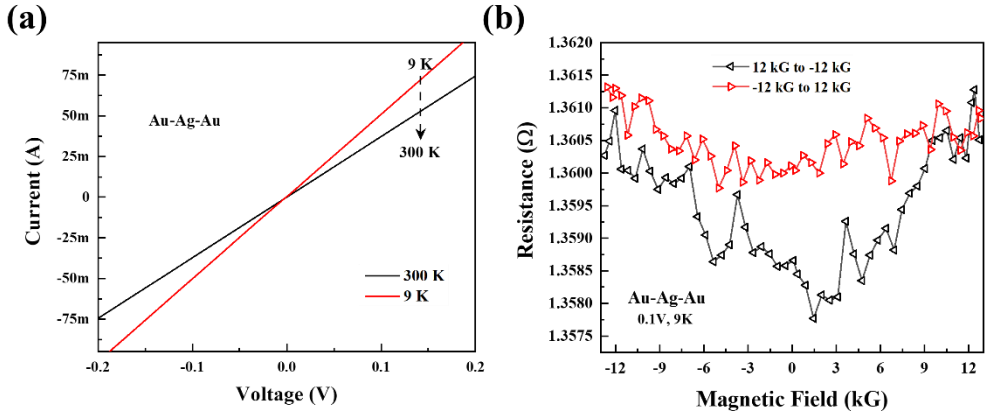

Figure AP 8. (a) *Current-voltage (I-V) characteristics of Au-Au contacts contacted with Ag paste at B = 0.* ***(b)*** *MR response of the Au-Ag-Au contacts (applied bias is 0.1 V).*

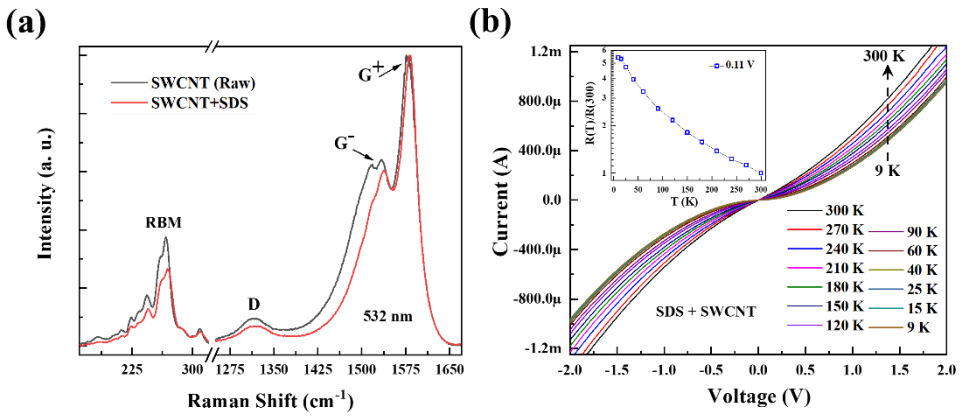

Figure AP 9. (a) *Current-voltage (I-V) characteristics of SDS+SWCNTs at B = 0 in Ni-Au electrodes in different temperatures, and* ***(b)*** *Raman characterization (532nm) of SWCNT+SDS.*

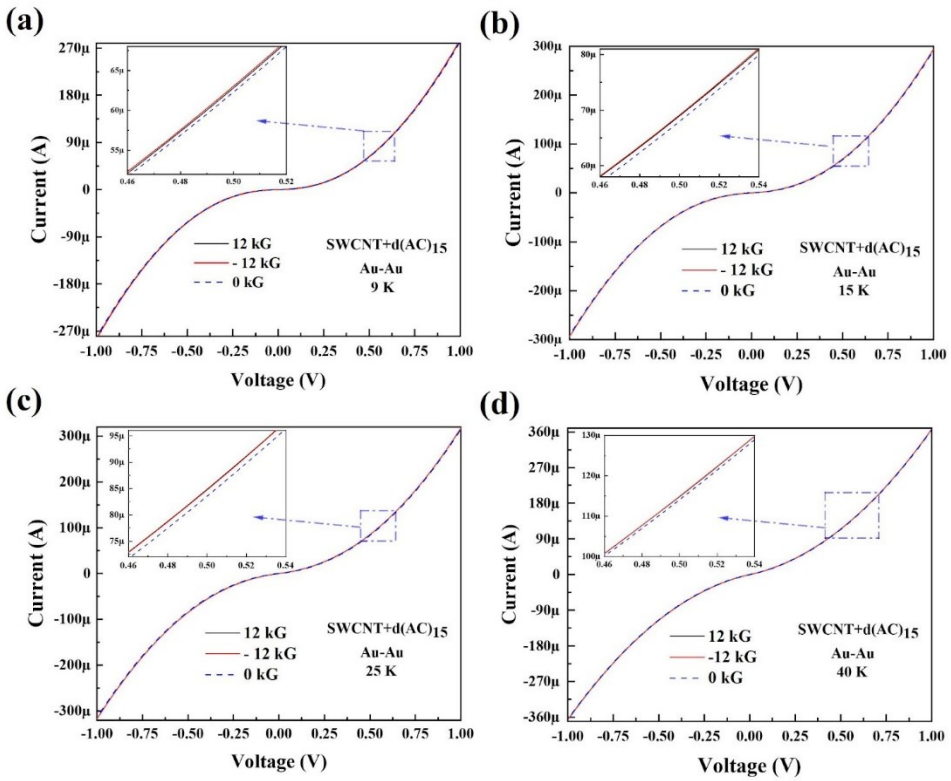

Figure AP 10. (a)-(d) *Current-voltage (*I-V*) characteristics of d(AC)$_{15}$+SWCNTs at* B *= 0 in Au-Au electrodes in different temperatures. Changes in MR% are clearly visible from the IV.*

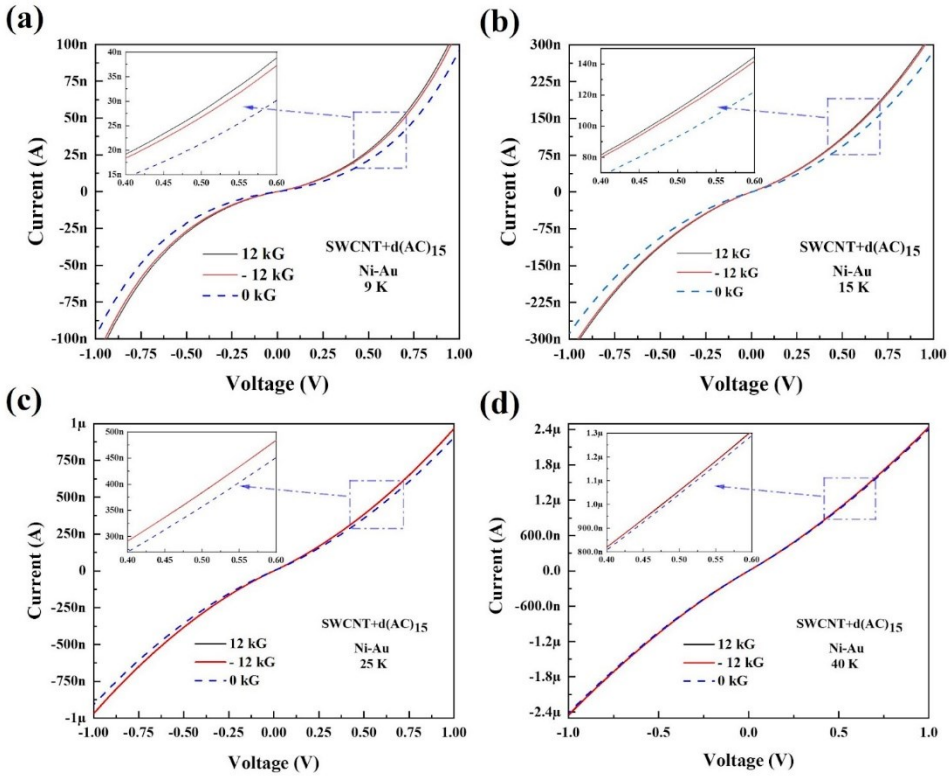

Figure AP 11. (a)-(d) *Current-voltage (*I-V*) characteristics of $d(AC)_{15}$+SWCNTs at* B *= 0 in Ni-Au electrodes in different temperatures. Changes in MR% and Δ% are clearly visible from the IV.*

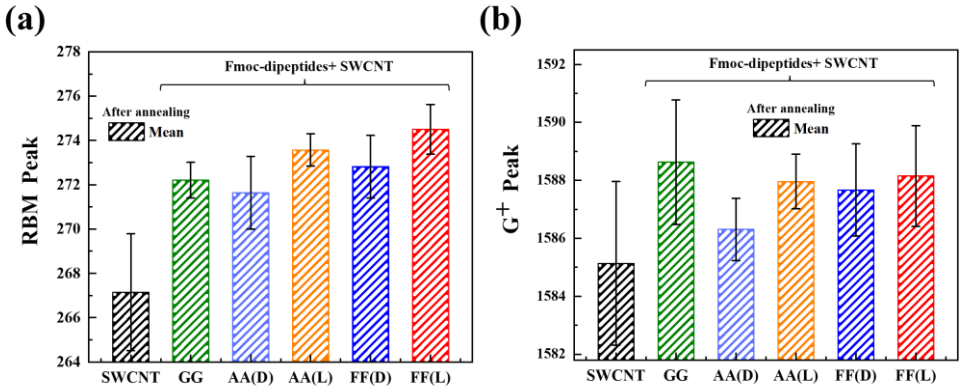

Figure AP 12. *RBM peak and G^+ peak positions as a function of molecular functionalization.*

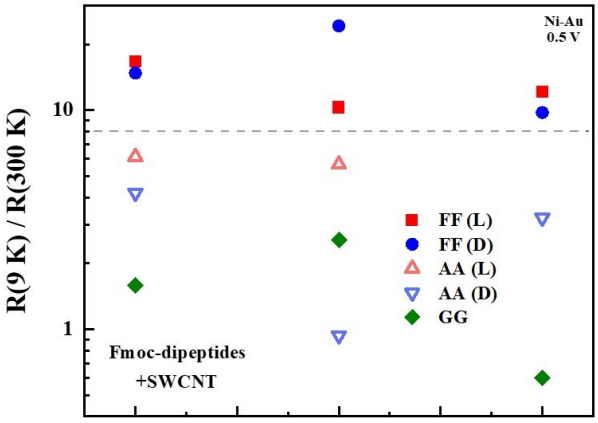

Figure AP 13. *Distribution of R(9K) / R(300K) values for different functionalizations.*

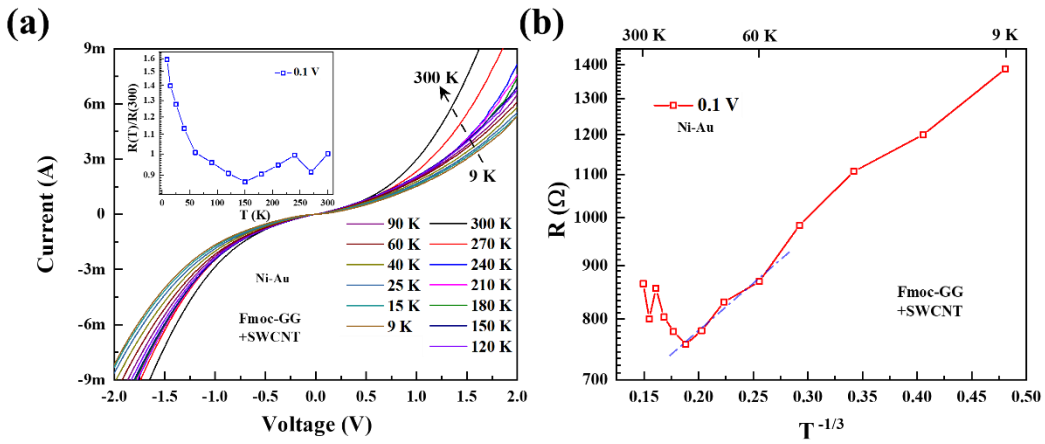

Figure AP 14. *Current-voltage (I-V) characteristics of* ***(a)*** *Fmoc-GG functionalized SWCNTs with Ni-Au contacts.* ***(b)*** *Fitting of device resistance R (= dV/dI) with the variable range hopping model for d = 2.*

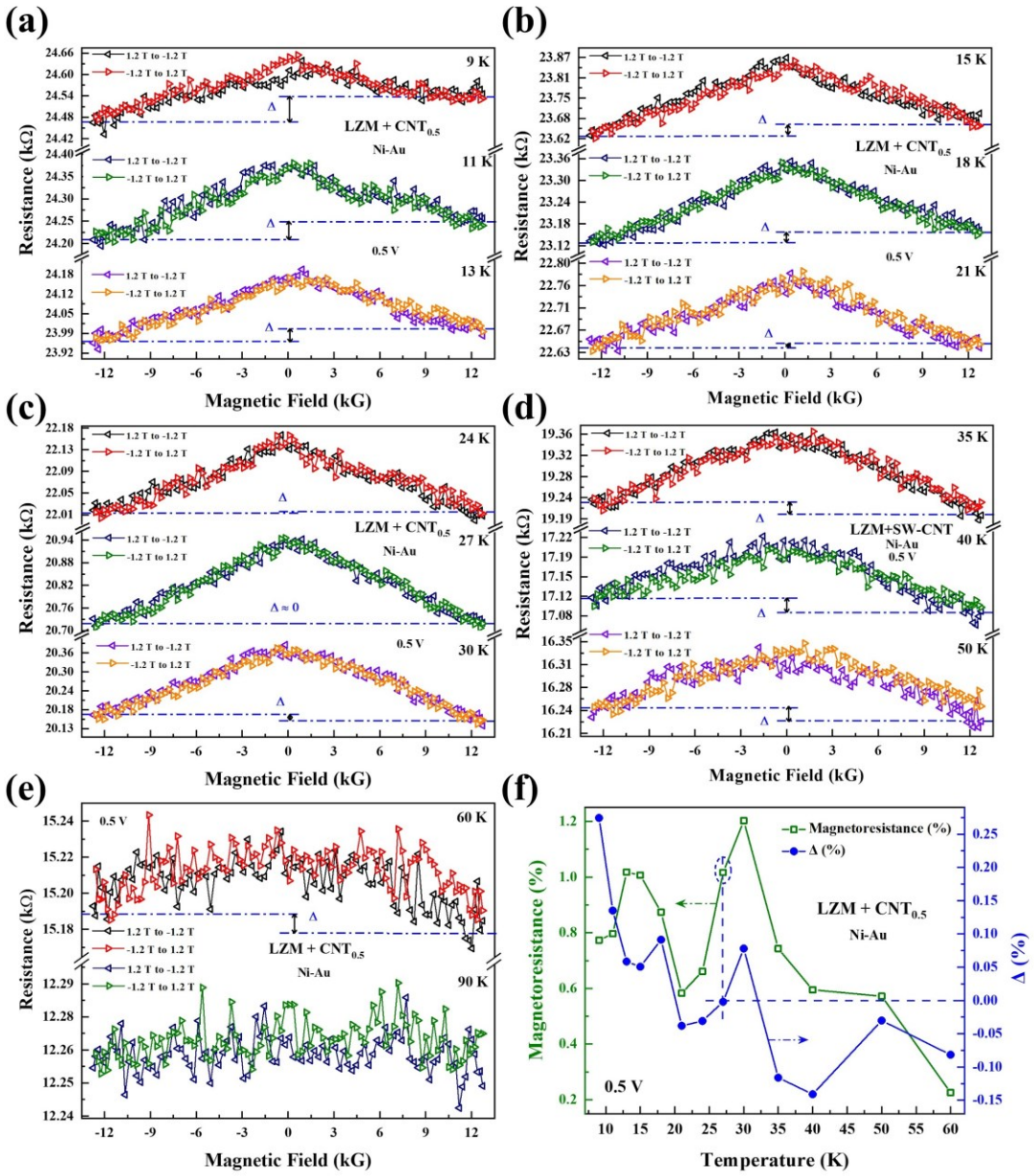

Figure AP 15. (a)-(e) *Asymmetric MR of LZM+CNTs (0.5 mg/ml) with Ni-Au contacts at different temperatures. Applied bias is 0.5V in all cases.* ***(f)*** *Temperature-dependence of background MR and Δ.*

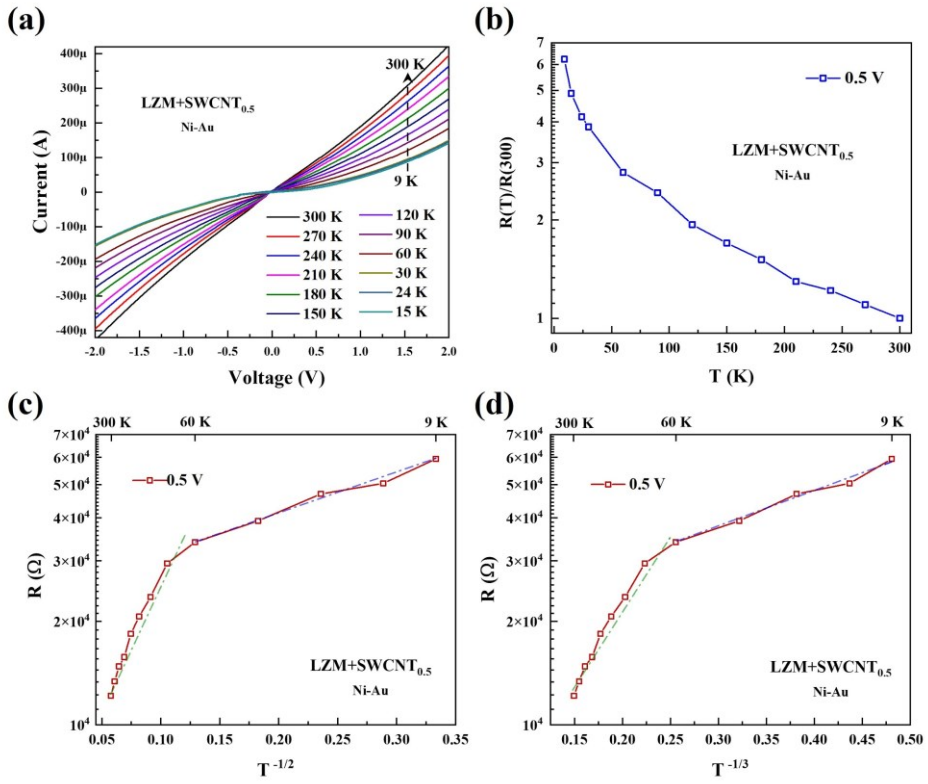

Figure AP 16. (a) *Current-voltage (I-V) characteristics of LZM+CNTs (0.5 mg/ml) at B = 0 using Ni-Au electrodes.* ***(b)*** *Temperature-dependence of the normalized resistance.* ***(c), (d)*** *Fitting with the VRH model for* d = *1 and 2.*

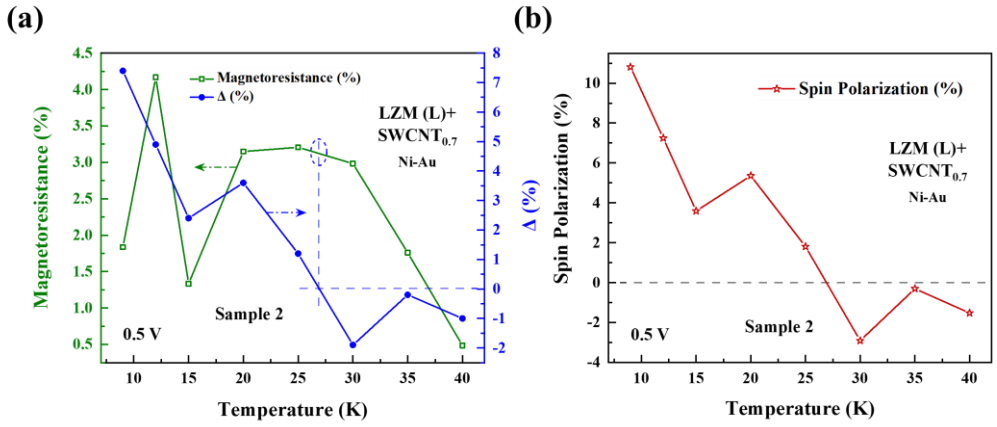

Figure AP 17. (a) *Temperature-dependence of background MR and Δ for a second LZM + CNTs (0.7 mg/ml) sample and* ***(b)*** *Spin polarization (estimated from Δ) vs. temperature.*

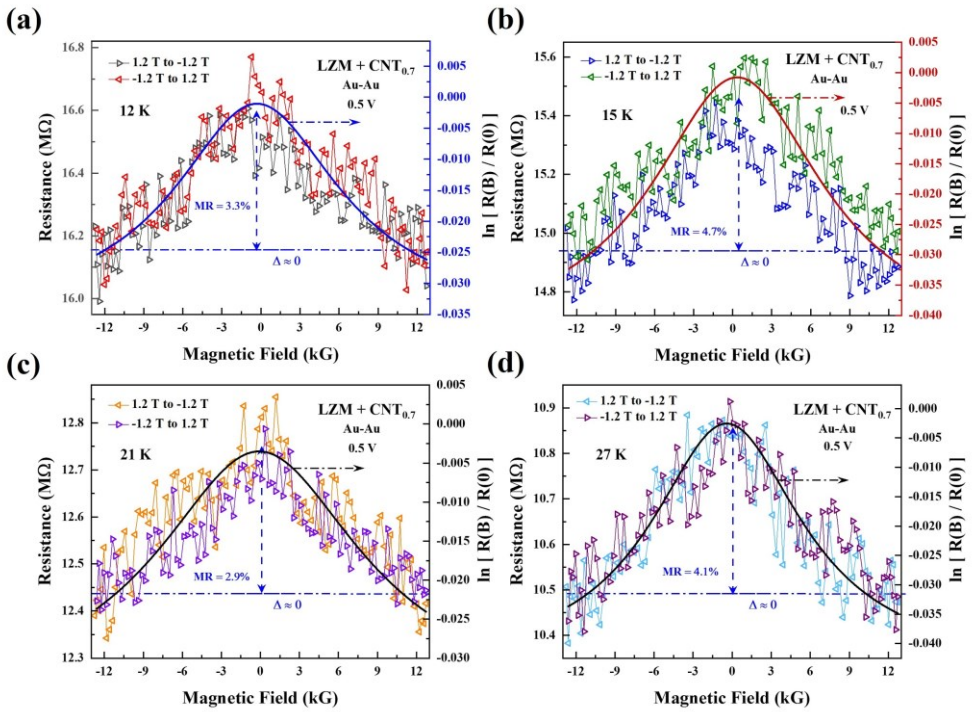

Figure AP 18. *Plot of ln [R (B)/R (0)] vs. B for LZM+CNTs (0.7 mg/ml) samples described in Figure 7.3 of the main paper. Absence of a linear fit in the measured field range indicates that quantum interference between forward hopping paths is not the dominant transport mechanism.*

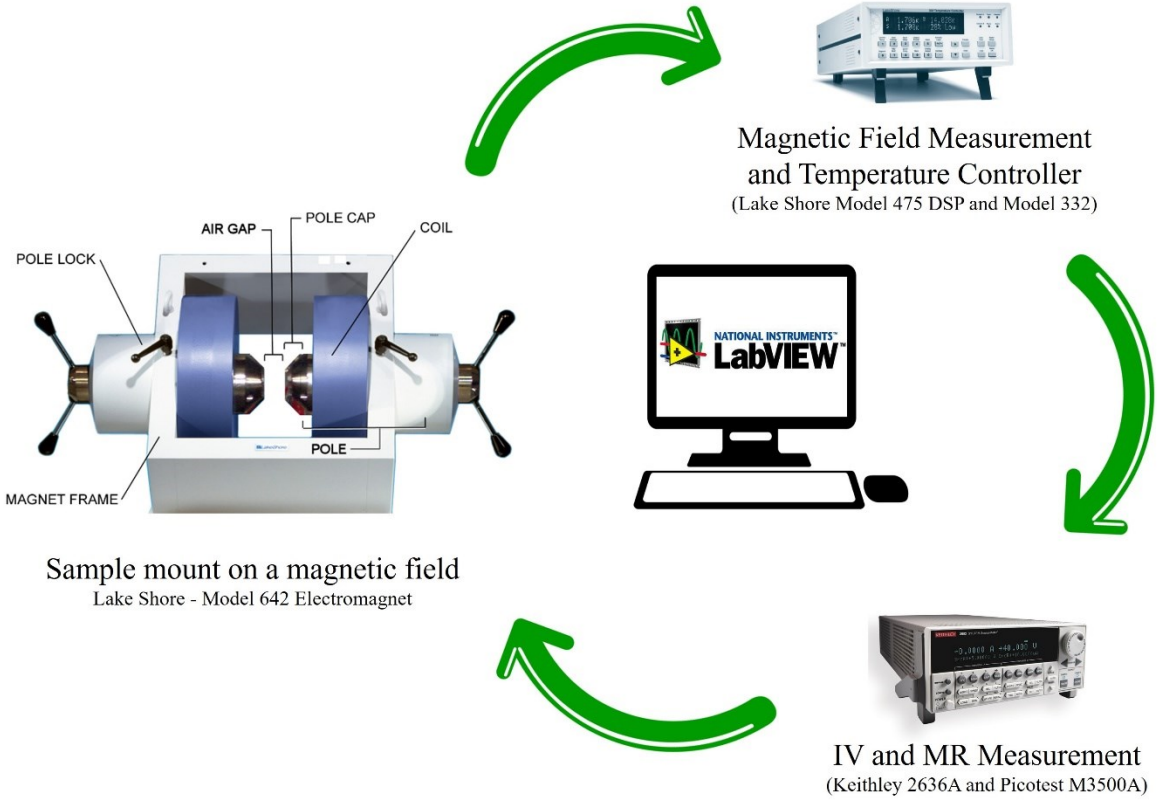

Figure AP 19. *Measurement setup schematics.*